CURRENT SHEET MASS LEAKAGE IN A PULSED PLASMA ACCELERATOR

John W. Berkery

A DISSERTATION
PRESENTED TO THE FACULTY
OF PRINCETON UNIVERSITY
IN CANDIDACY FOR THE DEGREE
OF DOCTOR OF PHILOSOPHY

RECOMMENDED FOR ACCEPTANCE
BY THE DEPARTMENT OF
MECHANICAL AND AEROSPACE ENGINEERING

November, 2005

Abstract

In a pulsed electromagnetic plasma accelerator a current sheet accelerates a propellant gas through the $\mathbf{j} \times \mathbf{B}$ force density. In the ideal case all of the gas is entrained and accelerated by the sheet. An observed departure from this ideality is current sheet mass leakage – a phenomenon through which a wake of plasma is left behind the sheet along the cathode. This leads to a decrease in sweeping efficiency – the percentage of the available propellant mass that is contained in the sheet. The goal of this work was to use experiments and an analytical model to understand the nature of the physical processes behind the mass leakage phenomenon and to quantify its effects on the performance of the accelerator over a range of pressures and propellants. Photography, interferometry, magnetic field probing, spectroscopy and momentum plate measurements are employed to gain an understanding of the evolution of the sheet and the performance of the device. It was found that after an initial bifurcation phase, the current sheet in this device enters a steady-state phase of propagation during which the mass, velocity and canting angle are approximately constant. Specific impulse and efficiency decrease with increasing propellant pressure for discharges using argon propellant, because of a decreasing sweeping efficiency. In neon, performance stays constant with pressure because the loss of mass from the current sheet is made up for by a commensurate increase in wake mass. In helium and hydrogen, performance increases with pressure, because while the sweeping efficiency stays constant, the wake velocity increases. The trends in the behavior of the sweeping efficiency have been explored with an analytical model. The model indicates that for the lighter propellants, which have a higher ion Hall parameter, the ions in the sheet are subject to a directed motion towards the cathode, causing a high degree of leakage of plasma into the wake. The heavier propellants, with low ion Hall parameters, are subject only to a diffusive leakage of ions at the cathode.

Acknowledgments

During my time here at Princeton, I have benefitted from the support and encouragement of many people. I would like to take this opportunity to thank them for their roles in helping me complete this dissertation.

To my wife Diana, I can't imagine doing it without you. Thank you for your patience, love and support. You have helped me more than you can imagine. We have been together now for almost ten years and I wouldn't change a day of it. I love you. Thank you for everything.

To my advisor, Professor Edgar Choueiri, thank you for your guidance and support. I learned a lot from you over the years, including how to write better papers, how to give better presentations, and how to better supplement my experimental work with theoretical modelling and analysis. You have really helped me develop into a more well rounded scientist, and I am grateful.

To Bob Sorenson, thank you for all the knowledge that you have imparted in me over the years. From you I learned a lot about electronics, high voltage and all things practical.

To Professor Bob Jahn, thank you for the academic knowledge that I gained from you. You were always willing to offer suggestions and point me in the right direction.

To Professor Sam Cohen, thank you for all your support and teaching. I am especially grateful for the guidance you provided me as I was searching for a postdoc position.

To the young guys in the lab, Luke Uribarri and Peter Norgaard, thank you for listening to my attempts to explain my research and giving me valuable feedback.

To the slightly younger guy, Jimmy Cooley, thanks for taking over my first project, and thank you for the many beneficial discussions we've had about both of our projects.

To my classmates, Kurt Polzin, Lenny Cassady and Slava Spektor, thank you for all the help with classes and when we were studying for generals, and many other discussions. We have all helped each other to become better scientists.

To the older guys, Andrea Kodys, Kamesh Sankaran, Vince Chiravelle and John Ziemer, thank you for your help getting acclimated to the lab during my early years here. You gave me a lot of guidance with classes, generals, and how to navigate in our department and lab.

Finally, to Tom Markusic, thank you for building this experiment and helping me get started with using it. I wouldn't have gotten very far without the benefit of your guidance and suggestions and your work has been an invaluable resource for me during my research.

This dissertation carries the designation 3144T in the records of the Department of Mechanical and Aerospace Engineering.

Nomenclature

a	Slope of the temperature line on a Boltzmann plot
A_{nm}	Emission transition probability for the atomic transition from level m to n
b	y-intercept of temperature line
B	Magnetic field strength
$\bar{c}$	Thermal velocity
c	The speed of light in vacuum
C	Capacitance
d	Depth of current sheet (width of electrodes, z dimension)
D	Drag
e	Electric charge
E	Electric field
E_0	Input energy
E_{in}	Incident energy on the momentum plate
E_m	Energy of atomic level m
E_{ref}	Energy reflected from the momentum plate
F	Force
F_{ref}	Fraction of momentum that is reflected from the momentum plate
g_0	Acceleration due to gravity
g_m	Degeneracy of atomic level m
h	Gap height between electrodes (y dimension)
$\hbar$	Planck's constant
i_{nm}	Spectrally integrated intensity of light from the atomic transition from level m to n
I_{nm}	Spectral emission line intensity profile
I_{sh}	Impulse of the sheet
I_{sp}	Specific impulse
I_{total}	Total impulse, or momentum, delivered by the sheet and wake
j	Current density
J	Total current
k	Boltzmann's constant
K_{sh}	Kinetic energy of the sheet
K_w	Kinetic energy of the wake
l	Length of the electrodes
L	Inductance
L'	Inductance per unit length

Nomenclature (cont.)

m_a	Mass of an ambient neutral particle
m_{av}	Total propellant mass available to the discharge
m_e	Mass of an electron
m_i	Mass of an ion
m_{sh}	Mass of the sheet
m_w	Mass of the wake
n_a	Ambient neutral number density
n_c	Cutoff density, above which the interferometer laser beam is reflected out of the plasma
n_e	Electron number density
n_i	Ion number density
N_m	Population of atomic level m
p	Pressure
Q_{ia}^{cx}	Ion-ambient neutral charge exchange collision cross section
Q_{ia}^{es}	Ion-ambient neutral elastic scattering collision cross section
R_E	Energy reflection coefficient
R_N	Particle reflection coefficient
T_e	Electron temperature
u_e	Electron species velocity
u_i	Ion species velocity
U_e	Electron drift velocity
U_i	Ion drift velocity
v	Fluid velocity
v_c	Velocity of ions towards the cathode
v_H	Theoretical velocity of hydrogen current sheets
v_{sh}	Velocity of the sheet
v_x	Theoretical velocity of the sheet in the x direction
v_w	Velocity of the wake
v^*	Characteristic velocity (all input energy goes into kinetic energy)
V	Voltage
w	Width of the current sheet (x dimension)
X	Percent of ambient neutrals that is accelerated to the sheet velocity
y	Normalized radiative intensity
Z_a	Electronic partition function of species a

Nomenclature (cont.)

Γ^e	Flux of mass entering the current sheet
Γ^l	Flux of mass leaking from the sheet at the cathode
δ	Width of the current sheet in the direction perpendicular to the current
ϵ_0	Permittivity of free space
η	Efficiency
θ	Canting angle
λ_{mn}	Wavelength of atomic transition from level m to n
μ_0	Magnetic permeability of free space
ν_{xy}	Momentum transfer collision frequency between particles x and y
ξ_{sh}	Non-dimensional current sheet velocity
ξ_w	Non-dimensional wake velocity
ρ_a	Density of the ambient fill gas
ρ_c	Density of the plasma at the cathode in the current sheet
ρ_i	Density of ions in the sheet
ϕ	Phase angle
Φ_{sh}	Non-dimensional current sheet mass (sweeping efficiency)
Φ_w	Non-dimensional wake mass
ω	The frequency of a HeNe laser
ω_c	Cyclotron frequency
ω_{mn}	Frequency of atomic transition from level m to n
ω_p	Plasma frequency
Ω_i	Ion Hall parameter

Contents

Chapter 1

Introduction

1.1 Electric Propulsion Overview

Electric propulsion is a class of thrusters for spacecraft that derive thrust from the acceleration of charged particles [1, 2, 3, 4]. The thrust or (in the case of pulsed thrusters) impulse can be obtained in three general ways: electrothermally, electrostatically, and electromagnetically. Electrothermal thrusters heat a gas using electricity (as opposed to a chemical reaction) and expel the gas, typically through a nozzle. Electrostatic thrusters, typically called ion thrusters, use an electric field across two plates to accelerate ions. Electromagnetic thrusters typically use the interaction of current and magnetic fields to accelerate plasma. Electromagnetic thrusters may be steady state devices, such as magnetoplasmadynamic thrusters, or they may operate in a pulsed manner. The research reported in this dissertation was performed in a pulsed electromagnetic accelerator.
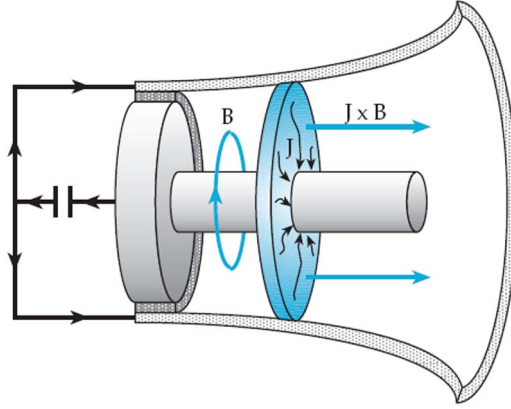
Figure 1.1: Diagram of a gas-fed pulsed plasma thruster, from reference [7].

1.1.1 Gas-Fed Pulsed Plasma Thrusters

Pulsed plasma thrusters (PPTs) are one category of electric propulsion. PPTs are divided neatly into two categories: ablative PPTs and gas-fed PPTs.

Ablative PPTs are by far the more common variety and have undergone far more research and development [5]. These thrusters use a solid, usually Teflon, as their propellant. A discharge ablates the solid propellant and accelerates it as a plasma, using the Lorentz force. The impulse of these thrusters is often primarily electrothermal, however [6]. Due to the ablation process, the existence of macro particles and the thermally derived component of the impulse, the physics of these devices is quite different from that of gas-fed PPTs. We will concentrate on the gas-fed variety, the type of thruster used in the present research.

In gas-fed pulsed plasma thrusters a propellant gas is fed into an electrode gap and broken down into a plasma. This plasma forms a current sheet, carrying current from the anode to the cathode. The current creates a magnetic field and the interaction of the current and magnetic field creates a force. This $\mathbf{j} \times \mathbf{B}$ (or Lorentz) force density accelerates the current sheet along the electrodes and expels the plasma with a certain velocity. A typical coaxial gas-fed PPT configuration is shown in figure 1.1, from reference [7].

2

Gas-fed PPTs are viable options for space propulsion for attitude control and orbital transfer for satellites, or possibly deep space propulsion when the available power is limited [7]. Research on gas-fed PPTs was conducted in the 1960's and 1970's and revived in the 1990's at Princeton University [8]. Ziemer performed a study of gas-fed PPT performance scaling [7]. Several open topics of research were identified by Ziemer including the extension of performance scaling models to higher energies, alternative discharge initiation mechanisms [9], current sheet canting [10], and current sheet leakage. It is the last of these issues that is studied in the present work.

1.2 Current Sheet Mass Leakage - Motivation For This Study

The desired behavior of the current sheet in a gas-fed pulsed plasma thruster with a uniform gas fill is that it follows the "snowplow model" of development. The snowplow model describes a progression of the sheet from an initiation phase to a sweeping phase and finally expulsion [1].

In the initiation phase, the current sheet forms as a thin, planar sheet, perpendicular to the electrodes, at the breech of the device. The breech is the lowest inductance point of the circuit, so the arc tends to form there initially.

In the sweeping phase, the current sheet moves into the neutral gas, ionizing the particles it encounters and incorporating them into the sheet. The sheet maintains its planarity and remains perpendicular to the electrodes while growing steadily heavier. A schematic of the current sheet in a parallel-plate accelerator is shown in figure 1.2.

In the expulsion phase, the sheet reaches the end of the electrodes and ideally the current is cut off at the same time. The mass accelerated by the sheet is ejected, giving an impulse.
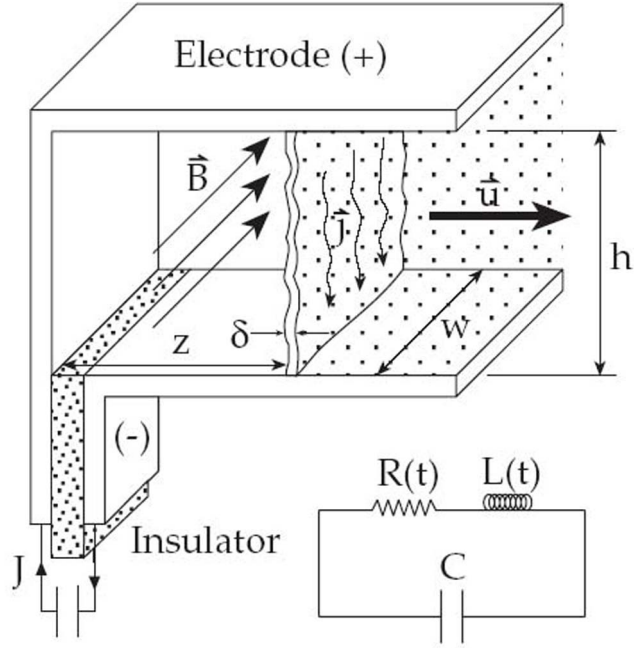
Figure 1.2: Diagram of an ideal current sheet in the sweeping phase, from reference [7] This diagram shows the parallel-plate configuration, which was used in this study and is to be distinguished from the coaxial geometry shown in figure 1.1.

Previous research has shown that the operation of these devices is not likely to follow the ideal pattern of the snowplow model. Recently, a study by Markusic [10] at Princeton University's Electric Propulsion and Plasma Dynamics Laboratory showed that the behavior of current sheets was more complicated.

Markusic's study focused on the tendency of the current sheet to cant, or tilt, with the anode attachment leading the cathode attachment. This behavior was evident under all conditions tested, and is shown in figure 1.3. Markusic's canting study is discussed further in the next chapter.

Also evident from Markusic's study was that the current sheet seemed to be leaking plasma along the cathode as it travelled. This is also visible in figure 1.3. The present study
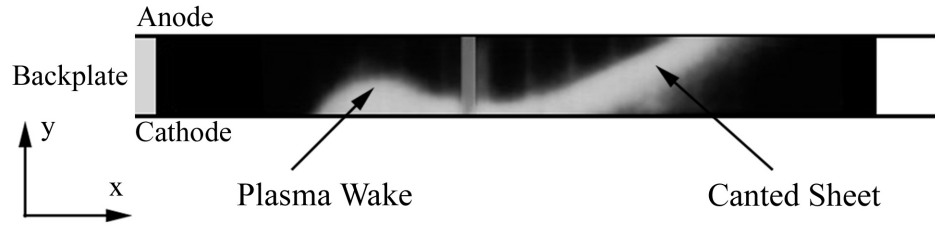
Figure 1.3: Photograph of a discharge from [10], showing two non-idealities of current sheet behavior. The top electrode is the anode and the bottom electrode is the cathode. The plasma is moving from left to right. The ideal behavior would be for the current sheet to be perpendicular to the electrodes. Instead we see a canted sheet and a plasma wake trailing the sheet along the cathode. The vertical bar in the middle of the photograph is a physical structure that obscured the light, not a plasma structure.

focuses on this phenomenon of current sheet leakage.

It is clear that leakage of the propellant through the current sheet could lead to a loss of momentum of that portion of the propellant. This can have a negative effect on the performance of the device. Although researchers have seen current sheet leakage in the past, a study of its effect on the performance of the accelerator has never been published. Also, knowledge of the fundamental physics behind the leakage phenomenon and the partitioning of momentum into the sheet and wake was lacking. It is these questions which the current study aims to answer.

1.3 The Effect of Mass Leakage on Accelerator Performance

York and Jahn introduced a "sweeping parameter" for a current sheet which is the percent of available mass contained in the sheet [11]. This parameter is defined,

$$\Phi_{sh} = \frac{m_{sh}}{m_{av}}, \tag{1.1}$$

where m_{sh} is the mass of the sheet, and m_{av} is the total available mass. In the experiments presented in this dissertation, the accelerator is operated with a uniform gas fill, so the available mass is simply the density of the gas fill times the volume of the accelerator.

The sweeping parameter is interesting to know in its own right, but further motivation for this study can be drawn from quantifying its effect on the thruster performance. There are three important performance measurements of a pulsed plasma accelerator: total impulse, specific impulse, and efficiency.

Total impulse, the analog of thrust in a steady-state device, is the momentum delivered by a single pulse of the device. This includes the momentum of the current sheet, and the plasma wake. We will make the assumption that the available mass is contained in either the sheet or the wake, or it is lost entirely. The third possibility would happen, for example, if neutral particles were to permeate through the sheet without gaining momentum. If we also make the assumption that the sheet and wake velocities can be represented with mass-averaged velocities, then the total impulse can be written, in terms of the sweeping parameter, as:

$$I_{total} = m_{sh}v_{sh} + m_w v_w = m_{av}(\Phi_{sh}v_{sh} + \Phi_w v_w). \tag{1.2}$$

The sheet mass and velocity are represented by m_{sh} and v_{sh} and the wake mass and velocity

are indicated by m_w and v_w. We have also introduced a parameter, Φ_w, for the wake that is analogous to the sweeping efficiency of the sheet (equation 1.1).

Since plasma in the wake is leaking out of the acceleration region, we expect to have a wake velocity that is a fraction of the sheet velocity. Therefore a higher sweeping parameter (a larger percentage of the available mass is contained in the sheet) should lead to a higher total impulse.

We can further non-dimensionalize the total impulse equation by defining a characteristic velocity. Since the characteristic mass used was the available mass, m_{av}, a logical characteristic velocity to use is,

$$v^* = \sqrt{\frac{2E_0}{m_{av}}}, \tag{1.3}$$

where E_0 is the initial energy stored in the pulse forming network. This is what the velocity would be if all the energy put into the discharge was converted into kinetic energy, and all of the available mass was accelerated. Of course, the velocities achieved in our experiments are merely fractions of this velocity (10% - 25%).

Now, we can write the non-dimensional total impulse as,

$$\hat{I}_{total} = \Phi_{sh}\xi_{sh} + \Phi_w\xi_w, \tag{1.4}$$

where $\xi_{sh} = v_{sh}/v^*$ and $\xi_w = v_w/v^*$.

Also, we can write the specific impulse and acceleration efficiency based on the same non-dimensional parameters. Specific impulse is the ratio of the thrust derived to the rate of propellant use, and it is important as a measure of the "fuel efficiency" of the thruster. A higher specific impulse means that the same momentum can be gained while using less propellant. The acceleration efficiency of a thruster is an "energy efficiency" in that a higher acceleration efficiency means that the same momentum can be gained while using

less input energy.

The specific impulse of a pulsed thruster can be written as the total impulse divided by the propellant weight at sea-level,

$$I_{sp} = \frac{I_{total}}{m_{av}g_0}, \tag{1.5}$$

$$\hat{I}_{sp} = \frac{I_{sp}}{v^*/g_0} = \Phi_{sh}\xi_{sh} + \Phi_w\xi_w. \tag{1.6}$$

The non-dimensional specific impulse is the same as the non-dimensional total impulse. This is not surprising since we have non-dimensionalized the total impulse with the available mass, which gives it the same meaning as the non-dimensional specific impulse.

Next we consider the acceleration efficiency of the device. The acceleration efficiency is the percentage of input energy that is converted into kinetic energy. Efficiency is already non-dimensional:

$$\eta = \frac{K_{sh} + K_w}{E_0} = \Phi_{sh}\xi_{sh}^2 + \Phi_w\xi_w^2. \tag{1.7}$$

Again we see that, since $\xi_{sh} > \xi_w$, the efficiency increases with increasing sweeping parameter.

It is clear that for a given operating condition four parameters must be measured to characterize the performance of the device: the mass and velocity of the sheet and the mass and velocity of the wake. The goal of this dissertation is to explore how the accelerator performs under different operating conditions and how the mass leakage process effects the performance. We will thus characterize the dependencies of the four non-dimensional parameters, Φ_{sh}, Φ_w, ξ_{sh}, and ξ_w on experimental conditions. In addition to knowing *what* the effect of mass leakage on performance is, through the four parameters listed above, we will explore *why* the leakage occurs, and how it depends on the propellant species and pressure.

1.4   Dissertation Outline

The bulk of this dissertation explains the experimental methodology for determining the effect of current sheet mass leakage on accelerator performance, and the results and conclusions of those experiments. Chapter 2 is a review of previous research, focusing on findings relevant to the problem of current sheet mass leakage. In Chapter 3 the experimental setup and the various experimental diagnostics used, including a high-speed camera, magnetic field probes, a laser interferometer, a spectrometer and a momentum plate, are described in detail. In Chapter 4 the results of a detailed case study are laid out. This study consisted of detailed mapping of the magnetic field, current density and electron number density with spatial and temporal resolution under the particular operating condition of argon propellant at 100 mTorr pressure. The purpose of such a study was to describe the evolution of the sheet and wake structures in detail. In Chapter 5 the results of a set of performance measurements is presented. These included measurements of total impulse, current sheet mass and velocity, and wake velocity of discharges with argon, neon, helium and hydrogen propellants with fill pressures ranging from 75 mTorr to 400 mTorr. The purpose of these measurements is to characterize the extent of the mass leakage phenomenon and how it affects the performance of the device. In Chapter 6 a model of the current sheet is presented that explains the observed behavior in the current sheet sweeping phase. Finally, Chapter 7 provides the conclusions of this work.

Chapter 2

Review of Previous Research

In this chapter we present a review of previous research that is relevant to the study of current sheet mass leakage in pulsed plasma accelerators.

2.1   Overview of Previous Research

The problem of current sheet leakage has been identified by a few researchers in the past, although no one has published a systematic study of the phenomenon. Much of this work was performed in the 1960s, and some of it was not directly related to propulsion applications. Nonetheless many of the reported findings are relevant to this study because similar processes and structures were seen. In this section, an overview of the most relevant previous studies is presented, in chronological order.

Burkhardt and Lovberg used circumstantial evidence to argue the existence of current sheet "permeability" in a coaxial plasma accelerator in 1962 [12]. They noted the increased speed of the sheet compared to the expected speed, which implied a reduced propellant drag due to propellant permeating through the sheet. Permeability, however, refers to a certain

leakiness or porosity of the sheet to neutrals, and not a systematic leakage of plasma along the cathode that is the focus of our studies.

They also noticed the coaxial sheet was planar, while the expected behavior would be a lag at large radius due to the radial drop off of the magnetic field. The planarity of their sheet, and other coaxial configurations with the cathode at the center, might be explained by the counter-acting influences of the drop in magnetic field away from the cathode and the known tendency for the anode attachment to lead the that of the cathode.

Keck studied the current sheet in a magnetic annular shock tube, also in 1962 [13]. Using magnetic field probes, in a grid of measurement points, he mapped the current density in the device. With the polarity such that the outer electrode was the cathode, he observed a canted current sheet, with the anode attachment leading the cathode attachment (see figure 2.1). Also from the same data, Keck states that "the current distribution suggests the growth of a gas "bubble" on the outside wall [cathode] behind the current sheet". This is because the decreased magnetic field in the cathode region behind the sheet implied an increase of gas pressure in that region.

An explanation for this observation is offered in a companion paper by Fishman and Petschek [14]. They propose a model, shown in figure 2.2, of the flow in the device:

> The current sheet may be regarded as a solid body moving through the gas. A shock wave will form slightly ahead of the current sheet. When this flow reaches the outside wall [cathode], its radial motion is stopped and therefore its pressure increased, moving the current sheet further away from the wall and allowing the gas to flow through and form a bubble.

This is the first suggestion we find for what is causing the wake of plasma. It is also interesting to note the connection between the canting of the sheet and the flow of ions towards the cathode and eventually into the wake.
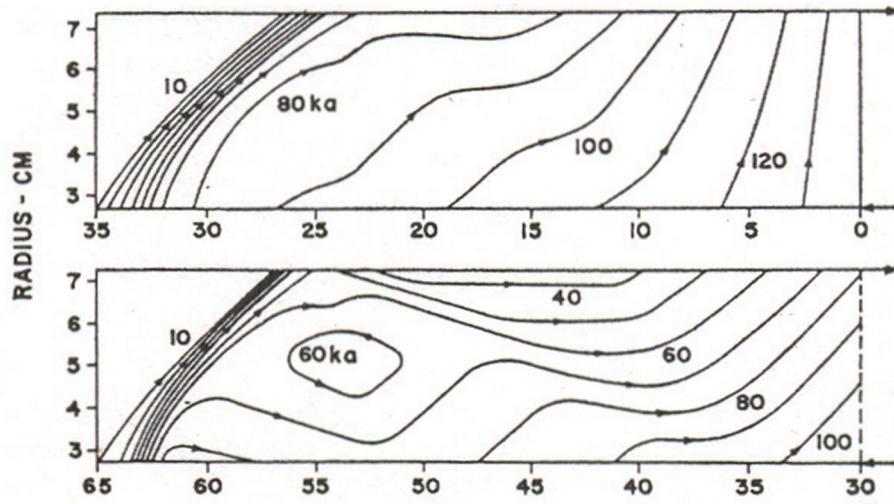
Figure 2.1: Current contours from two different times in a magnetic annular shock tube, from reference [13]. The cathode is on top, the anode on bottom, and the discharge is moving from right to left in this case. The conditions are: 50 mTorr of argon, 5 kV discharge.

Lovberg, in 1963, measured the electric fields inside of current sheets in a parallel-plate accelerator [15]. He found that in hydrogen discharges, ions carried much of the current in the sheet and there was no polarization field due to ion-electron separation. In nitrogen discharges, ions did not carry current and they were accelerated by the polarization electric field. Thus there must have been, in this case, a flow of ions to the cathode in hydrogen discharges, but not in nitrogen discharges.

Later, Lovberg also noticed plasma lagging along the cathode after the current sheet had passed [16] in his device. Using Schlieren photography, Lovberg investigated the plasma density in his parallel-plate accelerator. The development of current sheet structures is shown in figure 2.3; the discharge was operated with nitrogen at 120 mTorr. These photographs show a bifurcation of the sheet near the anode (left of figure 2.3) and subsequent canting of the sheet (right of figure 2.3), with two plasma structures evident. Lovberg reports in the caption of the photo: "The rapid current sheet advance near the anode results
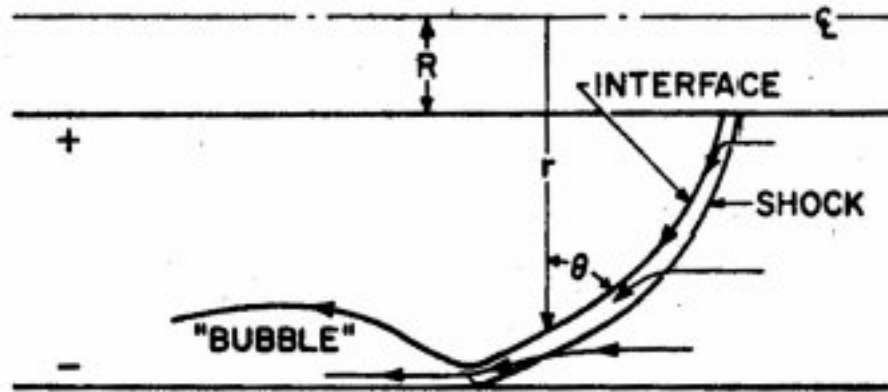
Figure 2.2: Drawing from Fishman and Petschek [14], explaining their model of the formation of a gas "bubble" along the cathode.

in giving the plasma a velocity component toward the cathode".

In hydrogen at 300 mTorr, the sheet appears to remain more planar, but a layer of plasma is visible along the cathode (figure 2.4). This plasma layer is seen as the bright line along the bottom electrode in the figure, stretching from the sheet back to the breech of the accelerator. Lovberg attributes the existence of the layer to a flow of ions towards the cathode in order to carry a significant portion of the current. He goes on to say:

> What is then to be expected is that the current sheet should leave in its wake a very dense layer of gas highly compressed against the cathode, since the ions which moved into this electrode at a velocity necessarily close to the sheet speed will in general lose most of their kinetic energy and be able to move away again (as neutrals or re-formed ions) at speeds not much greater than room temperature thermal velocities. On our time scale, this means very little motion away from the cathode.

Lovberg is concerned with the fact that the plasma layer is so dense, and doesn't appear
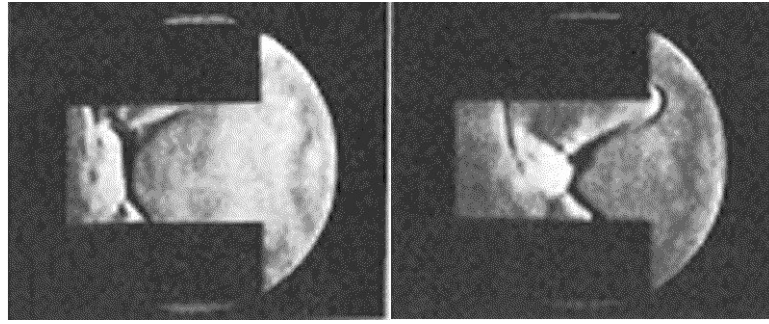
13

Figure 2.3: Schlieren image from Lovberg [16]. The anode is on top and the cathode is on bottom. The sheet is the vertical column of fringes which indicate a vertical density gradient in the sheet. The conditions are: nitrogen propellant, 120 mTorr.

to recombine significantly. It is clear that this cathode plasma layer is an ionized plasma and not neutrals, because the Schlieren photography method can distinguish neutrals from free electrons by the direction of the deflection of the light [16]. Lovberg attributes the ionization of the plasma layer to current being carried in the layer:

> It seems surprising that such an apparently dense plasma is able to maintain its ionization under these conditions... A likely explanation of what is observed here... is that the return current from the discharge is actually being carried along the cathode surface, in some fraction at least, by this boundary layer, and that this current, while not heating the plasma ions enough to cause rapid expansion of the gas away from the cathode, is able to maintain ionization at the level observed here.

Altogether, Lovberg's Schlieren studies provided the best experimental evidence until recently of current sheet leakage through a cathode plasma wake.

In 1965 Johansson performed a study focusing on current sheet tilt in a radial shock tube [17]. Although Johansson did not specifically mention a plasma wake, he does consider the implications of a canted current sheet. "The direction of this tilt is such as to deflect the ions
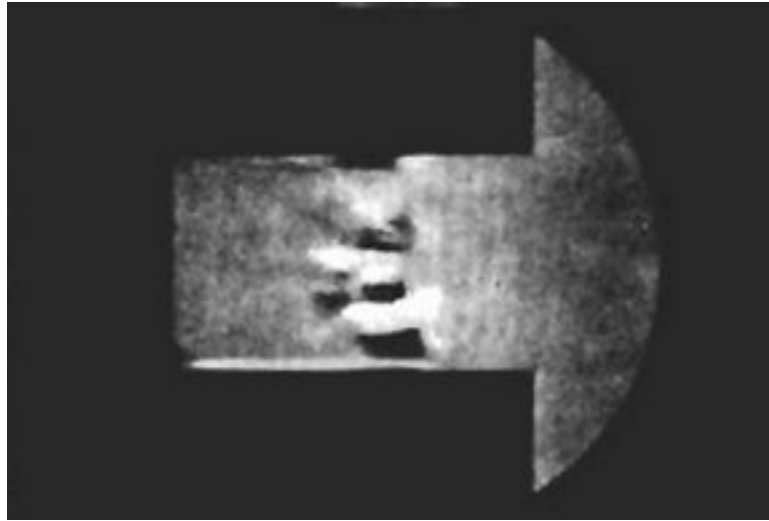
Figure 2.4: Schlieren image from Lovberg [16]. The anode is on top and the cathode is on bottom. The conditions are: hydrogen propellant, 300 mTorr.

so that they can carry current." This is a similar analysis to that of Fishman and Petschek, with the added observation that is similar to Lovberg's proposals: that the directed ion motion towards the cathode allows for a higher ion component of the current.

Also in the mid 1960s a group at General Dynamics headed by Gooding was investigating a coaxial plasma accelerator [18, 19]. They recognized the possibility of current sheets driving propellant into the electrodes as it is swept along, as well as the possibility of neutral particles being left in the wake of the sheet [18]. No investigations of these phenomena were published by this group, however.

MacLelland, MacKenzie, and Irving took both regular and Schlieren photographs of the discharge in a rail gun in 1966 [20]. Their results are similar to Lovberg's above. Figure 2.5 shows three frames from a framing camera taken of a discharge in 750 mTorr of hydrogen. The top electrode is the anode, the bottom the cathode, and the bottom frame is the earliest (the plasma is moving from left to right). A slight cant of the sheet is evident and a luminous trail is left along the cathode, especially in the middle frame.
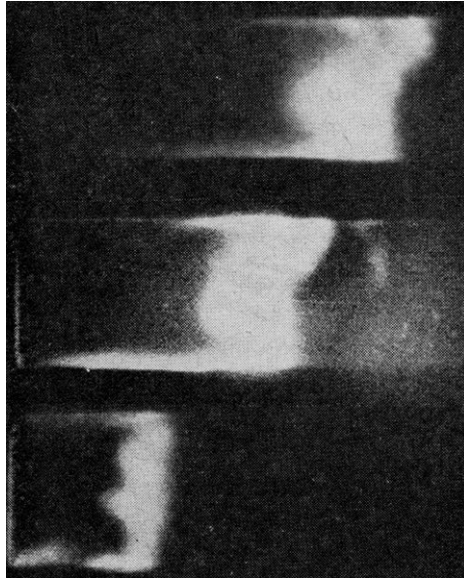
Figure 2.5: Photographs from MacLelland, MacKenzie and Irving [20]. The anode is on top and the cathode is on bottom. The conditions are: hydrogen propellant, 750 mTorr.
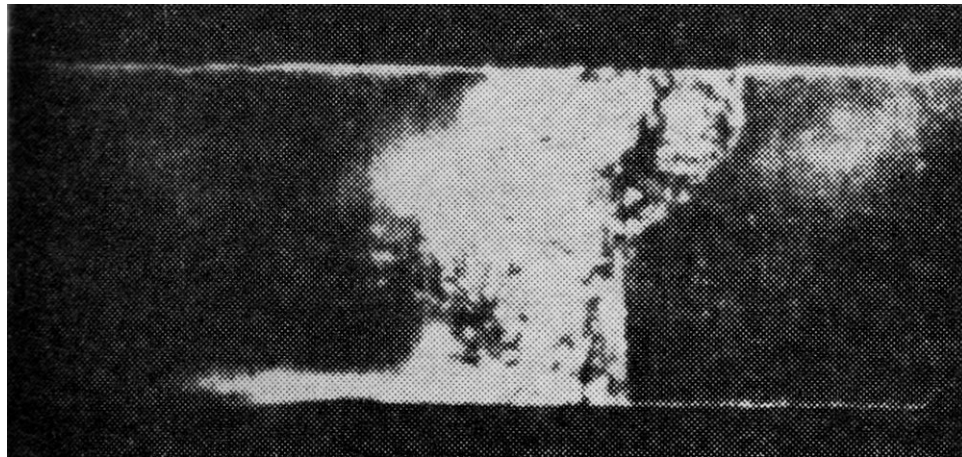

Figure 2.6: Schlieren photograph from MacLelland, MacKenzie and Irving [20]. The anode is on top and the cathode is on bottom. The bottom frame is the earliest in time and the top frame is the latest. The conditions are: hydrogen propellant, 500 mTorr.
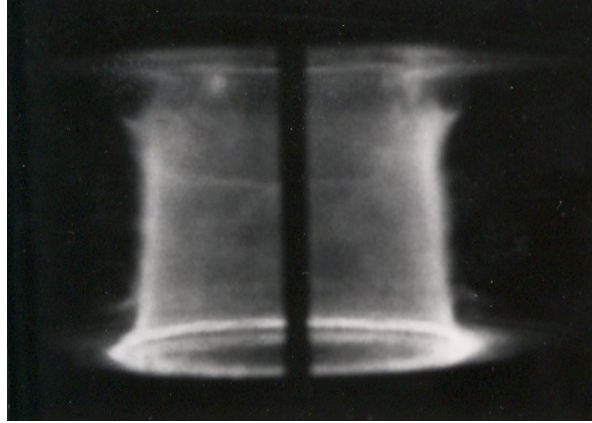
Figure 2.7: Photograph of the linear pinch device used by Burton, York and Jahn (from [21]) showing a cylindrical current sheet that is moving radial inward. The anode is on top and the cathode is on bottom. The conditions of this photograph are: argon propellant, 120 mTorr.

A Schlieren photograph of MacLelland, MacKenzie, and Irving's plasma is shown in figure 2.6. This photo is from a hydrogen discharge at 500 mTorr initial pressure. It is clear that a plasma wake is left behind along the cathode in this device. The authors themselves cite similarities to Lovberg's Schlieren photographs, and state that these photographs support the theory of a current-conducting boundary layer.

At Princeton University in the late 1960s, Jahn and his colleagues studied the cylindrical current sheet in a linear pinch device [11, 21, 22]. Figure 2.7 shows a photograph of the discharge, with a small visible plasma trail at the cathode (bottom surface).

Two interesting findings, for our purposes, are reported in 1967 by Ellis in his current sheet studies with argon propellant [23]. The first is that Ellis finds the current sheet would sometimes bifurcate near the anode of the device. The second finding is that measurements of the polarization electric field in the sheet indicated sufficient field at the midplane of the device to accelerate the ions to sheet velocity, but not at the cathode. It was inferred that the ions at the cathode were not accelerated at all.

Burton and Jahn, in 1968, argued that the ions must carry most of the current in the back part of the current sheet [21]. This was because the electric field reversed in that area to oppose electron current, but the net current density does not reverse. They attribute this ion current to a flow of ions due to the canted sheet, and also state, "as a consequence of the tilted current sheet... ions are expected to accumulate along the cathode, as has been observed by other experimenters".

York and Jahn, in 1970, found a plasma wake in their studies of the same pinch device [11]. They used piezoelectric pressure probes in axial and radial configurations in a pinch geometry accelerator. The goal of the study was to identify the structure of the current sheet. They found a spatial separation between the current sheet and the bulk of its mass. Also, they identified a "wake" region which is said to be "following the intense discharge with fractional sheet velocity". It is the wake, which can be seen in their measurements (figure 2.8) as a hump to the right of the sheet, which represents plasma or gas that has leaked through the sheet.

York and Jahn also define a sweeping parameter which is the "ratio of the entrained mass to that originally in the volume swept by the sheet" (see equation 1.1). In their experiments they calculate the sweeping parameter, Φ_{sh}, to be about 90%. This is consistent, at least from a first-order approximation, with the fact that their measured density peak in the wake (figure 2.8) is about one tenth of the measured sheet density peak.

Also in 1970 Pert studied the current sheet in a parallel-plate rail gun [24]. These studies were performed with a 100 mTorr hydrogen backfill. Although Pert claims that his current sheet is impermeable and for the most part non-canted, his measurements do show some interesting and relevant sheet conditions. He measured electron number density to be much higher near the cathode than the anode. Also, as seen in figure 2.9 which shows magnetic field measurements, Pert reports "current flow behind the current sheet and... a
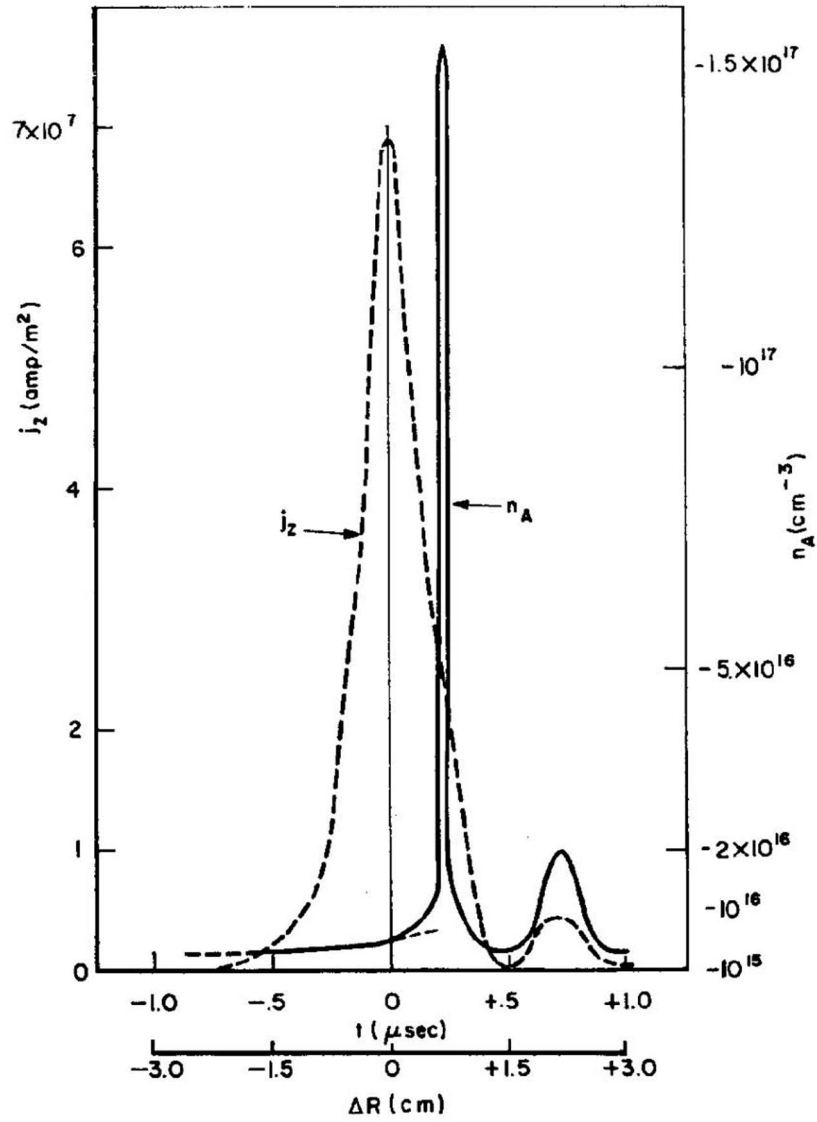
Figure 2.8: Current and density measured by York and Jahn in a linear pinch device (from [11]).
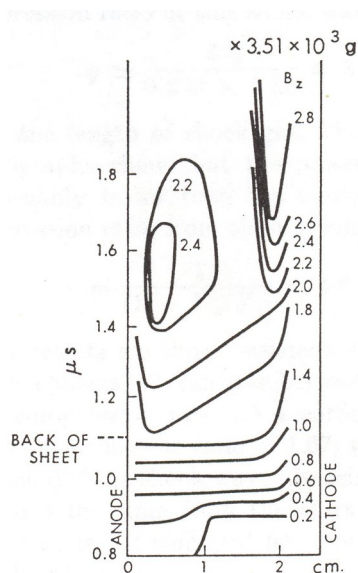
Figure 2.9: Magnetic field measurements by Pert [24]. The conditions were: hydrogen propellant, 100 mTorr.

well defined current vortex structure". The current near the cathode is clearly comparatively large as well.

York later moved on to Pennsylvania State University. From there two papers were published, with colleagues, in 1974 and 1975, that discuss pressure measurements in pinch discharges [25, 26]. Their conclusions, that are relevant to the present study, are that pressure asymmetries between the electrodes indicate a flow of ions towards the cathode. This is related, they state, to the observed current sheet tilt.

After around 1975 there was little interest in or experimentation with gas-fed pulsed plasma thrusters (GFPPTs) for many years. During this time, many researchers shifted work into quasi-steady thrusters, the predecessors of steady-state magnetoplasmadyamic (MPD) thrusters [27]. Research on ablative PPTs, using Teflon propellant, also became more popular during this time [5].

Later, in the late 1990s Ziemer began a study of lower powered GFPPTs at Princeton
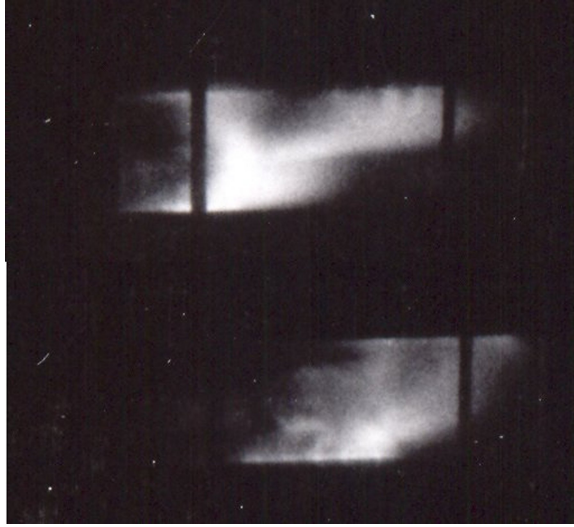
Figure 2.10: Photographs from Ziemer of the current sheet in a parallel-plate pulsed plasma thruster. The photos are taken 2 μs apart, and the top electrode is the anode. Note that these photos do not actually appear in reference [7], but they are from the same study.

[7]. Although Ziemer did not study the current sheet in detail, he does identify current sheet canting and permeability as major unresolved issues of previous studies of the devices.

Ziemer also photographed his discharge using a high-speed camera (see figure 2.10). The operating conditions of the thruster are much different from many of the earlier works. The gas is puffed into the electrode gap, and a mass of 2 μg of argon per shot is used in this photo. Also, only 4 J of energy per pulse is used, and the dimensions of the accelerator are 2.54 cm wide by 10.16 cm long with a 1.27 cm gap. Bifurcation of the current sheet near the anode is evident, as well as an obvious canting of the sheet. A possible, small plasma wake is visible along the cathode in the bottom frame of figure 2.10.

Finally, in the same laboratory but with a different apparatus, Markusic began a systematic study of current sheet canting [10, 28, 29]. This study was also the precursor to the study presented in this dissertation, and the same experimental accelerator was used in both. It is a parallel-plate device, with copper electrodes and a pulse forming network that
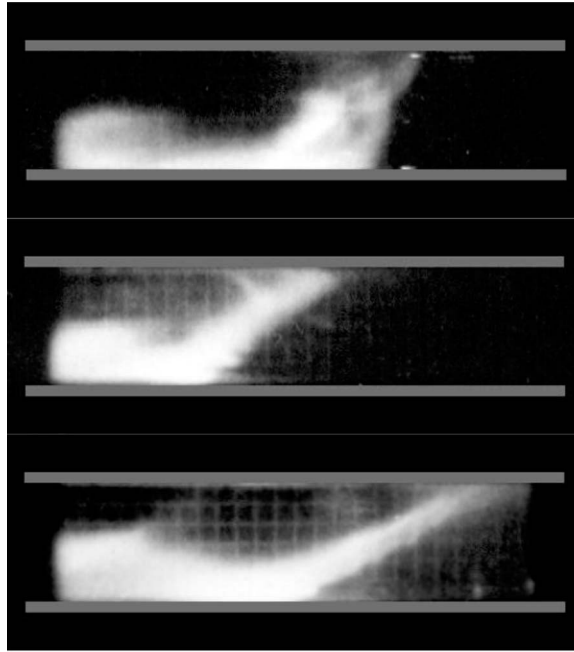
21

Figure 2.11: High speed photographs from Markusic [10]. The conditions are: deuterium, helium and neon propellants (from top to bottom), all at 200 mTorr. In each frame, the anode is on top and the cathode is on the bottom.

can be charged up to 10 kV. This accelerator is described in much more detail in the next chapter.

Although the study was focused on the canting of the current sheet, several observations related to sheet leakage were made as well. Primary among those was the visual evidence from high-speed photographs taken with the imaging system described in section 3.7. Figure 2.11 shows photographs from Markusic's study of a few different propellants. In each frame, the anode is the top electrode, the cathode is on bottom. We can see that in each case the sheet cants, with the anode leading the cathode, and there is a pronounced visual trail of plasma along the cathode.

The development of the plasma wake is even more evident in the photographs of figure 2.12. This progression of frames shows the development of the current sheet from perpen-
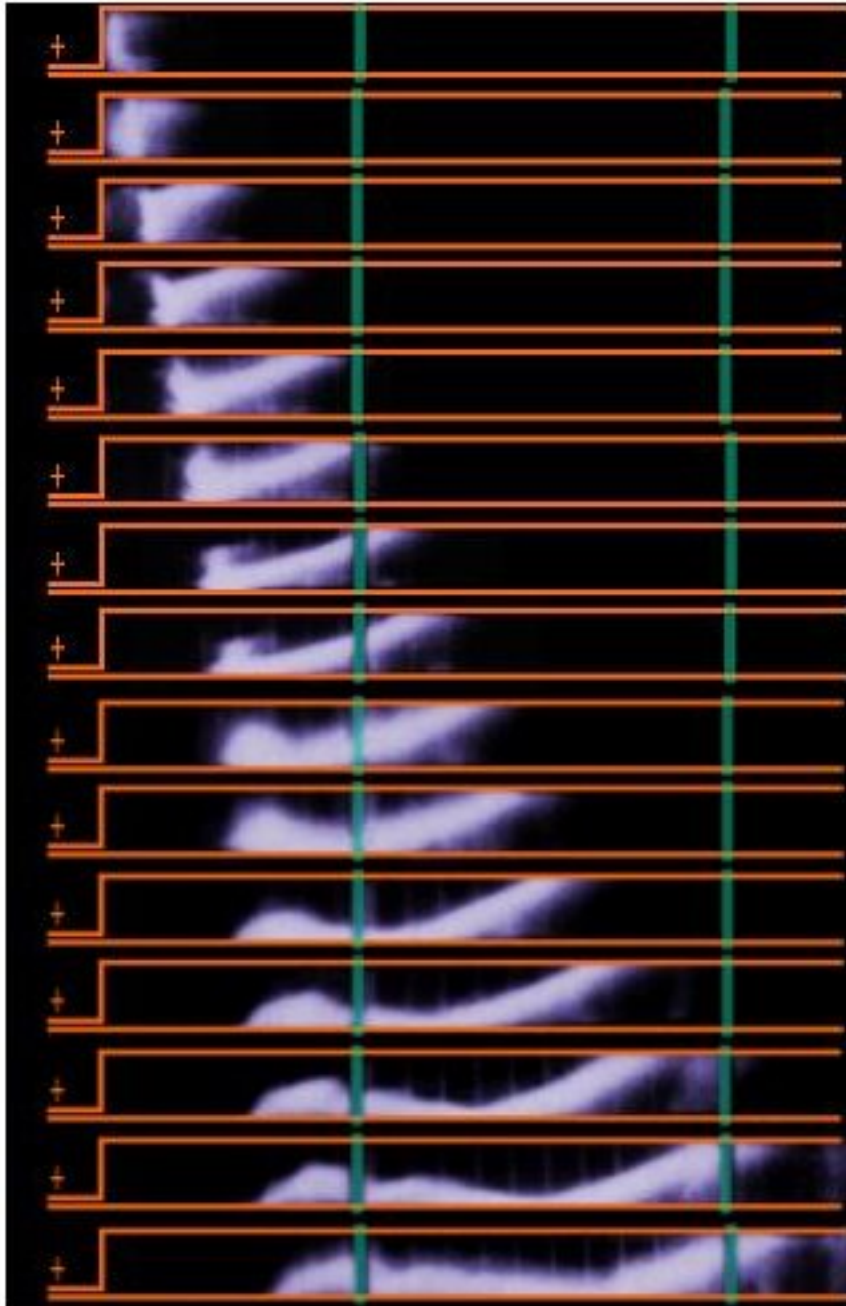
Figure 2.12: High speed photographs from Markusic [10]. These photographs are frames from a movie of the discharge [30]. Each frame is 1μs apart. The conditions were: argon propellant, 100 mTorr, 4kV. In each frame, the anode is on top and the cathode is on the bottom.
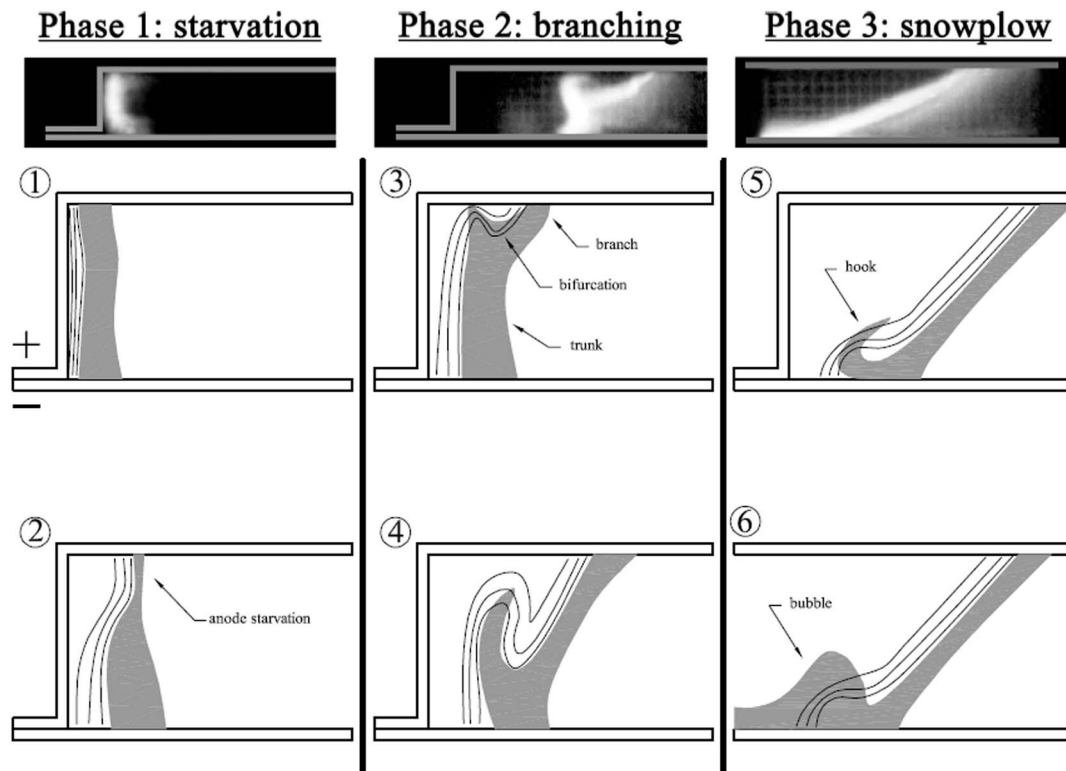
Figure 2.13: A schematic, from reference [10], that illustrates the development of the current sheet into a canted structure with a wake following it.

dicular to canted, and the development of the plasma wake which steadily grows as the sheet moves. Also a bifurcation of the sheet is visible in the early frames.

Markusic observed that canting occurred in all propellants tested, but that lower atomic mass propellants had smaller canting angles. In the same device used in this study, he measured the canting angles of discharges in seven different propellants and three different pressures each [28].

Markusic proposed a theory of current sheet canting, which relates to the bifurcation of the sheet. A brief overview of his theory is presented here, and is illustrated schematically in figure 2.13. At early times, the sheet forms perpendicularly to the electrodes, but has

little velocity yet. Through some mechanism, possibly diamagnetic drift, the plasma near the anode becomes depleted, so that the density is lower there. This allows the magnetic field, which is normally contained behind the current sheet, to be able to push through the plasma near the anode. This creates a second path of current ahead of the sheet, called the "branch". This bifurcation of the sheet and magnetic field structures has been observed by other researchers as well [7, 16, 23].

Once the branch has formed it moves ahead of the "trunk" (the original planar sheet) and also expands to take up more and more of the electrode gap. Eventually the canted branch spans the entire gap from anode to cathode and effectively becomes the new canted sheet. The remnant of the trunk is left behind. The canting of the sheet is highly relevant to the problem of current sheet leakage. As Markusic states [10]:

> The tilt of the current sheet causes it to exert a cathode-directed component of the $\mathbf{J} \times \mathbf{B}$ force density on all of the propellant which is subsequently swept up. As a result, the propellant is preferentially directed toward the cathode, where it accumulates. The "mass-funnelling" to the cathode may cause elevated plasma pressure along the cathode - leading to expansion of the propellant into the region *behind* the current sheet. A structure in the form of a plasma "bubble" behind the current sheet could form...

This is consistent with the observations of other researchers who also noted the potential for a canted sheet to direct ions towards the cathode.

The sum of the knowledge of previous researchers discussed above is the starting point for our study of the problem of current sheet mass leakage in gas-fed pulsed plasma thrusters.

25

2.2   Summary of Previous Research

A few researchers in the past have identified current sheet mass leakage via a plasma wake along the cathode. These observations have been made in a variety of devices and under a variety of conditions. Current sheet leakage has by no means been observed in all devices or all conditions, however. The most common observations associated with this phenomenon are:

- A bifurcation of the current sheet into two current paths near the anode at early times.

- Canting of the current sheet, with the anode attachment leading the cathode attachment.

- A visible trail of plasma along the cathode.

- A possible need for cathode directed ions to carry current, with canting cited as the cause of the ion flow.

Overall, a picture has developed of the current sheet development that leads from a bifurcation of the sheet attachment at the anode to a canted sheet that directs ions towards the cathode, possibly carrying current. Despite this level of understanding, however, none of the previous researchers studied the leakage problem in detail and none of them discussed or measured the effect of leakage on the performance of the device.

Chapter 3

Experimental Setup and Diagnostics

The experimental apparatus and diagnostics used are discussed in this chapter. The experimental setup includes the vacuum chamber and associated vacuum equipment, the power supply and pulse forming network, the triggering circuit for the accelerator, shielding from electromagnetic noise, and the accelerator itself.

The diagnostics that were employed in our experiments include a current transformer for measuring the total current in the circuit, a high speed camera for taking photographs, magnetic field probes to measure the magnetic field in the device, a laser interferometer for measuring electron number density, a spectrometer to measure the electron temperature, and a momentum plate to measure the impulse of the discharges.

3.1   The Experimental Accelerator

The device used in this study is the same as that used by Markusic in his current sheet canting studies [10]. The accelerator is not an actual thruster, but was constructed with ease of diagnosis in mind (see figure 3.1). It is a parallel-plate accelerator with glass sidewalls. The anode and cathode are made of copper and the volume of the acceleration region measures
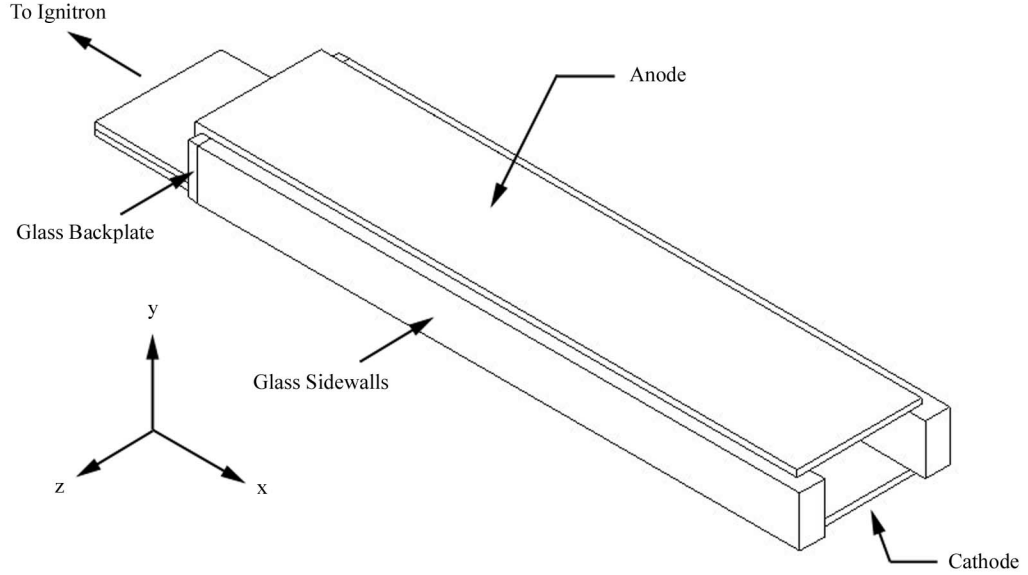
Figure 3.1: Schematic of the experimental accelerator with planar copper electrodes and Pyrex sidewalls.

60 cm long and 10 cm wide, with a gap of 5 cm between the plates. The propellant fill was performed by a uniform gas fill; there are no gas inlet valves.

The accelerator was placed in a vacuum tank for testing. This accelerator design provides easy diagnostic access for interferometric laser probing through the glass sidewalls, and magnetic field probe access down the barrel of the device.

3.2   Vacuum System

The vacuum tank used in these experiments is a 0.9 m diameter, 1.8 m length plexiglass chamber [31]. A drawing of this tank, with associated equipment is shown in figure 3.2. Unlike a metal chamber, the plexiglass does not interfere with the electromagnetic fields created in the device. Our accelerator was operated with a uniform backfill, therefore a

good pumping system was required to evacuate the tank of air before the propellant was fed in. The tank was pumped with an Welch 1398 Dual-Seal roughing pump to a level on the order of 10 mTorr. Then a CVC PMC-6B diffusion pump was used to pump the tank down to a level on the order of 10^{-4} Torr. When the air in the tank was sufficiently evacuated, a gate valve was used to close off the diffusion pump most of the way. Propellant gas was then let into the tank, regulated by a needle valve. A balance between the propellant feed rate and the pumping rate was used to establish a constant pressure in the tank. The pressure was measured using a MKS 626A02TBE Baratron gauge. This gauge was disconnected during firings to avoid arcing between the accelerator and the gauge during the discharge. The pressure was checked after every firing, however, and adjusted if the pressure had drifted away from the desired pressure.

3.3   Charging Circuitry

The energy supplied to the discharge while firing the accelerator is stored in a pulse forming network. The pulse forming network was constructed to supply a nearly constant current during the acceleration of the current sheet and consists of ten Maxwell 35385 10 μF capacitors in series with 100 nH inductance between each capacitor. These capacitors are rated up to 10 kV, however we only used them up to 9 kV in our experiments. The pulse forming network was charged with a Del Electronics power supply.

The voltage was measured with a 1000:1 voltage probe. This voltage probe was calibrated to ensure accuracy to 0.1%. While the voltage was raised on the capacitor bank, it was held off of the accelerator plates by an ignitron switch. When the voltage was at the desired level, it was switched quickly onto the accelerator electrodes using the ignitron, which was itself triggered by a separate triggering circuit.

The pulse forming network, charged to 9 kV, was able to provide an almost flat current
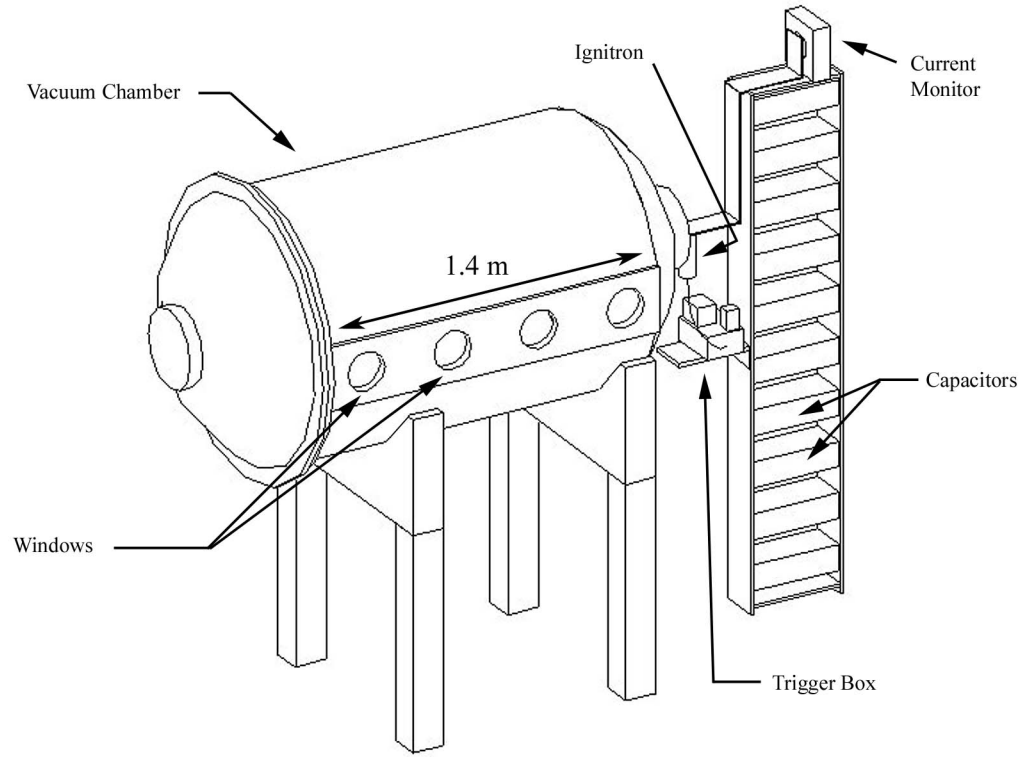
Figure 3.2: Schematic of the experimental vacuum chamber facility. The pulse forming network is shown on the right. A ladder-like configuration of the capacitors, it stores the charge for the experimental discharges.

of about 60 kA for about 25 μs, with a risetime on the order of 2 μs, as shown in figure 3.3. After about 28μs, the circuit current reverses, which, as we will see later, can cause a second current sheet to form at the breech.

3.4   Triggering Circuitry

The voltage had to be switched onto the accelerator electrodes in a safe and repeatable manner. The solution was to use a National Electronics NL-7703 ignitron. An ignitron uses a vacuum tube to hold off the voltage. At the bottom of the tube is a pool of liquid
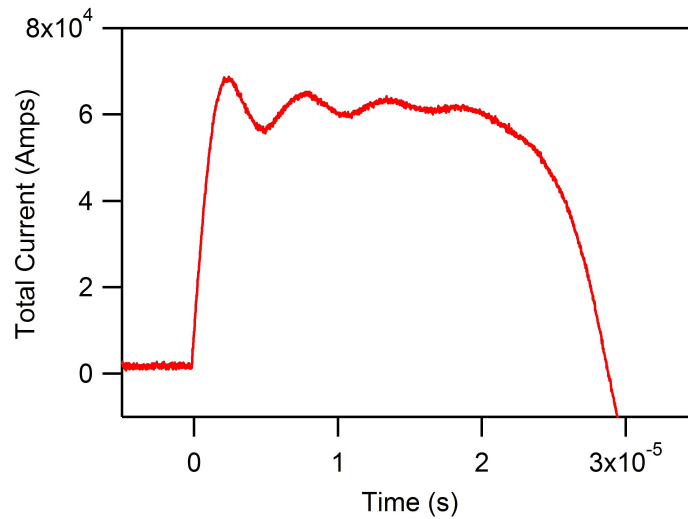
Figure 3.3: Example total current trace: argon, 9 kV, 100 mTorr.

mercury. When the ignitron anode, which is immersed in the mercury, is supplied with enough voltage, it vaporizes enough of the mercury to fill the gap with a conducting gas. Once the gap is switched, the current flow through the ignitron is quite quick. This allows for a short rise time of the current in the device, which is important for the gas breakdown process.

The ignitron is supplied with a 1500 V pulse by a trigger box which was made for this experiment. There are two interesting features of this device that are worth mentioning. The first is that the trigger box is isolated from the power outlet where it gets its power, by an isolation transformer. This prevents electromagnetic noise from the ignitron and trigger box from having a direct path to measurement devices through the ground.

The second feature of the trigger box is that it is isolated from the user-operated trigger switch with a fiber optic cable. This protects the user from the high voltage used to trigger the ignitron. The full trigger circuit is shown in a block diagram in figure 3.4.
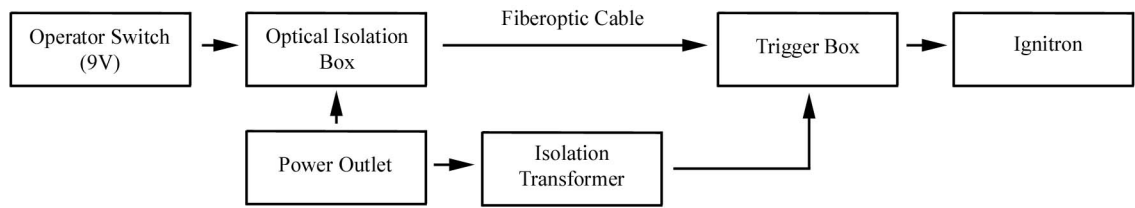
Figure 3.4: Block diagram of the trigger circuit.

3.5 Shielding

Several considerations were made in this experiment to eliminate noise. Due to the high energy pulse of the discharge, a considerable amount of electromagnetic noise is radiated. To prevent the high voltage pulse from creating ground loops, or pulling the ground up to a floating voltage, a ground plane was used. This ground plane is a copper floor covering most of the experimental room which is connected to a large cable that is buried in the earth. All equipment used this same ground. The power outlets used by the experiment were also grounded to this ground plane, and isolated from the wall outlet ground by a Topaz P1002-21 isolator and line noise suppressor.

All equipment that was sensitive to noise, such as computers, oscilloscopes, and laser detectors were housed in a Faraday cage. Signals entering the cage were directed through feed-throughs. This eliminated noise picked up in the cables.

3.6 Current Transformer

A Pearson Electronics 301X current transformer was used to measure the total current vs. time. This current transformer was placed on the transmission line between the capacitor bank and the ignitron. The signal from the transformer is a voltage directly proportional

to the current (1 A = 10 mV) and is accurate to within 1%. This signal was reduced by two 20 db attenuators, so that the final signal was only 1% of the transformer output. The total current was measured in every firing of the accelerator. The rise of the current signal was used to trigger the oscilloscope and other instruments.

3.7   Photography

High-speed photographs were obtained using a Hadland Photonics Imacon 792LC fast-framing camera. This camera was used with a module that allowed up to eight frames, taken two μs apart, to be imaged on a single polaroid film. The exposure time of each frame was approximately 0.4 μs. Therefore, with a sheet velocity of around 3 cm/μs, there will be some blurring of the sheet in the photographs, on the order of 1 cm.

A Stanford Research Systems DG535 digital delay generator (DDG) was used to trigger the Imacon camera. This DDG was itself triggered by the rise of the measured current in the accelerator, in the same manner as the oscilloscope is triggered. The camera also outputs a monitor signal which indicates the timing of the frames. This was used to verify the delay of the photographs relative to the current rise.

The camera was placed outside of the vacuum tank, looking in through a glass window. We photographed the discharge perpendicular to the electrodes, looking through the glass sidewalls of the accelerator. Different filters were used in front of the camera lens to capture light of interest in that test. We used three filters in our studies: one to look at an argon ion line, one for a neon ion line and one for a neon neutral line. The argon ion line $3p^44s$ - $3p^4(^3P)4p$ was captured at 487.99 nm wavelength with a Ealing-TFP 488 nm wavelength interference filter. The two neon line filters are discussed further in appendix B.
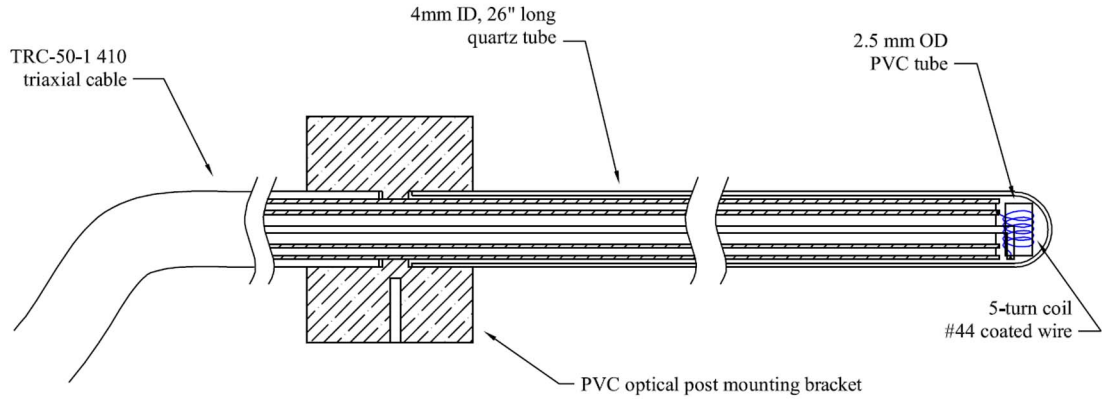
Figure 3.5: A schematic of a B-dot probe used in our experiments. This drawing is from reference [10].

3.8 Magnetic Field Probes

B-dot probes are probes which measure a voltage proportional to $\dot{B}$, the time varying magnetic field [32]. The probe tips consist of small coils of wire. The changing magnetic field through these coils induces a voltage on the wire. In our experiment there is a significant magnetic field in only one direction (the $-z$ direction, or into the page in our diagrams and pictures). The coils were thus aligned to measure the changing magnetic field in this direction. A diagram of the B-dot probes used is shown in figure 3.5.

The 0.25 cm diameter coils are encased in a quartz tube that protects them from the plasma. These tubes, which are inserted into the accelerator from the downstream direction, are 0.318 cm in diameter. Inside the quartz tubes the signal was carried on triaxial cable. The outer conductor was used as a shield to prevent the cable from picking up electromagnetic signals. The two coaxial inner conductors were used to transmit the $\dot{B}$ signal out of the vacuum tank (using triax feed-throughs) and to a Faraday cage. The $\dot{B}$ signal, which is obtained from these probes, is integrated numerically to obtain traces of $B(t)$ at the specific location of the probe tip.

The quantitative data to be determined from these measurements are twofold. First, the arrival of a steep magnetic field rise at a point will be taken as evidence of the arrival of the current sheet. From this knowledge at many points in the accelerator, the time-resolved velocity of the current sheet may be determined. Second, the value of the magnetic field can be resolved over a grid of measurement points in the accelerator. This also allows the determination of current density contours. Perhaps the most valuable information we can obtain from the magnetic field measurements is a clear picture of the development of current structures in the sheet at early times, obtained by taking the curl of B.

3.9   Laser Interferometry

We have used a laser interferometer constructed by Markusic to measure electron number density [10]. A Spectra-Physics 106-1 20 mW HeNe laser was employed in a Mach-Zehnder type configuration. This means that the laser beam was split into a scene and reference beam, which were steered into their respective paths and recombined on a detector.

The scene beam was directed into the tank, made a single pass through the accelerator, and was directed out of the tank again (see figure 3.6). The path through the accelerator was perpendicular to the electrodes (in the z dimension), entering through one glass sidewall and exiting through the other side. The reference beam was directed around an optical table outside of the tank in a path having a length approximately equal to the scene beam's path length.

The laser, detector and electronics for this interferometer were placed in a Faraday cage near the tank. This was to prevent electromagnetic noise from entering the measurement system.

The interferometry system used in these studies was of a heterodyne, quadrature type.

A similar system was used by Spanjers et. al. in a plasma opening switch [33]. A heterodyne system is one in which the two beams are given an imposed phase difference between them. This is accomplished with an Intra-Action Corp. AOM-405 Acousto-Optic Modulator, which served to both separate the beams spatially and give them a 40 MHz difference. Then, when the two beams are recombined, the detector picks up the 40 MHz modulation. This detected signal is compared to the reference 40 MHz signal that was imposed on the beams to begin with. The advantage of this heterodyne approach is that only amplitude variations due to phase change in the detected signal are picked up, and not amplitude variations due to attenuation or refraction of the beam [10].

The detector used is a Thor Labs PDA155 detector. The signal from this detector and the reference signal from the 40 MHz driver are compared in a quadrature phase detector. This involved using a mixer to determine the sine and cosine of the phase of the signal. Knowing both the sine and cosine of the phase indicates whether phase changes are positive or negative. This is the advantage of the quadrature system over a simpler Mach-Zehnder interferometer where it is sometimes impossible to tell a negative phase jump from a positive one.

In our particular configuration of the interferometer, as shown in figure 3.6, we employed a single pass of the scene beam through the accelerator. This was due to the problems encountered by Markusic using a double-pass configuration [10]. The problem was that in some cases where the plasma density in the sheet rises very quickly, the phase change occurs faster than the modulation frequency of the heterodyne system can detect. By using a single pass, we expect to record less phase "jumps" through π or $-\pi$. Unfortunately this did not completely solve the problem and we shall see that there were areas of the accelerator that could not be probed with interferometry because the density rise was too quick.
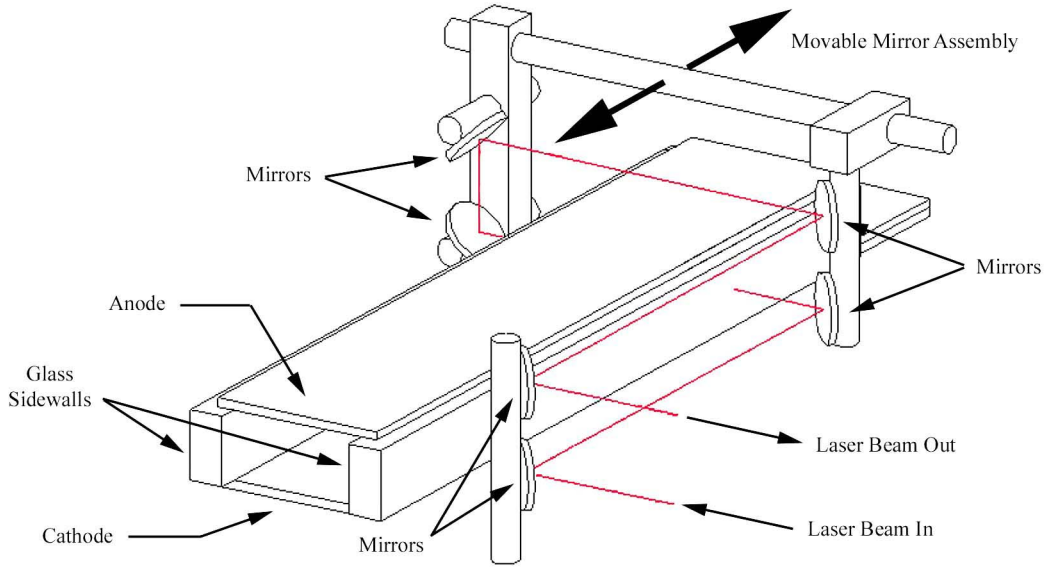
Figure 3.6: Schematic of the interferometry system inside the vacuum tank. The moveable mirror assembly allowed for repositioning of the beam location with a motor operated from outside the vacuum tank.

Another change to the configuration that we made was to place the scene beam mirrors in the tank on a movable platform (see figure 3.6). The movable mirrors allowed us to move the position of the laser beam in the accelerator without opening the vacuum tank. The beam was carefully aligned and the platform could be moved by small known distances allowing access to an entire horizontal row of data points in the accelerator.

The quadrature phase detector output the sine and cosine of the instantaneous phase, ϕ, of the interferometer signal [10]. These outputs were used to determine the phase through the relation,

$$\phi = \arctan\left(\frac{\sin\phi}{\cos\phi}\right).$$

(3.1)

The phase angle can be related to the electron number density in the plasma by the formula [34, 35],

$$n_e = \frac{2cn_c}{\omega d}\Delta\phi. \tag{3.2}$$

where c is the speed of light, ω is the frequency of the laser and d is the path length of the laser beam through the plasma, and n_c is the so-called cutoff density, above which the beam is reflected out of the plasma, which is defined as:

$$n_c \equiv \frac{\omega^2 m_e \epsilon_0}{e^2}. \tag{3.3}$$

For a HeNe laser interferometer, equation 3.2 reduces to,

$$n_e = 5.61 \times 10^{20}\frac{\Delta\phi}{d}. \tag{3.4}$$

Thus the electron number density of the current sheet can be determined through laser interferometry, provided that the assumptions implicit in the above analysis are met.

3.9.1 Interferometry Assumptions

The assumptions that allow the determination of the electron number density through interferometry, by equation 3.4, are:

- The contribution of bound electrons to the index of refraction is negligible.

- The path length changes due to vibration and thermal drifts are negligible compared to the effective path length change due to the plasma ($\Delta d/d << n_e/n_c << 1$).

- The effective path length change due to refractive bending is small compared to that due to the plasma index of refraction ($dn_e/dx << \sqrt{12n_e n_c}/d$) [34].

- The plasma is uniform along the path length, d, of the laser beam through the plasma.

- The plasma frequency is much less than the laser frequency ($\omega_p << \omega$).

- The cyclotron frequency is much less than the laser frequency ($\omega_c << \omega$).

- The Coloumb collision frequency is much less than the laser frequency ($\nu_{ei} << \omega$).

Each of these assumptions is met in this experiment. The first assumption, that bound electrons contribute negligibly to the index of refraction compared to the contribution from free electrons is easily met if the plasma is even very slightly ionized.

The second condition was met, experimentally, because the time scale of the current sheet propagation, over which the density was measured, was small compared to the time scale of vibrations of the optics. This was verified by measuring the density on longer time scales where the effect of vibrations became obvious and detrimental.

The third assumption, that refractive bending is small, is verified by the equation listed above. In our experiment $dn_e/dx \approx 10^{24}$ m^{-4}, while $\sqrt{12 n_e n_c}/d \approx 10^{26}$ m^{-4}.

The fourth assumption above, that the plasma is uniform along the path length of the laser, is the most difficult assumption to verify in our experiment. In section 4.3, we show measurements of the magnetic field in the z direction that show some drop in the magnetic field towards the edges of the plasma (near the glass sidewalls). Visually, the current sheet fills the entire width of the electrodes. We expect that the density does not change significantly from the center to edge, but in the worst case the interferometry measurement will represent an average density in the z direction across the electrode width.

The last three assumptions are easily verified. The expressions in the parenthesis above reduce, respectively, to:$n_e << n_c$, $B << 10^4$ Tesla, and $n_e << 10^{54}(kT_e)^{3/2}$. Each of these conditions is easily met in our experiment.

3.10　Line Emission Spectroscopy

A spectrometer has been used in the current study to measure the electron temperature of the plasma in the current sheet. The same technique was employed by Markusic to make a single measurement of the electron temperature in an argon current sheet at 75 mTorr pressure, which was 2.4 ± 0.2 eV [10]. We have measured the electron temperature in neon discharges over a range of pressures as will be discussed further in section 6.2.2.

The Boltzmann plot method of determining the electron temperature has been employed. This method, described in detail in the next subsection, requires that the plasma is in partial local thermodynamic equilibrium, and involves the comparison of the line intensities of many emission lines from the plasma. Because neon ions have many emission lines in close proximity and in the range of our spectrometer, neon was selected as the best candidate for making electron temperature measurements.

The spectrometer used was a Spex 1269 one meter spectrometer. The grating used had 1200 grooves per millimeter and the spectrometer had a useful range of 350 to 850 nm. The spectral lines were captured with a Princeton Instruments 576 Intensified CCD camera. The camera was gated with a Princeton Instruments PG-200 pulse generator. The exposure time used in our experiments was 100 ns. The spectrometer viewed the current sheets from the side, midway between the anode and cathode with the projection of the slit effectively imaging a few centimeters in the axial direction. During the gate time the expected movement of the current sheets is very small. Thus the spectrometer captured a snapshot of the middle of the electrode gap with resolution of a few cm in the x direction. Figure 3.7 shows the extent of the line of measurement with reference to a photograph of a discharge in neon.

The CCD array of the camera was able to capture about 10 nm of the spectrum in each shot. Because neon ion lines are close together, we were able to capture 2 - 4 useful lines

at a time. These measurements were repeated five times before moving to another part of the spectrum to capture more lines. Therefore for a given pressure condition the intensities of 6 different lines were measured, 5 times each. The intensities that were used were from the middle of the current sheet's width, where the lines were the brightest. These measured intensities were used to construct a Boltzmann plot and thus the electron temperature was determined.

3.10.1 The Boltzmann Plot Method

The simplest way in which the electron temperature may be determined through spectroscopy is by using the Boltzmann plot method on a single species of the plasma. Although other techniques are available, they often have stricter requirements on the plasma conditions [36]. The Boltzmann plot method requires that the plasma be in partial local thermodynamic equilibrium (LTE) and that it be optically thin [36]. Partial LTE is a less stringent condition than complete LTE and means that only the observed states must be in a Boltzmann equilibrium.

The principle of this technique is described in reference [36], but a brief summary is given here. If the free electrons in a plasma are in equilibrium (i.e., have a Maxwellian distribution of speeds), then the atomic species with which they are collisionally coupled will be in excitation equilibrium, that is, the bound electrons will be in a Boltzmann energy distribution. The actual distribution of excited states in a plasma is revealed when electrons in excited states relax to lower energy states and radiate light. By measuring the intensity of this light, we can infer the population of a particular upper state. Carrying out this procedure for many different transitions, we can determine the energy distribution of the bound electrons. Knowing this distribution, we can calculate the temperature of the free electrons needed to achieve the measured distribution of excited states.
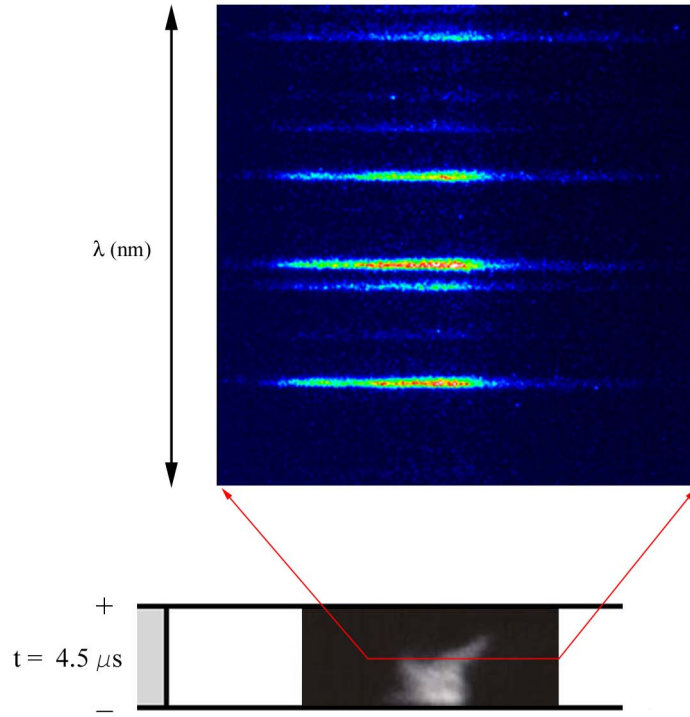
Figure 3.7: Illustration of the horizontal length of the line of projection of the spectrometer slit on the current sheet. The photograph is taken in neon at 100 mTorr, with a 369.4 nm filter on the camera, at the discharge time of 4.5 μs. The spectroscopy lines are taken in a discharge at the same conditions and same time, and the 369.4 nm line is the lowest line in the spectrometer image.

For an optically thin plasma of depth d along the line of sight, the spectrally integrated emission line intensities are given by [37]:

$$i_{nm} = \int I_{nm}(\omega)d\omega = \frac{\hbar\omega_{mn}}{4\pi}A_{nm}\int_0^l N_m dx \approx \frac{\hbar\omega_{mn}}{4\pi}A_{nm}N_m d, \tag{3.5}$$

where ω_{mn} is the frequency of the emitted light, A_{nm} is the transition probability between levels n and m, and N_m is the population of level m.

The population of the mth energy level is then given by the Boltzmann distribution:

$$\frac{N_m}{N} = \frac{g_m}{Z_a}e^{-(E_m/kT_e)}, \tag{3.6}$$

where g_m, Z_a, and E_m are the statistical weight, partition function and energy of the mth level of the atom, respectively. Combining equations 3.5 and 3.6, we find

$$i_{nm} = \frac{\hbar\omega_{mn}A_{mn}g_m N l}{4\pi Z_a}e^{-(E_m/kT_e)}. \tag{3.7}$$

Rearranging terms we find that the equation can be written in the linear form

$$y = ax + b \tag{3.8}$$

where,

$$
\begin{aligned}
y &= \quad ln\left(\frac{i_{nm}}{\omega_{mn}A_{mn}g_m}\right) \\
a &= \quad -\frac{1}{kT_e} \\
x &= \quad E_m \\
b &= \quad ln\left(\frac{\hbar N l}{4\pi Z_a}\right).
\end{aligned} \tag{3.9}
$$

With knowledge of the parameters ω_{mn}, A_{mn}, g_m and E_m for each transition and a measurement of the transition's intensity, a plot of y versus x is constructed and linear fit

43

λ_{mn}	Transition	E_m	ω_{mn}	A_{nm}	g_m
[Å]	(Level m → Level n)	[10^{-18} J]	[10^{15} s^{-1}]	[10^8 s^{-1}]	
3568.500	$(^1D)3p^2F^0_{7/2} \rightarrow (^1D)3s^2D_{5/2}$	5.451	5.279	1.40	8
3574.183	$(^1D)3p^2F^0_{5/2} \rightarrow (^1D)3s^2D_{5/2}$	5.450	5.270	1.30	6
3574.612	$(^1D)3p^2F^0_{5/2} \rightarrow (^1D)3s^2D_{3/2}$	5.450	5.270	0.10	6
3694.212	$(^3P)3p^4P^0_{5/2} \rightarrow (^3P)3s^4P_{5/2}$	4.890	5.099	1.00	6
3709.620	$(^3P)3p^4P^0_{1/2} \rightarrow (^3P)3s^4P_{3/2}$	4.899	5.078	1.10	2
3713.080	$(^3P)3p^2D^0_{5/2} \rightarrow (^3P)3s^2P_{3/2}$	4.986	5.073	1.30	6
3727.105	$(^3P)3p^2D^0_{3/2} \rightarrow (^3P)3s^2P_{1/2}$	4.996	5.054	0.98	4

Table 3.1: Atomic spectral data for some neon ion lines (Ne II). All data are from [38].

of the experimental data is computed. The slope of this line (a) gives the temperature. The necessary constants for each line used in this analysis are listed in table 3.10.1.

3.11   Momentum Plate

The total impulse of the device is the impulse supplied by the sheet and wake. A momentum plate was constructed to measure the impulse of the discharge and is shown in figure 3.8. Also known as a ballistic pendulum, the momentum plate is a method of measuring thrust or impulse of a thruster when a thrust stand cannot be used. Although a momentum plate is not as reliable as a thrust stand because of questions about interaction between the plasma and plate and reflection of plasma off of the plate, in our case it was the most convenient way to measure impulse, as the accelerator was built with a low-inductance connection to the pulse forming network and cannot be mounted on a thrust stand. Momentum plates of various designs have been used by researchers in the past to measure the impulse of pulsed plasmas [39, 40, 41, 42, 43, 44, 45, 46, 47].
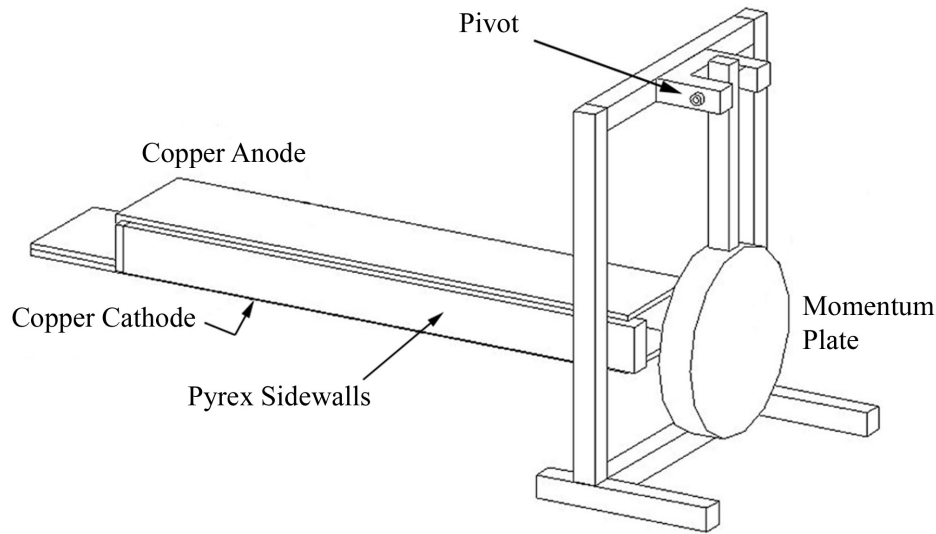
Figure 3.8: Schematic of the accelerator and momentum plate.

The momentum plate is a simple device. A flat plate attached to a pendulum arm is placed in front of the accelerator device. When the plasma discharge hits the plate, it imparts its momentum to the plate. This momentum is measured by measuring the plate's response. The motion of the plate is compared to its motion under a calibration, when it is struck with a known impulse.

For our measurements we constructed a plexiglass momentum plate that was 20 cm diameter. The plate was positioned a few cm away from the end of the electrodes. It was hung vertically on a pendulum arm of 28 cm length. The stainless steel ABEC-5 6085A bearings of the pendulum arm were selected to be as frictionless as possible to ensure a free swinging plate.

The plate, arm, and supporting structure were constructed out of plexiglass to avoid possible problems of arcing to the electrodes, or electromagnetic field influence on the plate motion. The plexiglass was able to handle the plasma impacts well; after many tens of shots there were no visible signs of erosion on the plate.

We measured the position of the plate with a laser positioning system. A laser beam was aimed at a mirror attached to the back side of the plate, and was deflected to a sensor placed outside of the vacuum tank. When the plate moved, the sensor recorded the beam movement as a voltage.

The calibration of the momentum plate was carried out as follows. The plate was positioned in place for testing, with the laser positioning system recording its position. A separate test pendulum was then placed in front of the plate. The test pendulum included a Piezotronics PCB 208A02 force sensor on its tip. This test pendulum was controlled by an electromagnet and could be set to a specific angle, released, impact the plate, and recaptured by the magnet so it would not continue swinging and impact the plate more than once. When the pressure sensor impacted the plate, the pressure vs. time signal was recorded, as well as the position vs. time of the swinging plate. Typical examples of the pressure trace and plate position trace are shown in figures 3.9 and 3.10, respectively.

To obtain the impulse of the test pendulum's impact, the pressure vs. time traces were integrated. Note that the impact time of the test pendulum is much less than the time scale of the swinging of the momentum plate, so that the impact can be treated as instantaneous. By changing the starting angle of the test pendulum, we were able to test the momentum plate's response to a range of impulses. The calibration impulses were selected to be in the expected range of the impulses of the discharges.

By plotting the momentum plate response (in units of peak voltage measured by the sensor) vs. impulses of the test pendulum, we can obtain a calibration curve for the system. This curve is shown in figure 3.11, and shows that the pendulum has a linear response to the impulse. This is because the momentum plate pendulum has almost no friction inhibiting its motion, and that the impulse is effectively instantaneous.
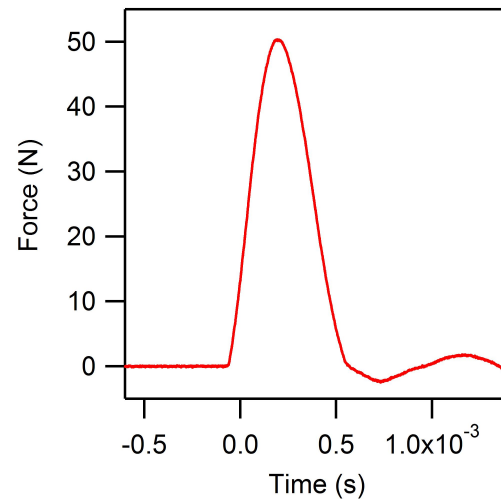
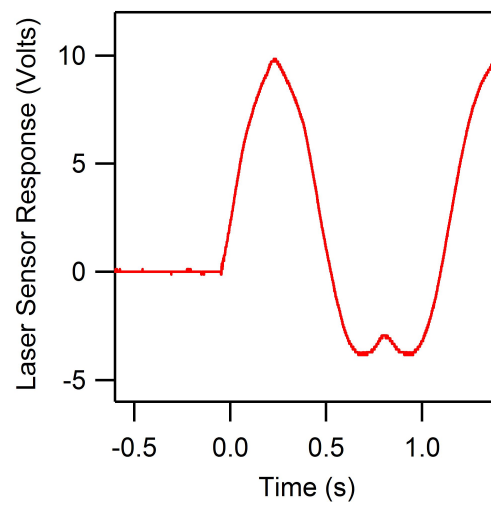Figure 3.9: Typical Pressure Sensor Response.
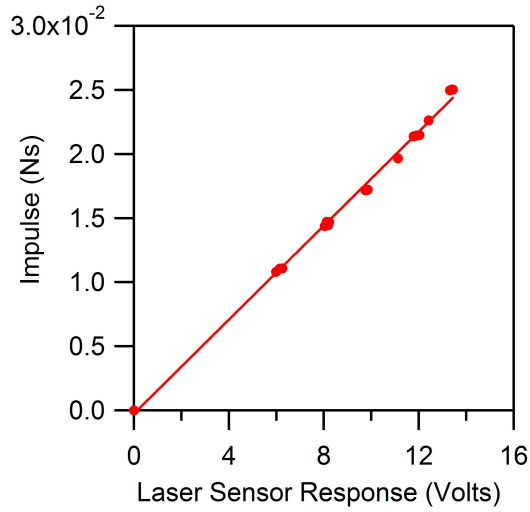

Figure 3.10: Typical Laser Sensor Response.

Figure 3.11: Pendulum Calibration Curve.

3.11.1 Momentum Plate Assumptions

There are a few questions about the ability of the momentum plate to capture the momentum of the plasma sheet. Researchers in the past have raised doubts about this type of measurement's ability to accurately determine the impulse of the plasma [39, 40]. Still, the inaccuracy of the momentum plate measurements is likely to be only on the order of a factor of 2, not an order of magnitude. We have been careful, also, to verify several assumptions about the operation of the momentum plate. The assumptions that need to be made are listed below, and each is subsequently addressed.

- The plasma strikes the plate instantaneously (on the time scale of the motion of the plate).

- All of the plasma impacts the plate.

- The plasma impacts the plate perpendicularly to the plate's surface.

- The electric and magnetic fields from the discharge do not affect the motion of the

48

pendulum.

- The fraction of momentum that backscatters off of the plate is known.

The first assumption above, that the plasma strikes the plate instantaneously is straightforward. The time scale of the plasma impact is microseconds while the time scale of the momentum plate's response is seconds.

The second and third assumptions, that all of the plasma hits the plate and that it does so without much of an angle to its impact were examined with high-speed photography. Using the Imacon camera, we examined the impact of the plasma on the plate under two conditions: argon, 9 kV, 100 mTorr and argon, 9 kV, 300 mTorr. A series of photographs from these condition are shown in figures 3.12 and 3.13, respectively. In each frame of these photographs, the left edge is centered on the accelerator exit, while the right edge is centered on the momentum plate. The frames are of an approximately 3 cm by 15 cm area, which is large compared to the 5.08 cm exit, but smaller than the 20 cm momentum plate. Each frame is taken 0.5μs apart.

We can see clearly from these photos that all of the plasma impacts the plate, as should be expected since the plate diameter (20 cm) is much larger than the 5 cm by 10 cm accelerator exit. It also appears that the plasma comes straight out of the accelerator and impacts the plate straight on. This was a concern because of the tendency of the plasma to balloon out of the exit of the accelerator. However, with the plate merely 5.7 cm away from the exit, it appears that the plasma does not have enough room to expand significantly.

The fourth assumption is that the electric and magnetic fields of the discharge do not affect the motion of the pendulum. We have constructed the pendulum from plexiglass to minimize interactions, however, it is still possible that the plate could develop a surface charge, which could be pushed by the fields. Any possible interaction of this sort would be quite small compared to the direct force of collisions, however [40].
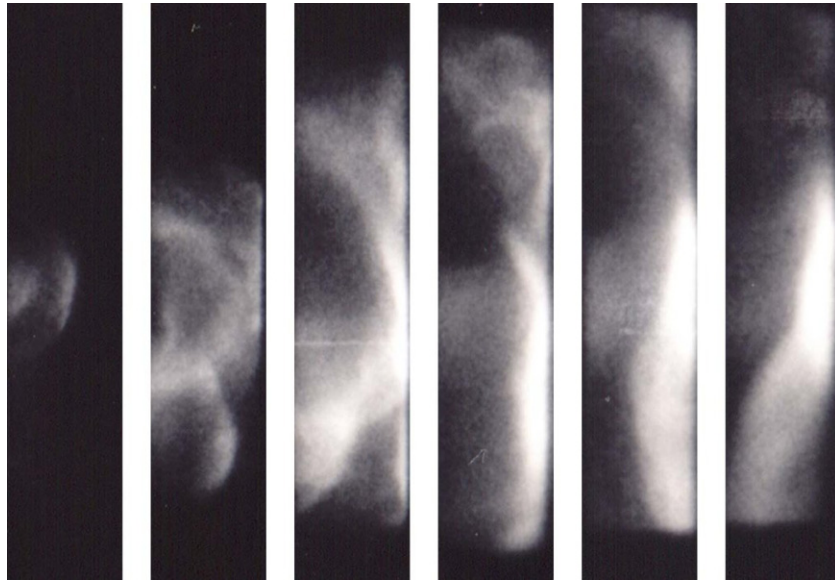
Figure 3.12: Photographs of the plasma discharge (argon, 9 kV, 100 mTorr) leaving the accelerator (left of each frame) and striking the momentum plate (right of each frame). The frames are 0.5μs apart.
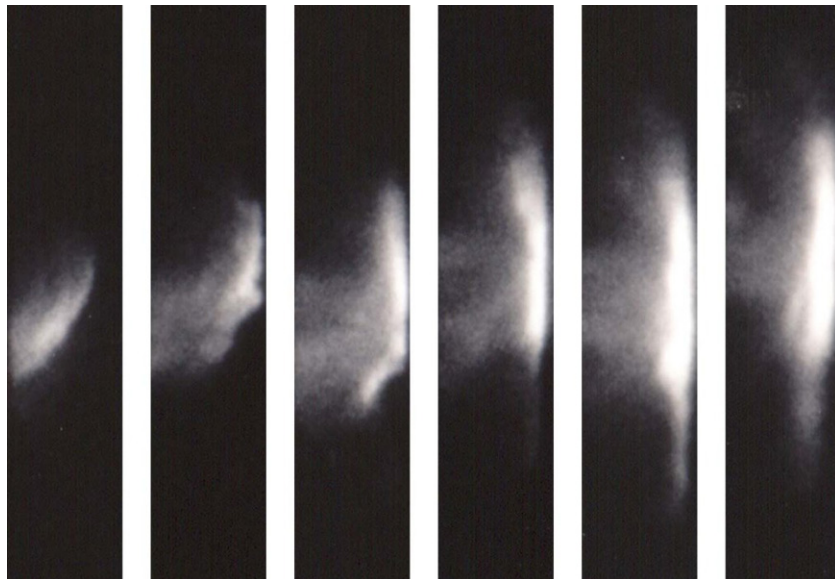

Figure 3.13: Same as figure 3.12, but for 300 mTorr.

The fifth assumption listed above is that the fraction of plasma that backscatters off of the plate is known. The extreme case, a perfectly elastic collision in which the plasma particles bounce back with the same velocity as they initially had would lead to a measured momentum that is twice the true momentum. Chavers has used the following analysis to calculate the fraction of the intercepted momentum that is reflected [48, 49]. A particle reflection coefficient, R_N, is defined as the fraction of incident particles that are reflected. Similarly, an energy reflection coefficient is defined,

$$R_E = \frac{E_{ref}}{E_{in}} R_N, \qquad (3.10)$$

where E_{in} is the incident energy and E_{ref} is the reflected energy. It can be seen, then that the fraction of the incident momentum that is reflected is,

$$F_{ref} = \sqrt{R_N R_E}. \qquad (3.11)$$

The particle and energy reflection coefficients are obtained from reference [50], and are functions of the incident energy of the particles and the atomic masses of the incident particles and the target material. In section 5.2.1 we estimate the reflected momentum for our experimental conditions and use this to adjust the measured impulse to more accurately represent the true impulse. The corrections will be in the range of $20 - 30\%$.

We have justified each of the assumptions required for the interpretation of the momentum plate measurements, some more rigorously than others. Even so, the momentum plate remains the most inexact diagnostic employed in this study. We will keep this in mind in our interpretation of the results.

Chapter 4

A Detailed Case Study

In this chapter we describe the experimental results of a detailed study of the plasma parameters and current sheet evolution in an argon discharge at 100 mTorr initial pressure and 9 kV charging voltage. In chapter 5 many of the experiments presented here will be repeated for various pressures and propellants but without the same level of detail. This condition is a typical example of the discharges in our experiments. The diagnostics employed are high-speed photography, magnetic field probing, and interferometry. These are used to determine the magnetic field, current density, electron number density of the discharge. Also the velocities of the sheet and wake and the mass of the current sheet can be determined. These measurements help us to understand the evolution of the discharge into a steady-state propagation phase. It is this phase of the discharge that we will study in chapter 5 and model in chapter 6 to understand the effects of current sheet mass leakage on the performance of the accelerator. Throughout this chapter we will present various experiments and results, but will delay the discussion of the trends until section 4.8.

4.1 Photography

The Imacon camera, described in section 3.2, was used to take photographs of the discharge in the argon, 100 mTorr, 9 kV condition. The argon ion line 3p^{4}4s - 3p^4(^{3}P)4p was captured at 487.99 nm wavelength with a Ealing-TFP 488 nm wavelength, 10 nm bandwidth interference filter [51]. The photographs from this test are shown in figure 4.1.

These photographs are of a 13.5 cm by 5.08 cm area of the accelerator, with the anode on the top and the cathode on the bottom. The left edge of each frame is 7 cm from the breech of the accelerator. The current sheet is moving from left to right.

The timing of the frames is from top to bottom. The first frame is at 1μs into the discharge, and each subsequent frame is 1μs later. The sequence was made with two separate firings. In the first firing the Imacon camera captured frames 2μs apart. In the second firing the camera was delayed 1μs from the previous firing, and the frames were interlaid to create figure 4.1. This is possible because of the excellent repeatability of the discharges.

The grid that is slightly visible in the photographs is from a printed grid placed behind the accelerator. This was done to verify the location of the photographs in the accelerator.

4.2 Magnetic Field Contours

Magnetic field probes were used in the discharge under the conditions of the study (argon, 100 mTorr, 9 kV). The probes are coils on which a voltage is induced that is proportional to the time variation of the magnetic field. They were described in detail in section 3.8.

Time-resolved measurements of dB/dt were made over a grid of points covering the inter-electrode space, as shown in figure 4.2. This array of data points consisted of 6 vertical locations by 72 horizontal locations. The horizontal spacing (x direction), starting at 0.3175 cm from the breech, was constant at 0.635 cm, with an uncertainty of plus or
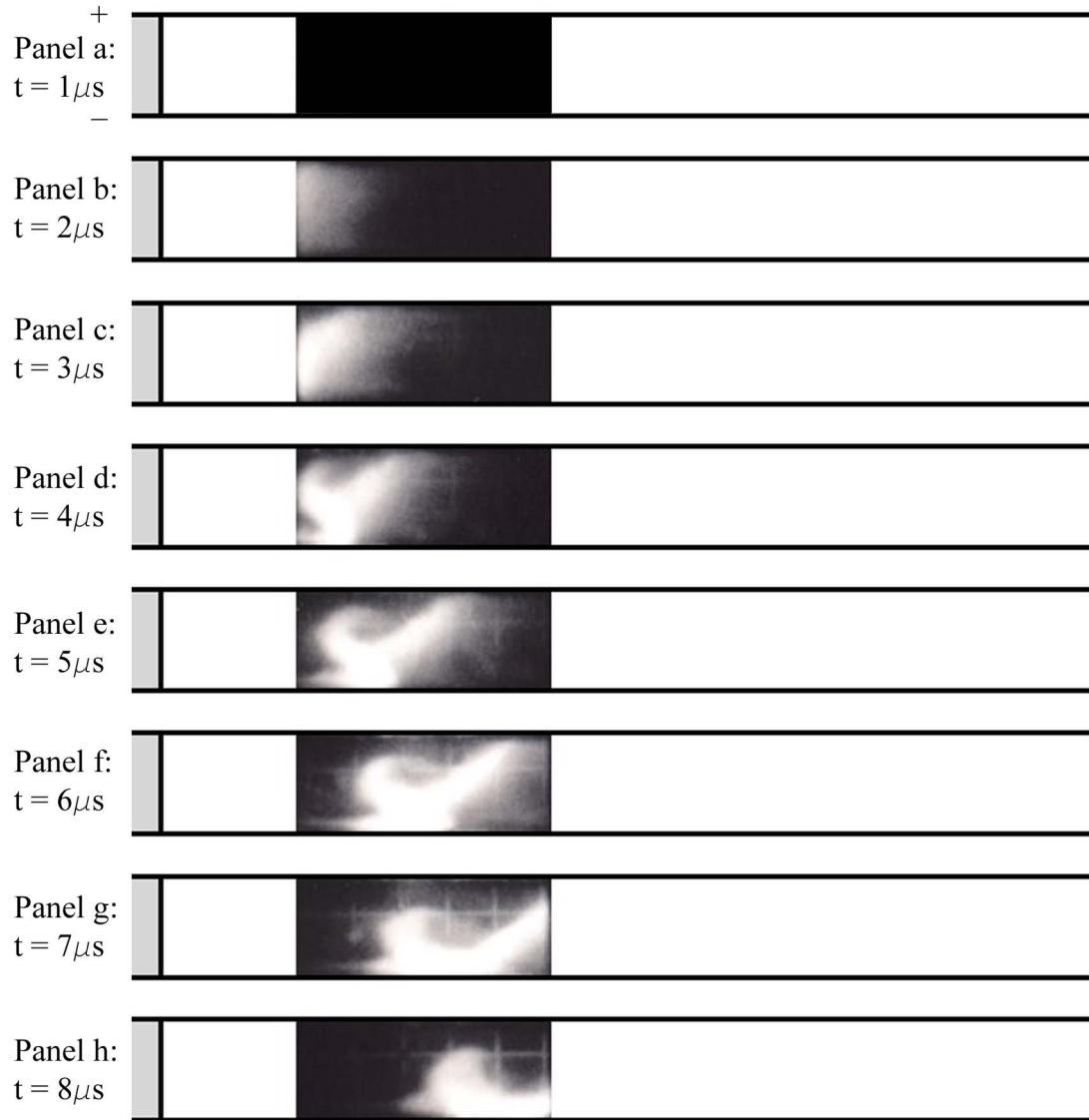
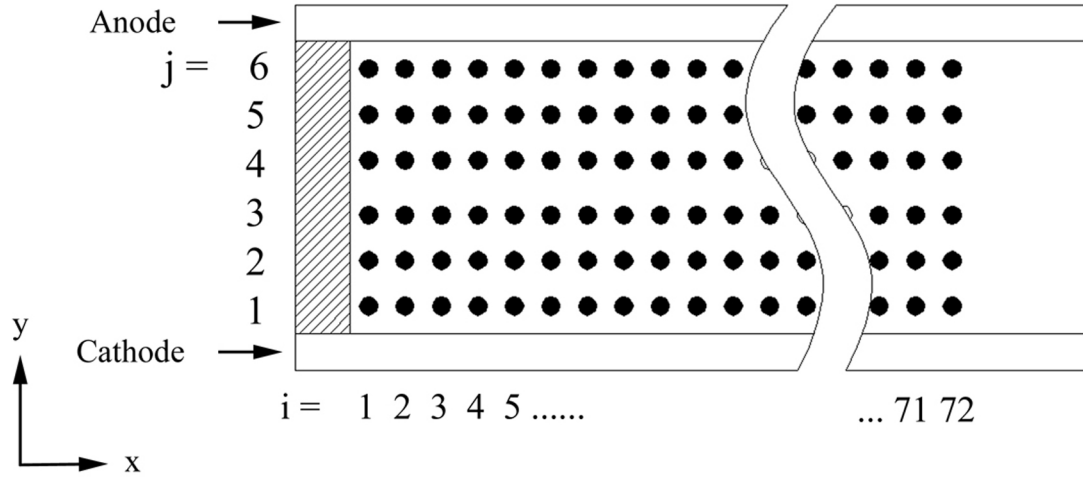Figure 4.1: Photographs of argon ion emission at $t = 1 - 8\mu s$.

Figure 4.2: The array of measurement points in the accelerator is shown. The top copper plate is the anode, the bottom plate is the cathode. An insulator backplate is shown (shaded). The coordinate system is also defined. Note that the z direction is out of the page.

minus 0.159 cm. This uncertainty is due to the ability of a translation device, used to move the probes, to accurately position the tips. Vertically (y direction), the data points were spaced at the following distances from the cathode (the bottom electrode) in the 5.08 cm gap: 0.476 cm, 1.270 cm, 2.064 cm, 3.016 cm, 3.810 cm, and 4.604 cm, with an uncertainty of plus or minus 0.318 cm, the diameter of the quartz tubes in which the coils are housed. The probed locations will be referred to as (i, j), where i and j are the x and y positions as labelled in figure 4.2. All measurements, unless otherwise specified, were taken at the centerline of the thruster in the z dimension.

It is important to note that, since only two B-dot probes were employed, only two out of the 432 locations were probed during a single discharge. The composite map of the magnetic field was then constructed from data obtained during many discharges [52]. The
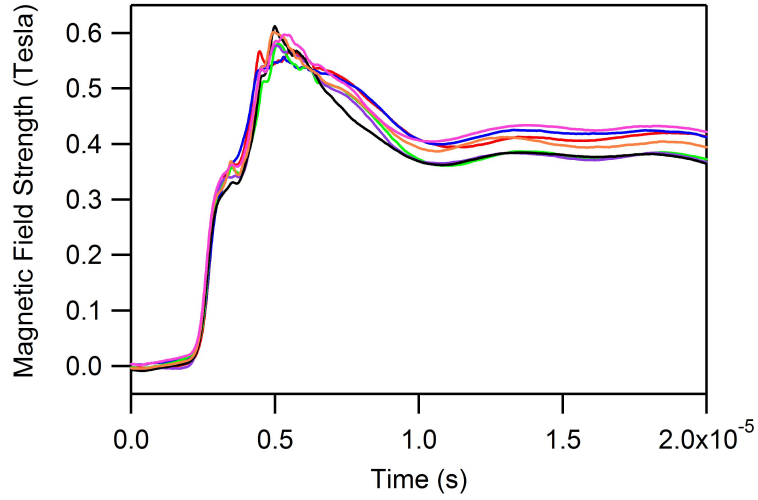
Figure 4.3: Magnetic field strength versus time for seven separate shots taken at the same physical location. The probe was located at position (12,4).

data was repeatable as is evident by eight separate tests in which measurements were made six or seven times in a row at the same location and with the same conditions. One example of these repeatability tests is shown in figure 4.3, which shows seven traces of the B field obtained from directly integrating the $\dot{B}$ traces from seven discharges repeated at the same conditions. These traces are typical examples of the data that were collected.

From these repeatability tests we were able to determine the standard deviation of the measurements. The inaccuracy of the probes is quite small (less than 1%) as verified by calibration with a Helmholtz coil [10]. Most of the error is due to the standard deviation of the repeatability. The highest standard deviation found in all of the repeatability tests was 0.05 Tesla, or approximately 10%.

With this method, at any given time in the discharge, the value of the magnetic field is known at 432 physical locations. From this knowledge, a contour plot can be constructed. This is done by displaying the magnetic field strength with a range of colors, as shown in figure 4.4. Due to the smoothing in between the grid points, any structure observed that is

56

Panel a:
t = 1μs

Panel b:
t = 2μs

Panel c:
t = 3μs

Panel d:
t = 4μs

Panel e:
t = 5μs

Panel f:
t = 6μs

Panel g:
t = 7μs

Panel h:
t = 8μs

0.0   0.1   0.2   0.3   0.4   0.5   0.6   0.7   0.8
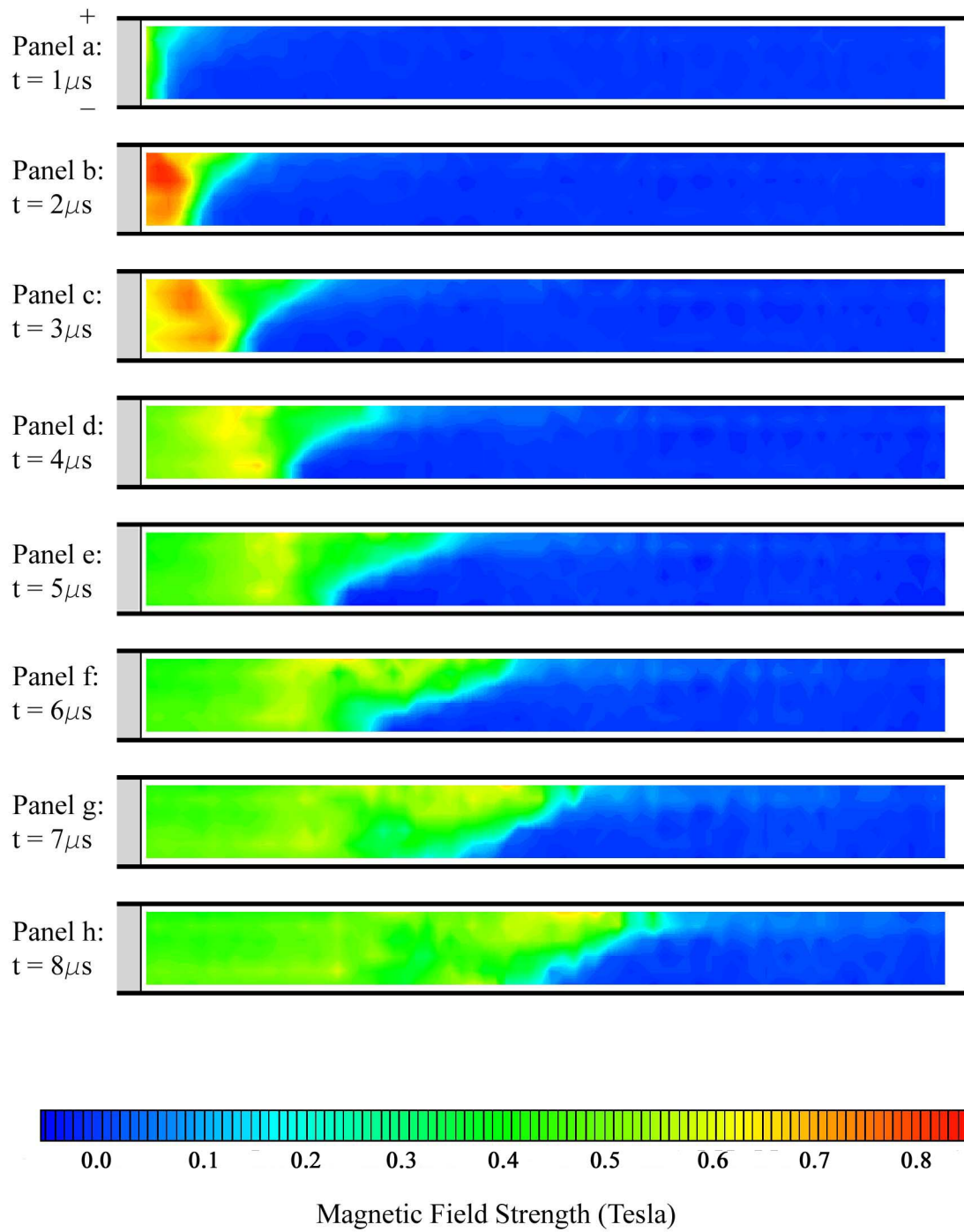
Magnetic Field Strength (Tesla)

Figure 4.4: Magnetic field contours at $t = 1 - 8\mu s$.

less than the grid spacing of figure 4.2 should not be interpreted as physical. This method provides a vivid visual display of the evolution of the magnetic field with time.

A movie [53] has been generated from seventy frames such as those shown in figure 4.4. With a spacing of $0.2\mu s$ between frames, the movie covers $14\mu s$ of the discharge.

4.3   Current Density Contours

If we consider the dimension in which the current sheet propagates to be x and the vertical dimension to be y, then the magnetic field is in the $-z$ direction. In this case, the total current density can be found from $\nabla \times \mathbf{B} = \mu_0\mathbf{j}$, which for our particular configuration yields the following expression for the current density:

$$j = \frac{1}{\mu_0}\left[\left(-\frac{dB}{dx}\right)^2 + \left(\frac{dB}{dy}\right)^2\right]^{\frac{1}{2}} \tag{4.1}$$

This expression is then evaluated over the grid to yield a temporally and spatially resolved contour plot of the current density [52]. Note that the displacement current is very small compared to the current density in the device.

There are two limitations with this technique. First, the assumption that the magnetic field is constant in the transverse (z) direction, which simplifies the evaluation of equation 4.1, was found not to be entirely correct. Measurements spanning the z dimension were made at two (x,y) locations. Figure 4.5 shows that there is a drop-off of approximately 25% in the peak magnetic field strength from the center to the side in the z dimension.

The fact that the electrodes are separated by 5.08 cm in the y direction and are 10.16 cm wide in the z direction gives an aspect ratio of 1:2. Some deviation from ideal, straight and constant magnetic fields, as seen in figure 4.5, should be expected then. This magnetic flux leakage can cause inefficiency in the $\mathbf{j} \times \mathbf{B}$ acceleration [54].
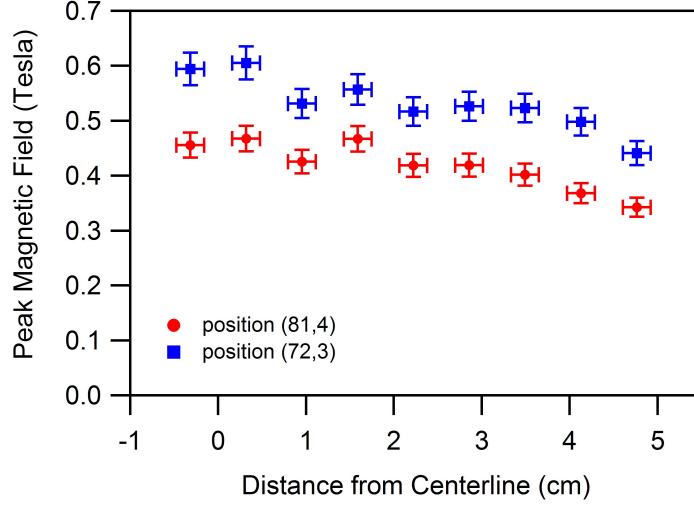
Figure 4.5: Peak magnetic field values vs. distance from the center in the z dimension for two different (x,y) positions. The error in the magnetic field measurement is taken as the largest standard deviation from repeatability tests, as discussed in section 4.2.

Furthermore, there is an error associated with taking the finite differences of the discrete data while evaluating equation 4.1. However, the resulting plots are still insightful because they allow a visualization of the current pattern and its evolution. Qualitatively, the current density contours are expected to be essentially correct and quantitatively, the measured current density values are in the expected range. Examples of such plots are shown in figure 4.6 at the same points in time as the magnetic field contours previously shown in figure 4.4. A movie [53] was generated from the resulting frames as was done for the case of magnetic field contours.

4.4 Electron Number Density Contours

Photographs show the existence of a plasma wake structure and current density contours show the region of current conduction, but it is not yet clear whether or not the plasma
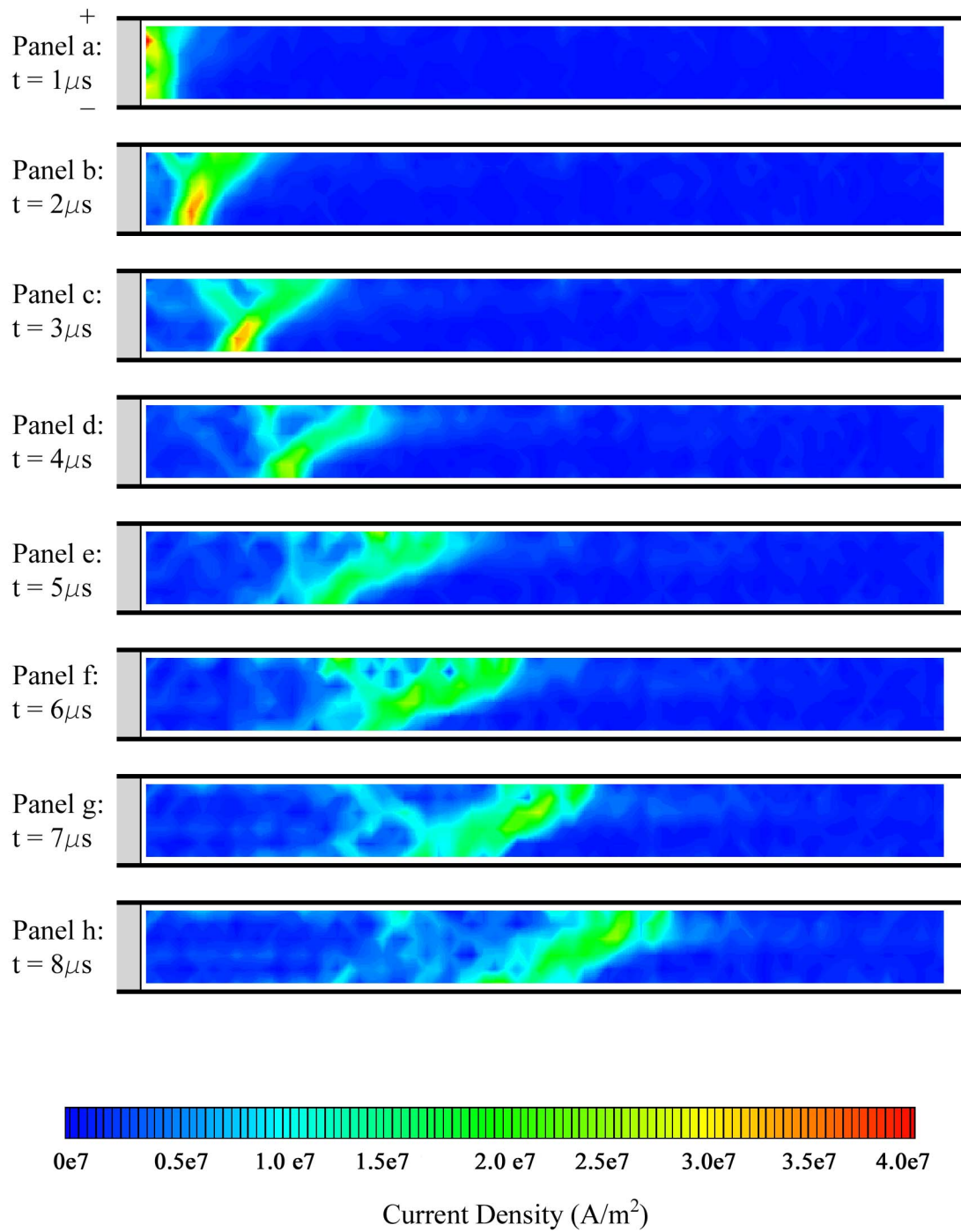
59

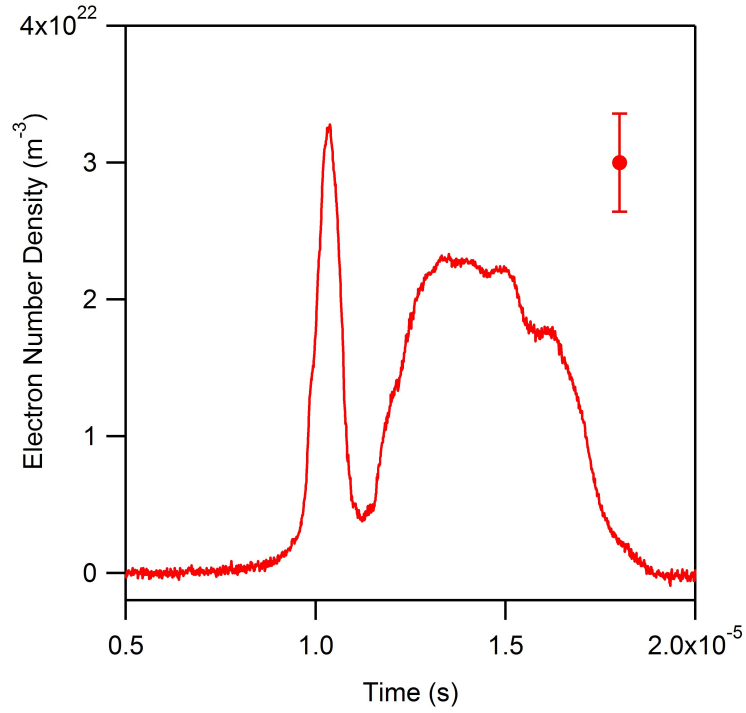Figure 4.6: Current density contours at $t = 1 - 8\mu s$.

Figure 4.7: Measurement of electron number density vs. time for argon, 100 mTorr, 9kV, from location (47,3). The first peak is the sheet and the second peak is the wake. A typical error bar derived from the repeatability of the peak density measurements is also shown.

wake is of significant density compared to the current sheet. To this end, we conducted a survey of the electron number density.

A map of the electron number density was made, in a similar manner to the magnetic field map, using an interferometer (see figures 4.8 and 4.9). This interferometer has been explained in detail in section 3.9. In short, a laser beam was used at a single location in the accelerator to obtain the electron number density vs. time at that point. A typical example of an electron number density measurement is shown in figure 4.7. By probing a grid of points, we can again arrange a two dimensional contour map of the electron number density at given times in the discharge process.

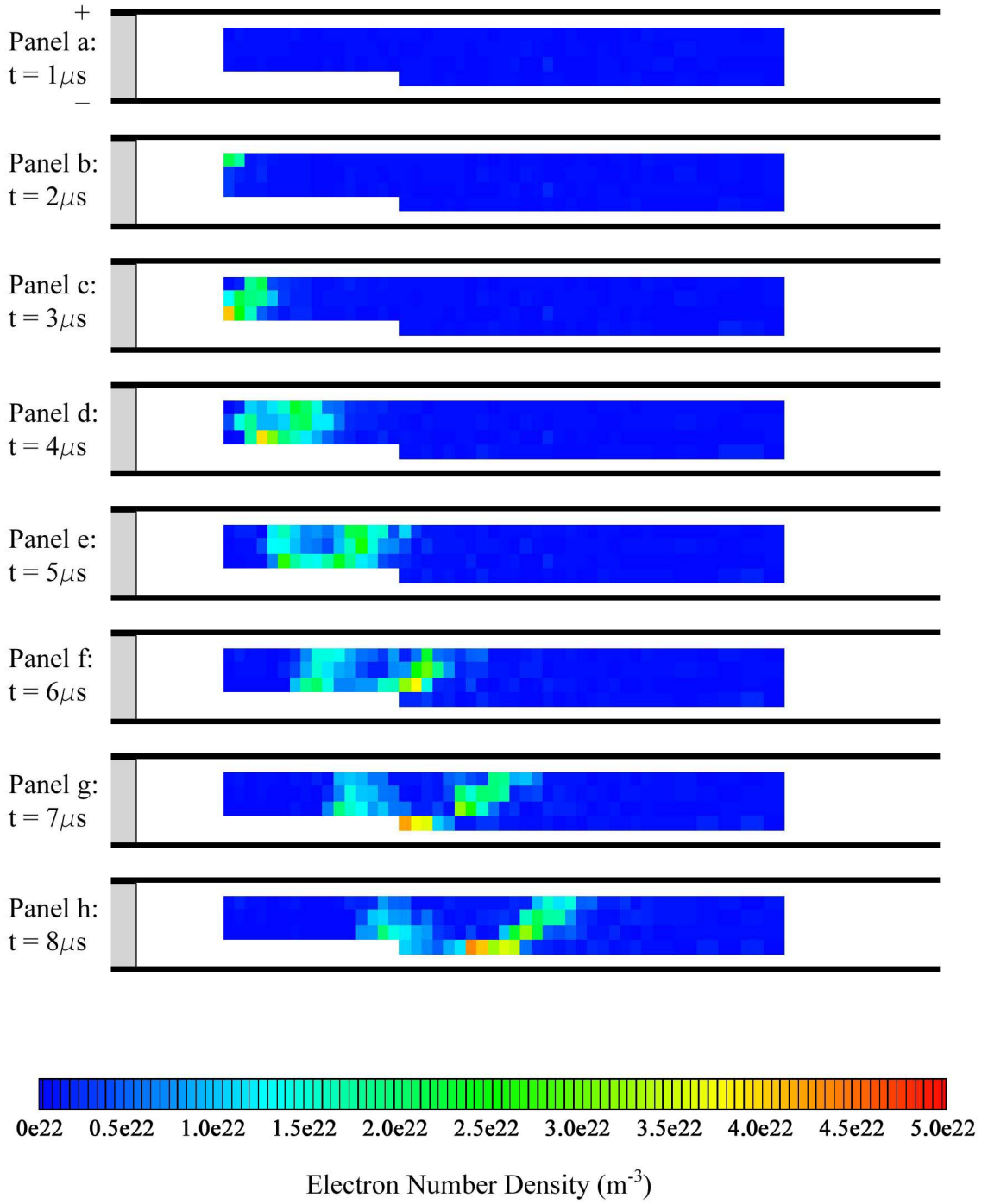There were two issues involved in this process that made it more difficult than the mag-

Panel a:
t = 1μs

Panel b:
t = 2μs

Panel c:
t = 3μs

Panel d:
t = 4μs

Panel e:
t = 5μs

Panel f:
t = 6μs

Panel g:
t = 7μs

Panel h:
t = 8μs

0e22   0.5e22   1.0e22   1.5e22   2.0e22   2.5e22   3.0e22   3.5e22   4.0e22   4.5e22   5.0e22

Electron Number Density (m^{-3})

Figure 4.8: Electron number density contours at $t = 1 - 8\mu s$.

Panel a:
t = 9μs

Panel b:
t = 10μs

Panel c:
t = 11μs

Panel d:
t = 12μs

Panel e:
t = 13μs

Panel f:
t = 14μs

Panel g:
t = 15μs

Panel h:
t = 16μs

0e22   0.5e22   1.0e22   1.5e22   2.0e22   2.5e22   3.0e22   3.5e22   4.0e22   4.5e22   5.0e22

Electron Number Density (m^{-3})
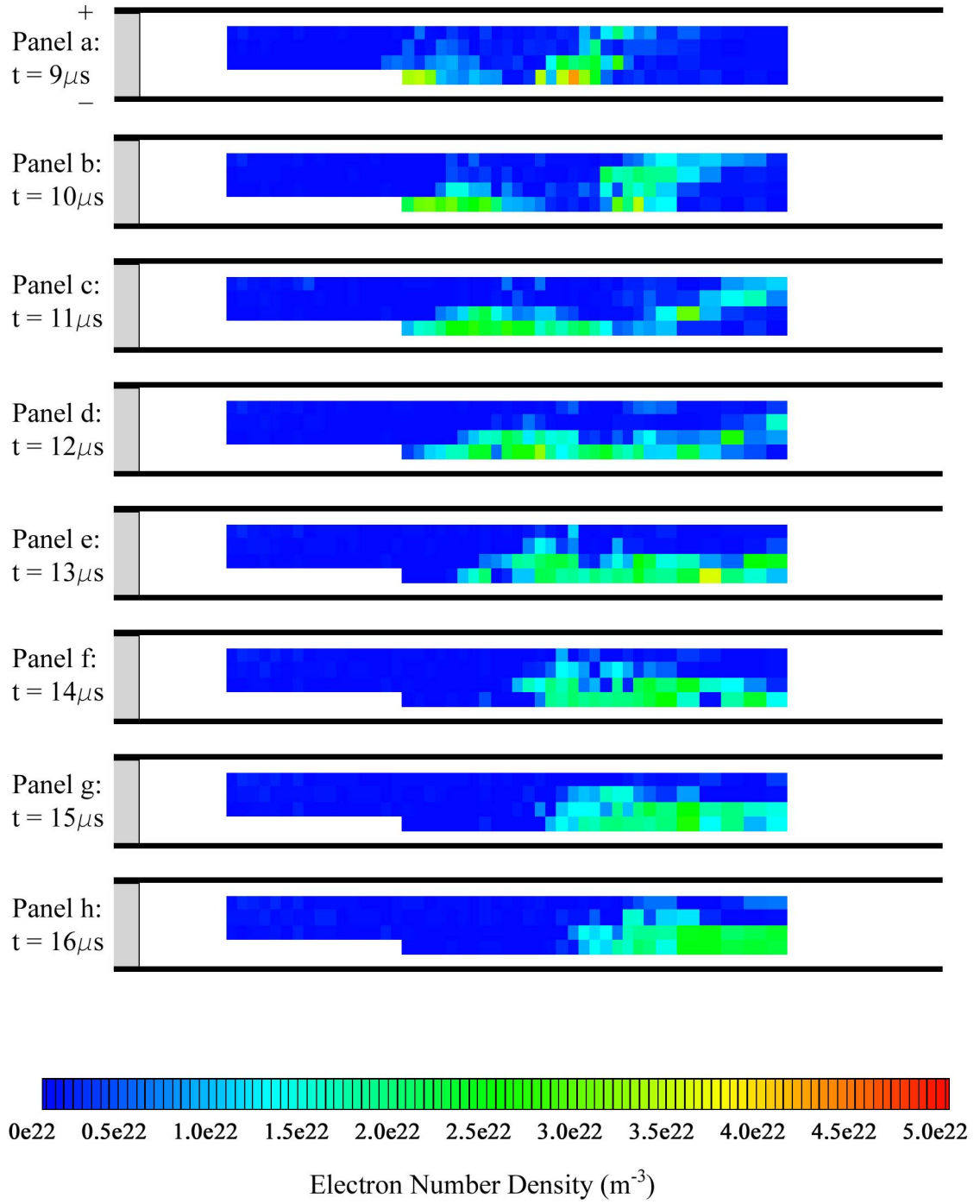
Figure 4.9: Electron number density contours at $t = 9 - 16\mu s$.

netic field mapping. First is that the electron number density measurements were far less repeatable from shot to shot than the magnetic field measurements. This is not entirely unexpected. Due to the dynamic nature of the sheet, small changes from shot to shot can cause small differences in the peak density, the arrival time, and the geometry of sheet structures. This is especially true at later times in the discharge when small differences in the sheet velocity from shot to shot can cause relatively large variation in the location of the sheet. Therefore, the appearance of the contours in figures 4.8 and 4.9 is far less smooth than the magnetic and current density contours. No attempt was made to graphically smooth the data, as was done in those cases.

The second issue with this measurement was that the interferometer was unable to capture the rise of the electron number density correctly if it was too quick. In other words, a high dn_e/dt was problematic for our interferometer. This is because the interferometer was limited in phase detection by the 40 MHz beat frequency used as part of the heterodyne system. Due to this difficulty, there were regions of the accelerator which were extremely difficult to probe. These include the entire gap near the breech, and an area along the cathode. Therefore the grid of measurement points was limited. This is evident in the contours displayed in figures 4.8 and 4.9.

4.5   Velocity of the Sheet

The velocity of the current sheet can be obtained from these contour plots as well. If we take a rise in the magnetic field from 0 to 0.2 Tesla as evidence of the arrival of the sheet, we can capture the position of the sheet versus time from the magnetic field measurements. Figure 4.3, for example, shows that this sharp rise in the magnetic field is an easily distinguished feature indicating the arrival of the sheet. This data is plotted for each row of measurements made in figure 4.10. If we then take the derivative of a fit to these measurements, we obtain

Row	1	2	3	4	5	6
$v_B(10^4$ m/s)	4.0	4.5	4.1	4.0	4.4	4.2
$v_{n_e}(10^4$ m/s)	-	-	2.9	3.5	3.7	-

Table 4.1: Velocity measurements (after 20 cm) for an argon, 100 mTorr discharge, made with both magnetic field probes and interferometry. The error on these measurement is approximately $\pm 10^3$ m/s.

the velocity of the magnetic field.

We have found that the velocity obtained in this way is sensitive to the fit that is used, because the derivative is used. Therefore, we will only report the velocities obtained from linear fits of the position vs. time data, after 20 cm. Note that the slope of the lines is lower before 20 cm for the rows near the cathode in figure 4.10, indicating that the sheet is slower initially there. This is consistent with the establishment of a canted current sheet during that phase (0 - 6 μs), with the anode attachment leading the cathode attachment.

Similarly, we can use the sharp rise of electron number density to 10^{22} m^{-3} (see figure 4.7, for example) as evidence of the arrival of the current sheet at a particular location. By tracking the time of this rise versus the position of the measurement we obtain the data in figure 4.11. Fitting a straight line, for positions greater than 20 cm, gives us the velocity of the sheet in each row of measurement. Note that row 2 has not been included in this calculation. This is because the data from about 20 to 30 cm appear to have incurred a delay in the triggering due to a spectrometer being operated concurrently during these firings. The spectrometer and interferometer measurements were both triggered with the total current signal and unfortunately during these firings it was not possible to recover the timing offset.

The results of these velocity measurements are displayed in table 4.1, and will be dis-
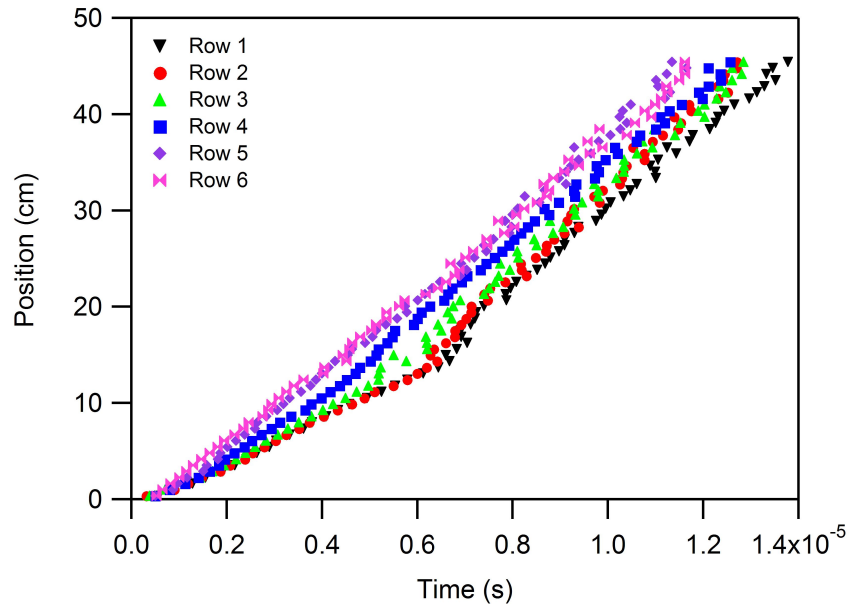
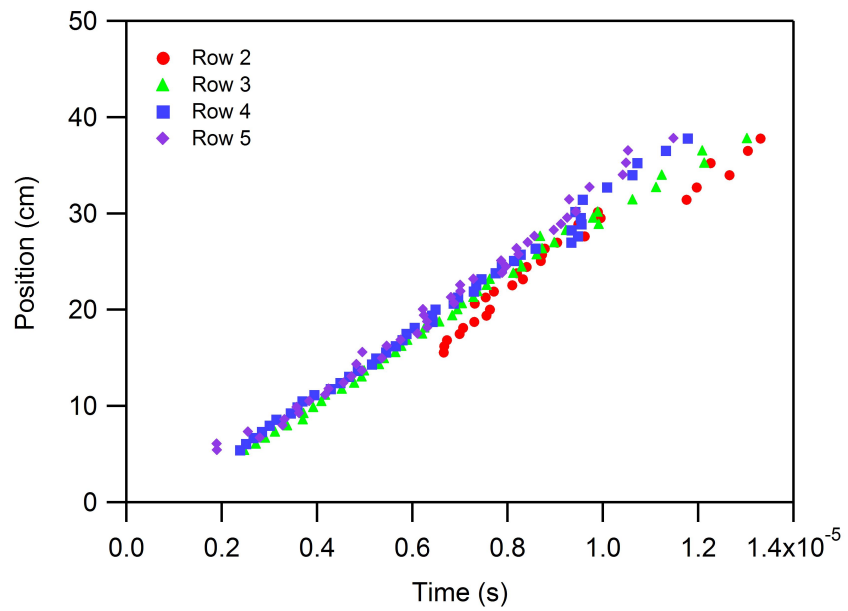Figure 4.10: Position vs. time from magnetic field probes.

Figure 4.11: Position vs. time from interferometry.

cussed further in section 4.8.2 below.

4.6   Velocity of the Wake

While the velocity of the sheet was measured using B-dot probes, that of the wake cannot be measured in this way because there is no distinguishing magnetic feature in the wake that can be followed. Instead, we will use interferometry. There are some difficulties associated with this approach. Interferometry measurements of the sheet provide a distinct location of the sheet in time because of the sharp peak. Unfortunately, the only distinct feature of the wake that can be followed in this manner is its tail-end, where the density drops off. With some assumptions a velocity estimate can be obtained from these measurements.

From photographic and interferometric evidence, the wake is seen to have a height of approximately half the electrode gap (see figure 4.9). Therefore the assumption is made that a measurement in row 2, or 1.27 cm away from the cathode will be sufficiently representative of the wake as a whole.

Another assumption that must be made is that the particles in the wake all move with the same velocity. This is implicit in the definition of a "wake velocity", but less obvious than an assumption of the sheet particles all moving with a single sheet velocity. In reality particles in the wake will probably have a distribution of velocities. Certainly, however, the wake particles cannot move with a velocity greater than the sheet, or with a velocity less than that of the tail-end of the wake. Thus this measurement will be, in the worst case, a lower bound estimate of wake velocity.

We can see from Markusic's photographs (figure 2.12), for example, that the tail end of the wake is a feature that we can track, and it moves with a velocity less than that of the sheet. In fact, an estimate from these photographs shows the wake moving at the approximate rate of 1.4 cm/μs for the entire time. This is in contrast to the sheet which increases
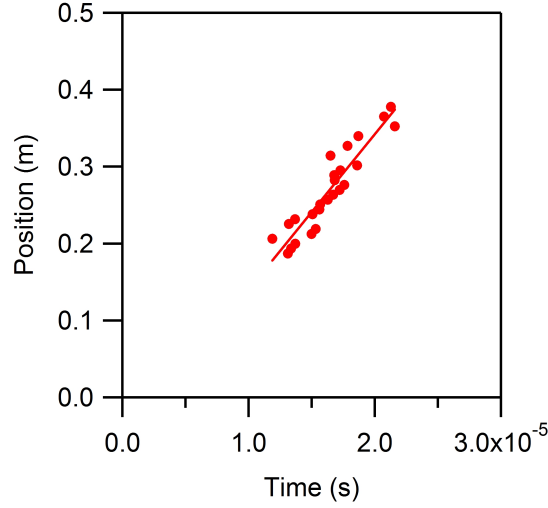
Figure 4.12: Position vs. time of the tail-end of the wake for the case of argon, 100 mTorr. The fit gives a velocity of 2.0 cm/μs.

in speed to an asymptotic value of about 4 cm/μs (as estimated from the photographs).

An analysis of the velocity of the wake from its drop-off requires us to define a drop to a certain density level as the "end" of the wake. This is similar to using a rise to 10^{22} m^3 as an indication of the "arrival" of the sheet when measuring the sheet velocity. Using a drop below 0.8×10^{22} m^3 to define the wake's end, we obtain the position vs. time graph in figure 4.12.

From the slope of the line in this graph we estimate that the wake moves with a constant velocity of $2.0 \pm .2 \times 10^4$ m/s.

4.7 Mass of the Current Sheet

The mass of the current sheet can be determined from the time-resolved electron density measurement. First, we will assume that the plasma in the sheet is singly ionized, therefore the electron number density is equal to the ion number density. Second, we can assume

that the sheet is fully ionized, so that ions make up the entire mass of the sheet. These assumptions will be addressed further in section 6.2.2. The total mass of the sheet, then, is the density integrated over the volume,

$$m_{sh} = \int \rho_i dV = \int \int \int m_i n_e dx dy dz. \tag{4.2}$$

In our experiment, the sheet is assumed uniform in the z direction (out of the page in figure 1.3) therefore the dz term immediately comes out of the integral as d, the "depth" of the electrodes. Integrating the density across the sheet width in the x direction is equivalent to integrating density times velocity with respect to time. In the y direction, the plasma density is not uniform. However, we can use the spatially resolved measurements to find the sheet mass gradient in the y direction,

$$\frac{dm_{sh}}{dy} = m_i d \int n_e v_{sh} dt. \tag{4.3}$$

Therefore, if we take the $n_e(t)$ measurement at each grid point (each (i,j) location) and integrate it according to equation 4.2 we find the mass gradient at that location. Then plotting $\frac{dm_{sh}}{dy}$ vs. y for a given x location shows the profile of mass at that location, and integrating under this curve gives the sheet mass. Care must be taken, however, to integrate only across the sheet, and not the wake. The integration must be cut off, then, at a time after the sheet has passed, and before the wake has arrived. This is not always easy, due to the close proximity of the structures, but an obvious separation point is often apparent. Figure 4.7 shows an example of an interferometric trace showing the temporal separation point between the sheet and wake densities. The error associated with the slight connection of the two structures (the density does not always go to zero between them) is small compared to the integrated mass of the entire sheet ahead of that point.

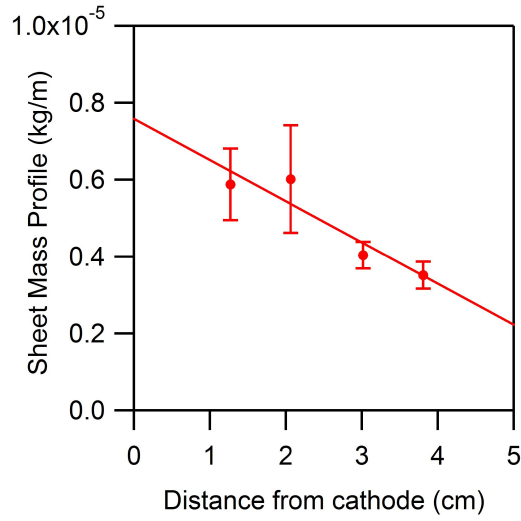Because only one measurement of electron number density was made at each grid point,

69

Figure 4.13: The sheet mass profile, calculated in each row of measurements from equation 4.3. Each point is an average over all measurements in that row after 20 cm.

the mass profile calculations have a large scatter from point to point in x. However, the density of the sheet appears to stay fairly constant in the steady-state propagation phase, and if we average the measurements from each row (after 20 cm) and use the standard deviation of the measurements to calculate error bars, we find the average sheet mass profile in figure 4.13. For simplicity, the value of v_{sh} used in these calculations was a constant 3.5 m/s for all rows. We can take the profile to be approximately linear from cathode to anode, and the current sheet mass value determined by integrating under this line is 2.5×10^{-7} kg. If we divide this mass by the total available mass we find that the sweeping efficiency, Φ_{sh}, is 37%, in this case.

4.8 Discussion

4.8.1 Evolution of the Current Sheet and Wake Structures

The magnetic field contours that have been obtained are insightful, particularly in confirming the phenomenological description of the early stages (t $< 6\mu$s) of the development of the current sheet. Several major features or trends are recognizable. The first is that the sheet, defined by the sharp gradient in magnetic field, begins as a planar sheet that is perpendicular to the electrodes, but soon begins to cant (figure 4.4a). The magnetic field near the anode moves at a faster speed and branches away from the trunk of the sheet (figure 4.4b). At the same time, a region of higher magnetic field can be seen trailing the sheet (figure 4.4b and 4.4c). While the sheet is establishing its fully developed canting angle, the trailing region of higher magnetic field begins to fade (figure 4.4d). By 5 μs the field structure has reached a fairly constant pattern (figure 4.4e). Downstream of the sheet the magnetic field strength is zero and upstream of the sheet, the field is fairly constant at approximately 0.4 Tesla. The sheet remains at a constant canting angle as it propagates from this time on.

The features identified here as a branching magnetic field, which pushes ahead, and a region of higher magnetic field, which lags behind, support the phenomenological description in reference [55] which was made on the basis of more limited magnetic, interferometric and photographic evidence. We can see even more clearly from the current density contours that these structures are the same plasma columns that were previously identified in that study as the "branch" and "trunk".

Figure 4.6 clearly shows two paths of current attaching to the anode at 2 and 3 μs. Figure 4.14 shows the 3 μs case zoomed in, with the branch and trunk structures identified. This bifurcation of the sheet was also noticed by other researchers [16, 23]. After another
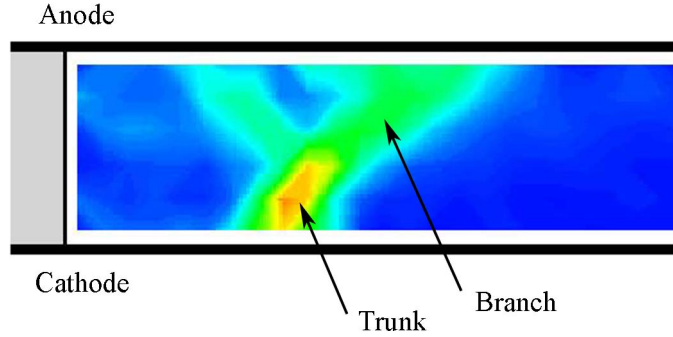
Figure 4.14: Current density contour at 3 μs, showing the branch and trunk structures.

2 μs (figure 4.6e) the trunk has ceased to carry current. At this time the branch has become the canted current sheet, and the trunk has become a body of plasma behind the sheet that does not carry current. The trunk will no longer feel a $\mathbf{j} \times \mathbf{B}$ force, and will continue at a lower speed than the sheet due to its inertia.

Other noticeable features of the current density contours are the higher current density near the cathode initially, and the lack of current conduction along the cathode. The first observation was also seen by Johansson [17]. The second observation is in contrast to Lovberg's suggestion that the plasma layer he observed carried ion current along the cathode [16].

The current density contours show two current-carrying structures, one of which (the branch) becomes the canted current sheet, and the other (the trunk) ceases to carry current, and thus disappears from these contours. We know from photographs that a plasma wake exists behind the canted sheet, and we know from the current contours that this wake does not carry current, but we do not yet know the comparative density of the wake. For this, we turn to the electron number density contours.

The electron number density contours confirm the conclusions from the current density contours, and add additional insight as well. The bifurcation of the sheet is visible in figures

72

4.8d and 4.8e. This shows that the two initial current carrying structures (branch and trunk) are also plasma structures of comparable density. As expected, though, while the remnant of the trunk ceases to carry current after a few microseconds, the trailing plasma structure remains. By 7 or 8 μs (figures 4.8g and 4.8h), the remnant of the trunk has become the wake that was previously seen in photographs. We see for the first time that this wake is of comparable density to the sheet. Also, as was also shown by photographs, the wake moves more slowly than the sheet and continues to grow longer, implying that it is being fed by mass leakage from the sheet (figure 4.9).

The development of the branch and trunk structures into the canted sheet and wake structures can be seen more clearly by comparing the magnetic, current density and electron number density contours and photographs together. Figure 4.15 shows this comparison at a time of 4μs, and figure 4.16 at a time of 8μs.

At four microseconds, the branch has canted ahead almost fully (the magnetic field contour shows the sheet is canted except right near the cathode). The current is being carried in the canted branch, with just a trace of the trunk path of current remaining. The electron density and photographs show a hook-like plasma structure behind the sheet.

By eight microseconds, the magnetic field shows a fully canted structure, as does the current density contour. The current has only one path of conduction now, and there is no hint of a second current carrying structure. The electron number density contour shows the familiar situation of the fully developed canted current sheet followed by a plasma wake of significant density. The wake looks remarkably similar between the density contour and the photograph.

Together the magnetic field, current density, electron number density and photography diagnostics paint a full picture of the evolution of the branch and trunk current structures into the canted sheet and wake plasma structures.
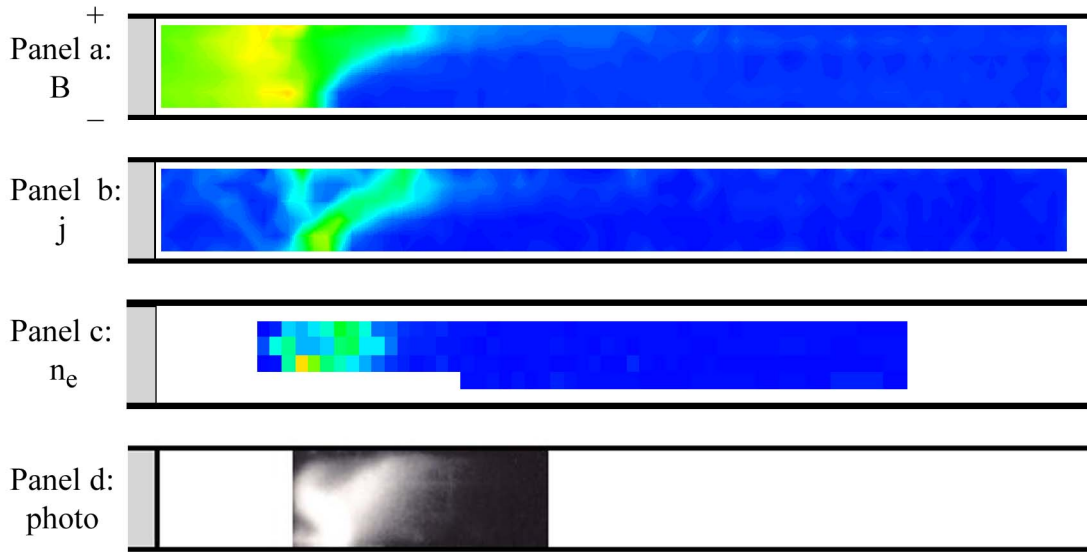
Figure 4.15: Magnetic field, current density, electron number density and argon ion emission at four microseconds.
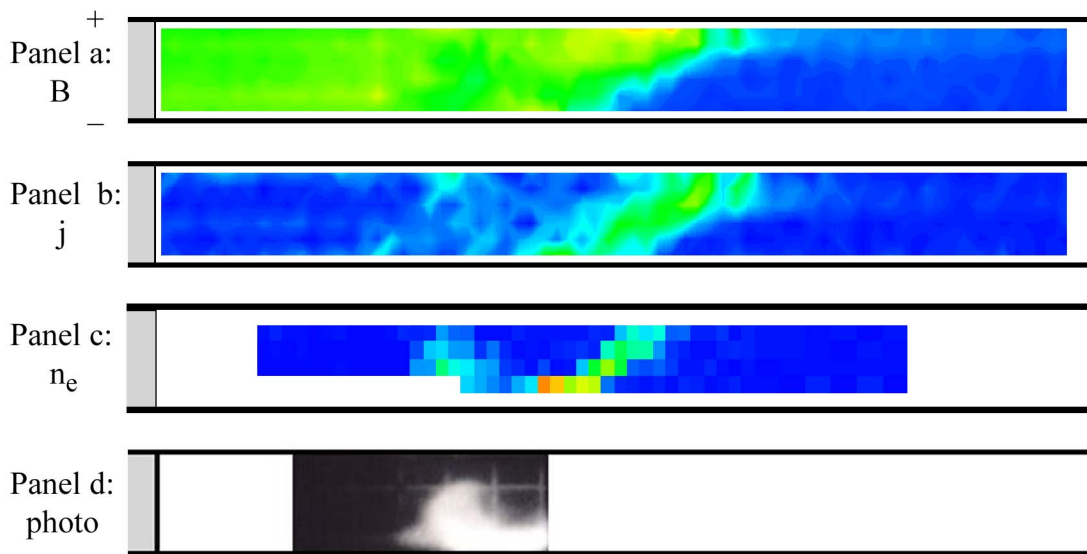

Figure 4.16: Magnetic field, current density, electron number density and argon ion emission at eight microseconds.

4.8.2 Velocity of the Current Sheet and Wake

The sheet velocity measurements made from the magnetic field probes (figure 4.10) show that near the anode the sheet travels at a fairly constant speed of about $4 - 4.5$ cm/μs. Near the cathode, the sheet starts at about 2 cm/μs and increases in velocity to 4 cm/μs until the velocity is nearly constant everywhere by about 6 μs. This is consistent with the conclusions drawn above, that the branch speeds ahead of the trunk at a higher velocity and that the canting angle is constant after an initial period. Recently, also, the velocity of the sheet in this device has been modelled with Mach 2 [56], with good results.

The sheet velocity measurements made from interferometry (figure 4.11) are subject to more uncertainty than the magnetic velocity measurements. These measurements show a fairly constant velocity, however, around $2.9 - 3.7$ cm/μs. The velocity obtained from magnetic field measurements appears to be higher than that obtained from the electron number density data. Other researchers have seen this separation of the current conduction zone from the plasma density [11, 57, 58]. Time-resolved measurements of the current density and the electron number density show that at later times in the sheet's development, the current appears to push out ahead of the electron density. Plots of these quantities are presented in appendix B. Interestingly, in less detailed velocity measurements for a range of different propellants and pressures presented in section 5.3.1, we *did not* see a discrepancy between the velocity obtained from the magnetic field data and that from the plasma ion emission data.

The wake velocity was found to be approximately constant and significantly less than the sheet velocity. We will see later, however, that under some conditions the velocity of the wake can be quite close to that of the sheet. Nonetheless, in this case there is a clear distinction between the two structures, indicating that a loss of impulse will be associated with any mass that leaks from the sheet into the wake.

4.8.3 Mass of the Current Sheet

We have shown that it is possible to use the time-resolved electron number density measurements, in conjunction with velocity measurements, to find the mass of the current sheet. Figure 4.13 shows that the density varies linearly from cathode to anode. The density at the cathode is approximately 1.5 times the midplane (average) density, and about three times the anode density. The value of the mass that is determined from this profile shows that the sheet contains only about 37% of the available propellant mass. It is clear that in the steady-state propagation phase the current sheet is not gaining mass, but either sweeping up particles and then losing them to leakage at the cathode, or allowing neutrals to permeate though the sheet entirely.

4.9 Summary

In this chapter we have explored in detail the evolution of plasma structures in our accelerator under one condition: argon propellant, 100 mTorr pressure, 9 kV voltage. We have seen that:

- The sheet begins as a planar structure, but soon bifurcates, with a branch leading off of the trunk near the anode.

- The branch soon carries all of the current and becomes the canted sheet.

- The trunk ceases to carry current and becomes the beginnings of the plasma wake.

- The plasma wake has a significant density compared to the sheet, but travels at a slower velocity.

- The current sheet continues to propagate into the ambient neutral gas with an approximately constant velocity, canting angle, and mass.

The implication is that after the initial bifurcation phase, the current sheet enters a steady-state phase of propagation during which propellant either leaks into the wake or permeates through the sheet. In the next chapter we will present measurements that show the consequences of this behavior on the performance of the device as an accelerator.

Chapter 5

Performance Measurements

While in the previous chapter we explored in detail the discharge for a single propellant and pressure, in this chapter we will explore trends in the performance of our device as a plasma accelerator. By changing the initial propellant fill pressure, and the propellant species, we can explore the parameter space of accelerator performance. We used argon, neon, helium, and hydrogen propellants in a range of pressures from 75 mTorr to 400 mTorr. Among the measurements made are: total impulse measured with the momentum plate, sheet velocity measured with photography and magnetic field probes, wake velocity measured with photography and sheet electron number density measured with the interferometer. The sheet velocity and density are used in conjunction to calculate the sheet mass. The mass of the "restrike" current sheet is calculated in the same way, and together these measurements allow us to estimate the wake mass.

With measurements of the current sheet mass, current sheet velocity and wake velocity, and an estimate of the wake mass, we can then calculate the four non-dimensional parameters introduced in chapter 1. Together these parameters determine the non-dimensional performance parameters of the device, specifically the non-dimensional impulse and efficiency. Finally, we will discuss the trends in the performance for the various propellants

and pressures tested.

5.1 Total Current Measurements

Measurements of the total current in the circuit, as a function of time, were made with a current transformer. This diagnostic is described in section 3.1. Knowledge of the total current, J, is important for the calculation of a variety of other quantities including the expected velocity of the sheet, and also will be used later to estimate the "blowing" component of impulse (this is discussed in section 5.2.1). An example of a measured current trace, taken under the conditions of argon, $9\,$kV, $100\,$mTorr, was presented in figure 3.3.

For the majority of the time the discharge is travelling the length of the electrodes, the total current is fairly constant (by design). The average current during this time varies with the conditions of the discharge. We have measured the current for four propellants while varying the fill pressure. The average current measured for a $9\,$kV discharge with varying pressure is plotted in figure 5.1. These averages are taken from $0.2 - 2.0\mu$s for each discharge. Each data point in figure 5.1 is the average of 10 measurements. The error bars are extremely small (smaller than the markers in the figure) because of the very good repeatability of these measurements. It is interesting to note at this point that the current in our device does not change more than about 10% for the different propellants or pressures.

5.2 Measured Impulse

The impulse of a pulsed plasma thruster is the momentum delivered per shot. The impulse is an important performance measurement of a pulsed plasma thruster, equivalent to the thrust of a steady state thruster. Knowledge of the impulse also leads to the knowledge of the important performance parameters, namely specific impulse and efficiency, as discussed
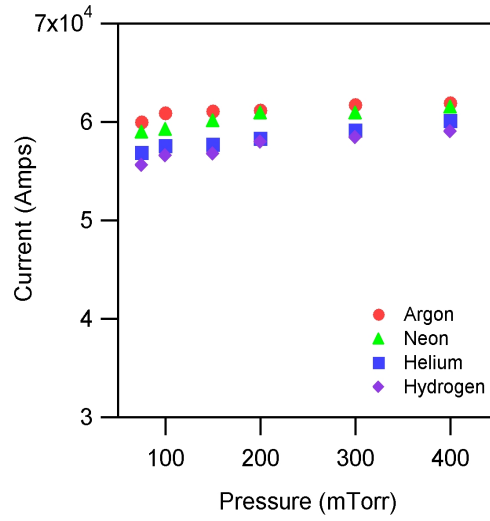
Figure 5.1: Total current vs. pressure.

in section 1.3. First we will present direct measurements of the momentum delivered during a single discharge. We will see, however, that separating the impulses of the various components such as the sheet and wake, is impossible with this method. Therefore each impulse component must be directly measured independently. The sum of all the components can then be compared back to the direct total impulse measurements to provide an independent check on the data.

5.2.1 Momentum Plate Measurements

The momentum plate diagnostic has been described earlier, in section 3.5. In short, it is a flat plate that captures the momentum of the travelling sheet, which is then measured by the response of the plate. Impulses have been measured for the parameter space of four propellants and a range of pressures.

As was mentioned earlier in section 3.11.1, some of the momentum that strikes the plate is reflected. Therefore the measured momentum must be multiplied by the factor $1/(1+F_{ref})$, where F_{ref} is the fraction of reflected momentum, to arrive at the correct mo-

mentum of the plasma hitting the plate. The fraction of reflected momentum is determined for each gas and pressure by the relation $F_{ref} = \sqrt{R_N R_E}$, and R_N and R_E are the particle and energy reflection coefficients, respectively. The particle reflection coefficient is defined as the fraction of incident particles that are reflected, and the energy reflection coefficient is the total energy of the reflected particles normalized by the total incident energy. From reference [50], using the measured velocities to determine the incident energy of the particles and using carbon as an approximation for the plexiglass target material, we find that for argon and neon the fraction of reflected momentum is effectively zero. Unfortunately data on the backscattering coefficients is scarce, especially in the $1 - 100$ eV range relevant to our experiments, however we can estimate the coefficient values for hydrogen and helium atoms using plots from references [59, 60]. These estimates are, for hydrogen: $R_N \approx 0.4$, $R_E \approx 0.2$ and for helium $R_N \approx 0.3$, $R_E \approx 0.15$. This means the fraction of reflected momentum is 28% and 21%, respectively. Thus, the data shown here has been adjusted by the appropriate factor, $1/(1 + F_{ref})$, for helium and hydrogen. This constitutes our best attempt to account for the reflected momentum. Momentum plate measurements, however, still have a high degree of uncertainty.

Figure 5.2 shows the impulse vs. pressure for discharges at 9 kV. Each data point in figure 5.2 is the average of 10 measurements. The uncertainty on these measurements is difficult to gauge, considering all of the assumptions and estimates that are necessary for the interpretation of the data. Indeed, the measurement error could be as high as 100% if our backscattering assumptions are incorrect. We have included error bars of $\pm 8\%$ in the figure that represent the largest error due to the repeatability of the measurements (standard deviation) and the error from the calibration.

Ideally, the momentum that we would like to measure with the momentum plate is the momentum of the sheet and wake added together. Unfortunately, there are two factors in
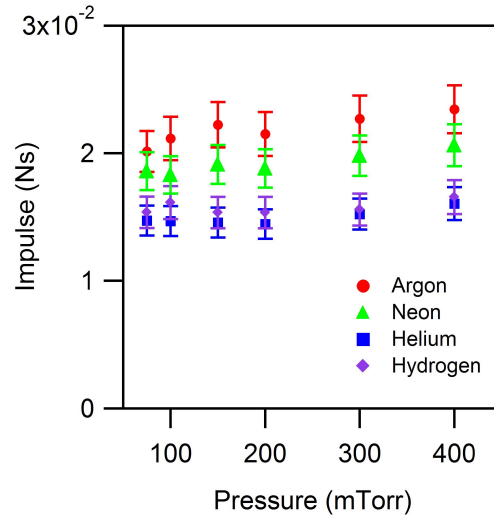
Figure 5.2: Momentum plate measured total impulse vs. pressure.

our experiment that make the situation more complicated than that. The first is that in our experiment the current reverses after about 25μs, and this launches a second, "restrike" current sheet [19]. If there is a significant amount of neutral gas remaining in the acceleration chamber at this time, this restrike sheet can be of significant density and velocity, and thus contribute to the total momentum. This is an effect that we will account for in section 5.4.2 by measuring the mass of the restrike sheet.

The second complicating factor is that the electrode length is not optimized for the current sheet velocity. In the ideal case the current reversal would occur at precisely the time when the current sheet reaches the end of the electrodes. Thus the sheet would experience a force up until it reached the end of the electrodes and then it would be released from the device. Under most of the operating conditions studied here, the current sheet reaches the end of the electrodes before the current reversal. This is especially true for the faster helium and hydrogen sheets. When the sheet reaches the end of the electrodes, but current is still flowing, it tends to balloon out of the device, and not disconnect cleanly from the electrodes [61, 62]. Because there is still current flowing in the sheet in this case, this quasi-steady

"blowing" mode can add impulse. We will estimate this blowing impulse in section 5.5 by approximating it with the impulse calculated by integrating the $\mathbf{j} \times \mathbf{B}$ force after the time that the sheet reaches the end of the electrodes.

When we have measured the sheet impulse and wake impulse and have estimated the restrike and blowing impulses, these four impulses should add up to the momentum plate measured impulses presented here.

5.3   Current Sheet Impulse

In addition to measuring the total impulse directly, measurements can be made of the impulses of the sheet and the wake by measuring the mass and velocity of the two structures:

$$I_{sh} = m_{sh}v_{sh}. \tag{5.1}$$

We have already seen that it is straightforward to measure the velocity of the current sheet through B-dot probes (section 3.11). It is also possible to measure the sheet velocity using photography. Once we have the sheet velocity a measurement of the sheet mass is possible by using interferometry, as was shown in section 4.7.

5.3.1   Sheet Velocity Measurements

The velocity of the current sheet is an important parameter for determining the performance of the accelerator. The best way to determine the velocity of the current sheet is through photography. By using multiple frames at set times, we can easily determine the distance the sheet has travelled as a function of time. An example series of photographs is shown in figure 5.3. Note that several series of photographs from separate discharges were interleaved to obtain a time resolution greater than the 2 μs resolution of the camera. This is
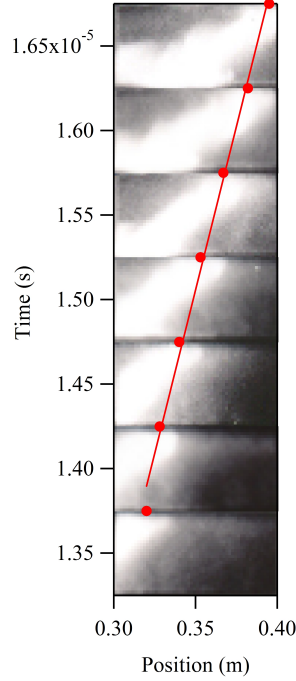
Figure 5.3: Time vs. position for a series of photographs taken in an argon discharge at 100 mTorr. The images are interleaved from four separate discharges.

possible because the discharge is very repeatable.

Another reliable way to measure the velocity of the sheet is through the time-of-flight technique, using B-dot probes. Two probes are employed, separated by a known distance, and that distance is divided by the difference in arrival time of the sheet at the two probes. The arrival of the sheet is taken as the time at which the magnetic field rises to 0.2 Tesla (see figure 5.4). In the measurements presented here, the two B-dot probes were placed at distances of 35.5 cm and 45.5 cm from the backplate to accommodate sheet velocities on the order of 10^4 m/s. This analysis assumes that the velocity is constant between the two measurement points.

By employing both of these methods, we can also check whether the velocity of the plasma light emission and of the magnetic field are the same. In section 4.5 we found some

84
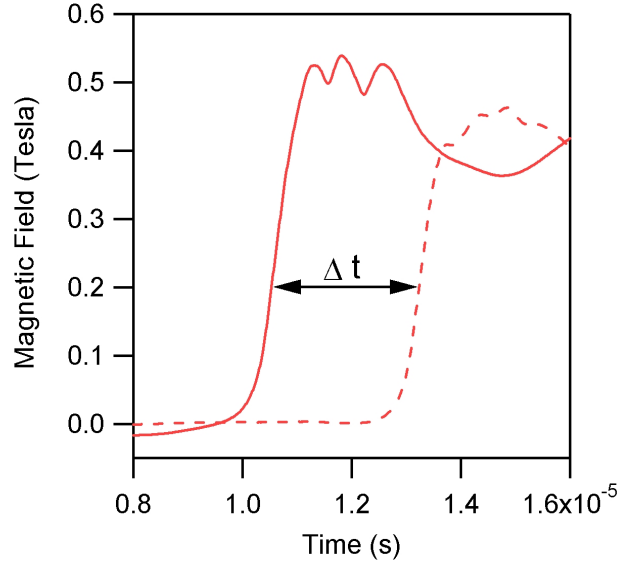
Figure 5.4: The time-of-flight technique for measuring current sheet velocity from magnetic field measurements. This plot shows two measurements made 10 cm apart in an argon discharge at 75 mTorr.

discrepancy between the two velocities, indicating a possible separation of the bulk of the plasma density from the current carrying region. Figures 5.5 and 5.6 show the current sheet velocity measured in these two ways for each propellant over a range of pressures. The error bars on the photographically measured velocity data are standard deviations of the linear fits of position versus time, taking into account also an uncertainty on the position measurement of ± 1 cm. Typically four photographic series were interleaved to obtain between four and twelve position measurements per condition (depending on the velocity of the sheet, it remained in the field of view of the camera for more or less frames). No error bars are shown for the magnetically measured velocity because only two measurements per condition were performed.

The match between the two methods is generally good, with helium having the largest discrepancy. Specifically, the maximum percentage differences between the two measure-
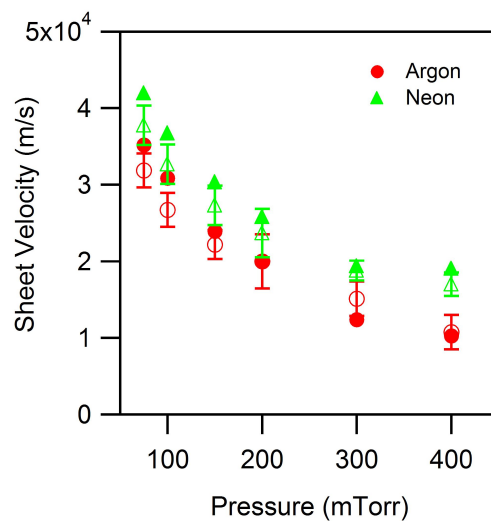
Figure 5.5: Sheet velocity vs. pressure for argon and neon. The open markers are measurements made with photography. The closed markers are measurements made with magnetic field probes.
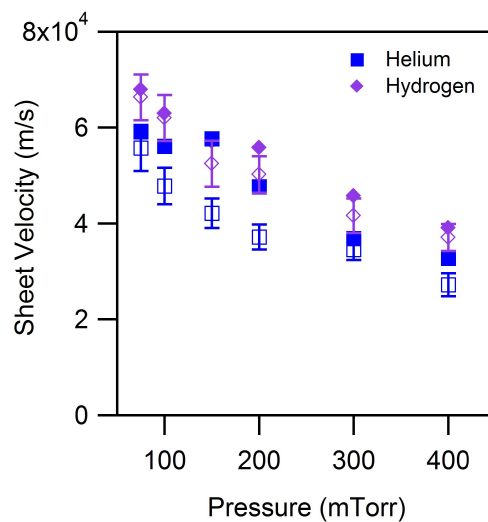
Figure 5.6: Sheet velocity vs. pressure for helium and hydrogen. The open markers are measurements made with photography. The closed markers are measurements made with magnetic field probes.

ments were 18% for argon, 12% for neon, 37% for helium and 11% for hydrogen. The plasma light emission and the magnetic field appear to travel at the same velocity, for the most part within the error bars.

5.3.2   Sheet Electron Number Density Measurements

With a few assumptions, time resolved electron density measurements of the current sheet will allow us to calculate the sheet mass and therefore the impulse. In this subsection we will present the electron number density measurements themselves. In the next subsection we use these measurements to determine the sheet mass.

We used the laser interferometer system described in section 3.9 to measure the electron number density in the sheet under different conditions. This system can measure the electron number density to within an accuracy of about $\pm 12\%$. We have seen from previous measurements (section 4.7) that the density is not constant in the sheet, it increases from anode to cathode. However, we will see in the next section that the linearity of this profile allows us to use measurements from the middle of the electrode gaps to calculate the mass of the sheet. Therefore the electron density measurements presented here are all from midway between the anode and cathode. A typical time-resolved electron density measurement is shown in figure 4.7. In figures 5.7 and 5.8 we display the peak values of electron number density in the argon, neon, helium and hydrogen current sheets.

The data presented here are from measurements at a single location in the thruster, corresponding to the laser interferometer beam positioned in the middle of the electrode gap, at 51.5 cm from the backplate, except for argon discharges. The electron number density measurements in argon were made concurrently with various other tests, and due to these other experimental constraints, the measurement location was at 38 cm instead. Since the density has been seen to remain fairly constant in the latter stages of the discharge, the
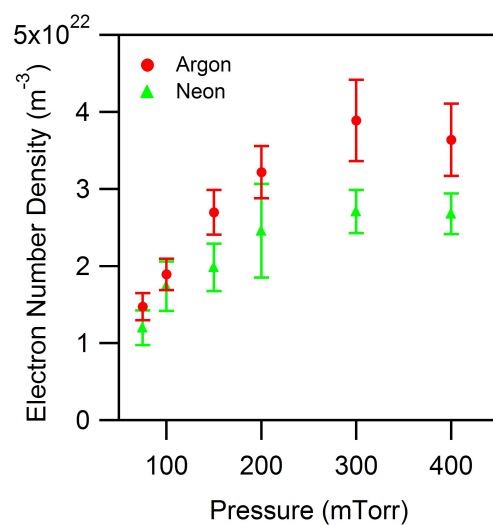
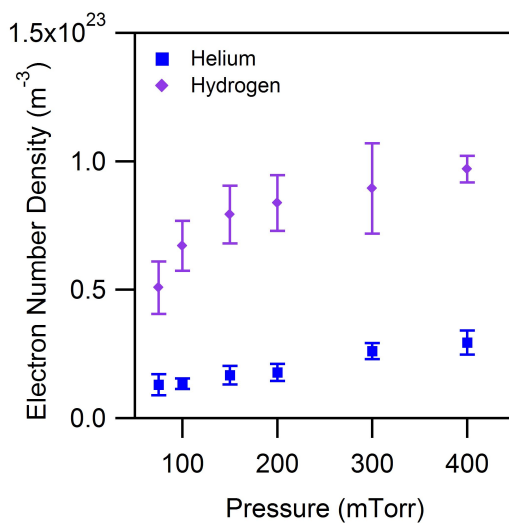Figure 5.7: Peak sheet electron number density vs. pressure for argon and neon.

Figure 5.8: Peak sheet electron number density vs. pressure for helium and hydrogen.

distinction in measurement location for argon is not expected to cause much error in the analysis.

5.3.3 Sheet Mass

We have shown in section 4.7 that the mass of the current sheet can be determined from the time-resolved electron density measurements and the velocity measurements. In that section we determined that the profile of density in the sheet is linear between the cathode and anode. Therefore, in the equation:

$$m_{sh} = \int \rho_i dV = \int \int \int m_i n_e dx dy dz, \qquad (5.2)$$

the dy term can be taken out as h if the density measurement has been made in the center of the electrode gap. In other words one could either make many measurements in the y direction to determine the mass profile and then integrate it to get the sheet mass, or assume a linear profile and make a single measurement in the middle of the electrode gap. We have chosen the second method, for simplicity. Even with small deviations from linearity in the profile, this method will give us a good estimate of the current sheet mass. Therefore the expression for the sheet mass becomes,

$$m_{sh} = m_i h d \int n_e v_{sh} dt. \qquad (5.3)$$

The sheet mass was calculated in this way, for each propellant over the usual range of pressures $(75 - 400$ mTorr), from equation 5.3, the electron number density measurements of section 5.3.2, and the photographically measured velocities from section 5.3.1. These data are shown in figures 5.9 and 5.10. Each data point in figures 5.9 and 5.10 is the result of ten measurements at that condition. The error bars on the figures are the standard deviations of the measurements.

89

The general trend of the current sheet mass, as should be expected, is of mass increasing with propellant pressure. One point in particular, the 200 mTorr measurement in hydrogen, appears to be anomalously high. The cause of this anomaly is likely to be due to some unnoticed systematic error during these measurements.

It should be noted, again, that the laser beam is not positioned at the exit of the accelerator. However, since the velocity and electron number density do not change after the canted sheet has been fully established, the mass and impulse will remain the same.

5.3.4 Sheet Impulse

It is straightforward to find the impulse of the sheet by multiplying the mass and velocity of the sheet together. The measured impulse of the sheet is shown in figures 5.11 and 5.12.

The error bars in these figures are calculated by compounding the errors on the sheet mass and sheet velocity measurements. In this case we see that the trend of the current sheet impulse is different for different propellants, especially for argon. For hydrogen, helium and neon, the impulse increases with pressure, while for argon it decreases. Also, the same anomalous mass measurement at 200 mTorr in hydrogen has been refelcted, so that particular measurement is again higher than the general trend in hydrogen.

5.4   Wake and Restrike Impulse

We wish to measure the impulse of the wake in addition to the impulse that the current sheet provides. The wake velocity can be measured photographically, similarly to the sheet velocity. However we will show that the wake mass cannot be accurately measured in a similar way to the sheet mass. Instead we will infer the wake mass from other measurements, and we will be able to check independently whether this was a reasonable method.
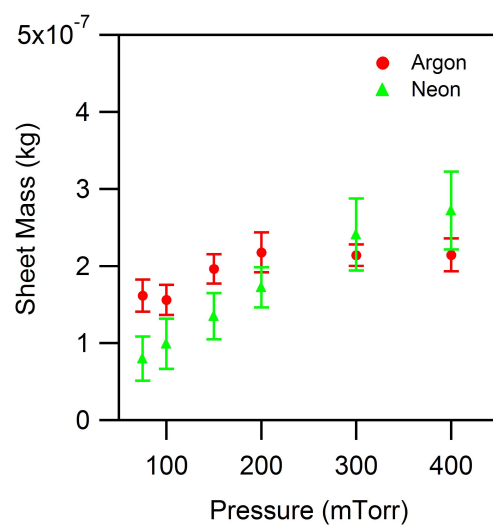
Figure 5.9: Sheet mass vs. pressure for argon and neon, all at 9 kV.
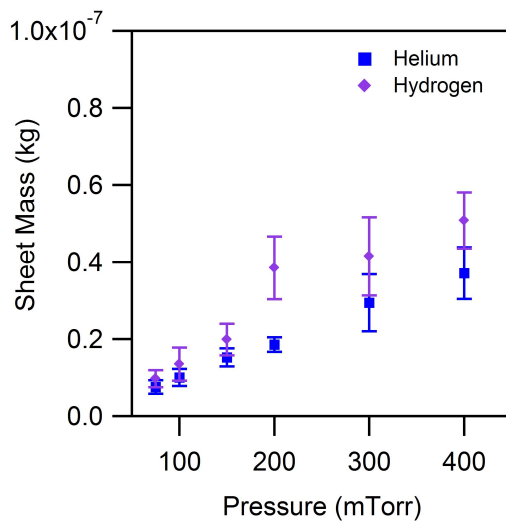

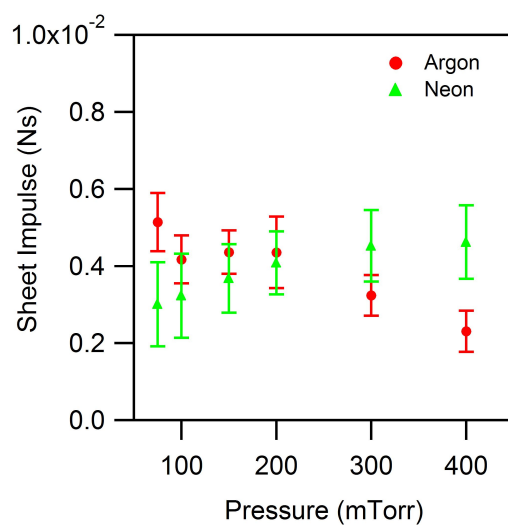Figure 5.10: Sheet mass vs. pressure for helium and hydrogen, all at 9 kV.

Figure 5.11: Sheet impulse vs. pressure for argon and neon, all at 9 kV.
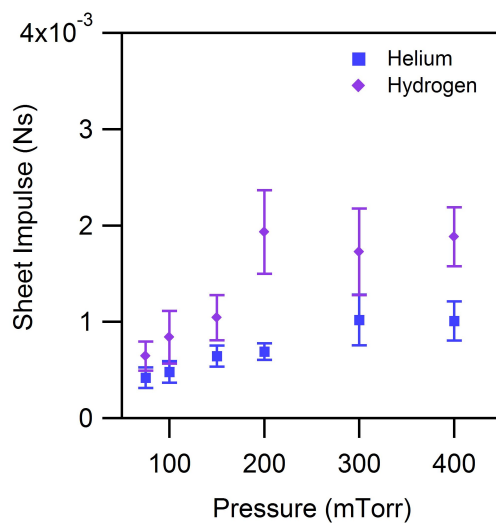

Figure 5.12: Sheet impulse vs. pressure for helium and hydrogen, all at 9 kV.

5.4.1 Wake Velocity Measurements

In section 4.6 we measured the velocity of the wake in the argon, 100 mTorr case, using interferometry to track the position of the tail-end of the wake. It was found that the wake, in that case, moved with a constant velocity, slower than the sheet. In order to determine the velocity of the wake over the range of parameter space explored here, we use the photographic method already described for measuring the sheet velocity (section 5.3.1). This method is somewhat less accurate than it was for the sheet velocity measurements because the wake is a less well defined structure than the sheet. However, it is still possible to obtain a good measurement with this method. Wake velocity measurements were obtained in this way for each propellant over the range of pressures, except for helium and hydrogen at 75 mTorr, where the wake was too dim in the photographs to make meaningful measurements. Figures 5.13-5.16 show the wake velocity, compared to the sheet velocity, for each propellant over the range of pressures. In almost all cases the wake velocity is less than the sheet velocity, but for helium at 400 mTorr and for much of the pressure range of hydrogen, the wake velocity is very close, or equal to, that of the sheet. We will use these measurements and the wake mass estimates from the next subsection together to estimate the wake impulse.

5.4.2 Wake and Restrike Current Sheet Mass

The mass of the wake is far more difficult to measure directly than that of the sheet. In calculating the current sheet mass we made assumptions that the sheet is fully ionized, has a well defined volume and that the density in the sheet increases linearly from anode to cathode, so that a density measurement at the center of the electrode gap could be used to calculate the sheet mass. From photographs we know that the wake volume is not as well defined. The distribution of the density in the wake is also not well known, and there
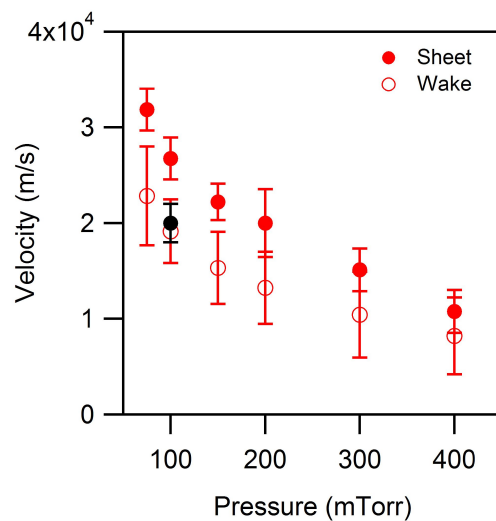
93

Figure 5.13: Sheet and wake velocity vs. pressure for argon. The single black marker is the wake velocity measurement made with interferometry measurements, that was reported in section 4.6.
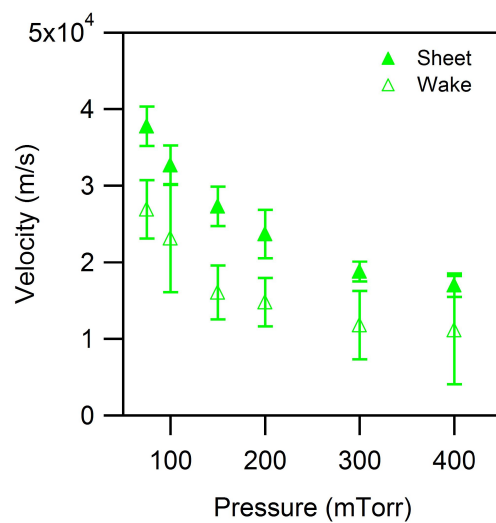

Figure 5.14: Sheet and wake velocity vs. pressure for neon.
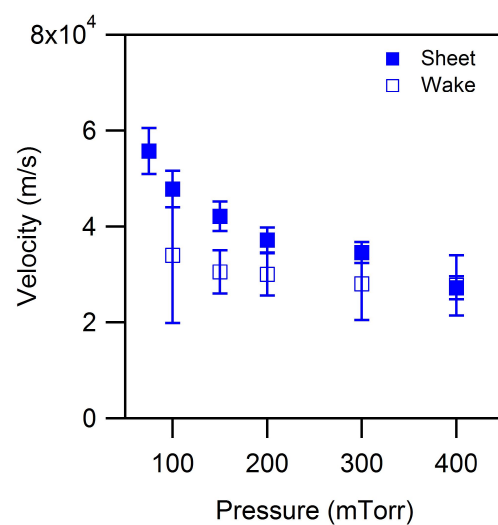
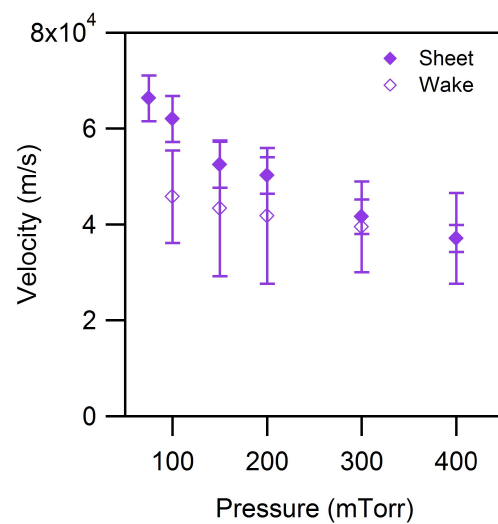Figure 5.15: Sheet and wake velocity vs. pressure for helium.

Figure 5.16: Sheet and wake velocity vs. pressure for hydrogen.

is likely to be a more sizable neutral component as well. Measuring the mass using an interferometer would likely require quite a few measurements spaced across the electrode gap for each condition.

However, there is a way to infer the wake mass, and also a way to check that this method gives a reasonable estimate. If we assume that the propellant mass available to the discharge is split into the sheet, the wake and a third component which is essentially all the mass left behind those two structures, then it is straightforward to infer the wake mass if the "left-behind" mass is measured. Fortunately this is easily accomplished in our device. As was previously mentioned, the current in this device reverses after about 25μs. When this happens a restrike current sheet is formed from the propellant mass left behind in the chamber. If we measure the mass of the restrike current sheet in the same way we measured the mass of the original current sheet, and assume that this restrike sheet contains all of the mass that has been left behind, then we can use this knowledge to estimate the wake mass. The interferometry traces of the restrike current sheet do not show a second wake behind this sheet, so the assumption that the restrike sheet contains all of the left-over mass is probably quite good. The reason that no wake appears behind the restrike sheet is probably because that it is moving into a much lower density of neutrals. Therefore, even though this sheet has a lower current and thus might be more tenuous, it is still able to sweep up almost all of the left-over gas without losing much.

After the measurement of the restrike mass has been performed, and an estimate of the wake mass obtained, we will show, in section 5.6, that we can check whether this wake mass estimate is reasonable by comparing the sum of the measured impulses of the sheet, wake (using this estimate), restrike and blowing components to the total measured impulse.

We must first make an assumption about the restrike sheet velocity in lieu of more detailed measurements. Photographic measurements of the restrike sheet velocity are quite

difficult because these sheets are dim. Magnetic field time-of-flight measurements also proved to be extremely unreliable. This is because the restrike sheet is not as well formed as the original sheet. Estimates from the arrival time of the interferometry signal show that the velocity of the restrike sheet is close to the first current sheet's velocity. This may be because while the ambient density is lower (lower drag), the current is lower as well (lower force). As a good estimate, we will use the measured current sheet velocity to calculate the restrike sheet mass in equation 5.3.

In figures 5.17-5.20 we display the restrike and wake masses for argon, neon, helium and hydrogen over the usual pressure range. For hydrogen the restrike mass was effectively zero for all pressures.

5.4.3   Wake and Restrike Impulse

Using the measured wake velocities, and the inferred wake masses, we can calculate the wake impulse. Similarly using the measured restrike mass, and again assuming the restrike current sheet moves with approximately the velocity of the first current sheet, we can estimate the restrike impulse. Together with the current sheet impulse and a blowing component, to be determined in the next section, these impulses add up to the total impulse that would be measured with a momentum plate. Measuring the total impulse and comparing it to the "added-up" impulse provides us with a way to check on our inferred wake mass. Once this verification is complete, we will have trusted measurements of the partitioning of mass between the sheet, wake and lost mass, and the division of useful impulse between the sheet and wake. The wake and restrike impulses are shown in figures 5.21 - 5.24.
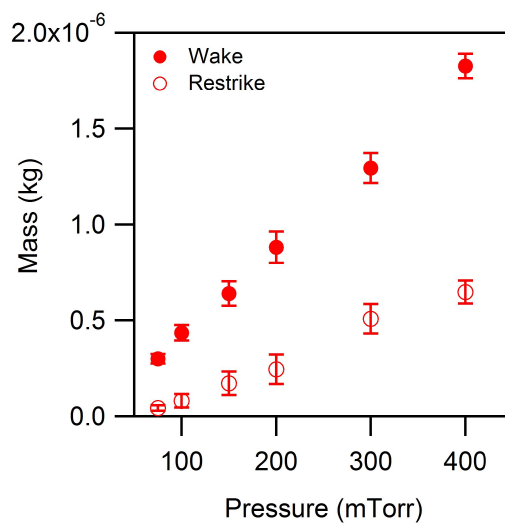
Figure 5.17: Restrike current sheet and wake mass vs. pressure for argon.
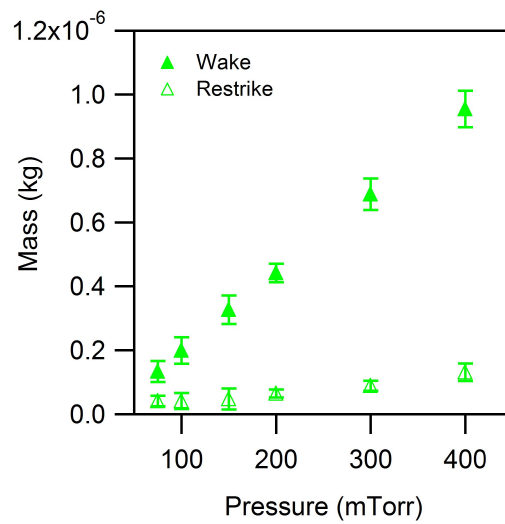

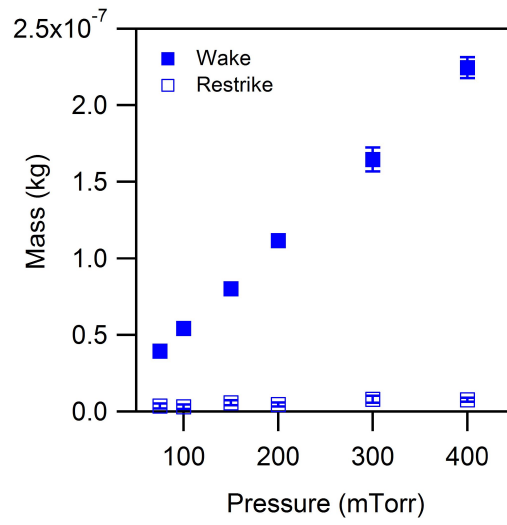Figure 5.18: Restrike current sheet and wake mass vs. pressure for neon.

Figure 5.19: Restrike current sheet and wake mass vs. pressure for helium.
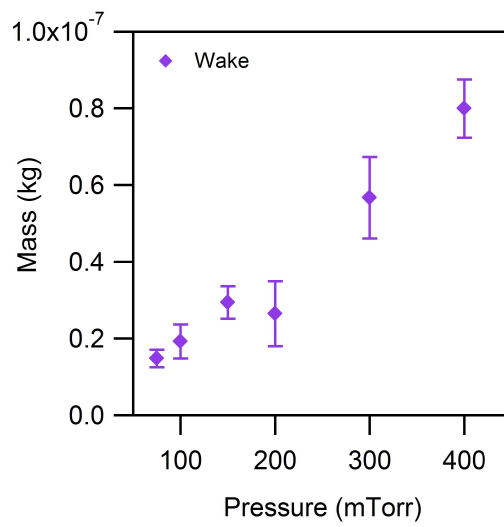

Figure 5.20: Wake mass vs. pressure for hydrogen. The restrike mass is effectively zero for hydrogen for all pressures.
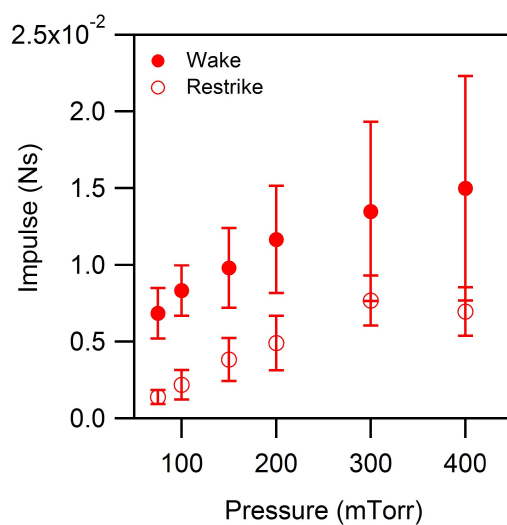
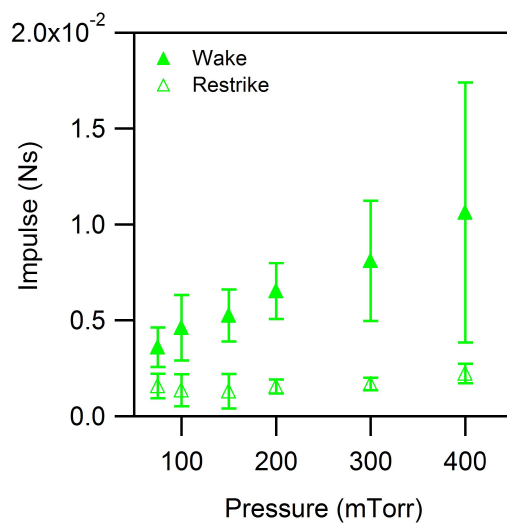Figure 5.21: Restrike current sheet and wake impulse vs. pressure for argon.

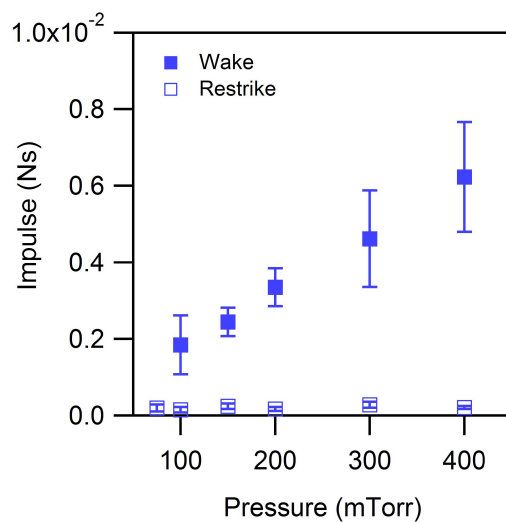Figure 5.22: Restrike current sheet and wake impulse vs. pressure for neon.

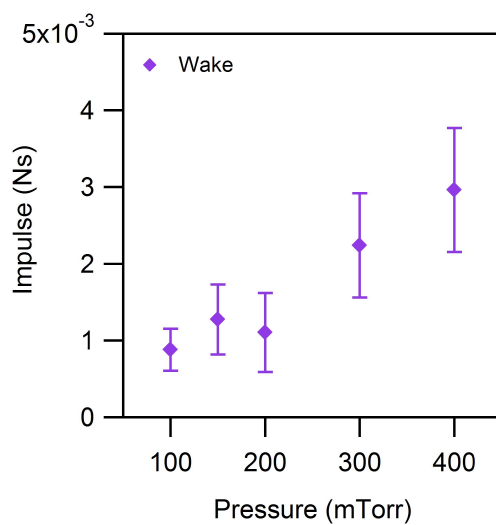Figure 5.23: Restrike current sheet and wake impulse vs. pressure for helium.

Figure 5.24: Wake impulse vs. pressure for hydrogen. The restrike impulse is effectively zero for hydrogen for all pressures.

5.5 Blowing Impulse

As was previously mentioned, in most cases in the operation of our device, the current sheets reach the end of the electrodes before the current reversal. This means that when the sheet reaches the end of the electrodes there is still a current flowing through it, so the sheet tends to stay attached to the end of the electrodes. This causes the current sheet to balloon out of the device, and the additional current can add impulse to the flow through the action of a quasi-steady $\mathbf{j} \times \mathbf{B}$ force density. If we are to compare the measured total impulse to the added-up measured components of impulse, we must take this effect into account. One way to estimate this blowing impulse is to consider the total current measurement. If the sheet experiences no losses of momentum, the ideal impulse should be given by [1]:

$$I = mv = \int F dt = \int_{t_0}^{t_f} \frac{1}{2} L' J^2 dt. \tag{5.4}$$

Performing this integration on the measured total current from the time that the sheet reaches the end of the electrodes (t_0) until the current goes to zero (t_f) will provide an estimate of the blowing component of the impulse. The time of the arrival of the sheets at the end of the electrodes has been determined from high-speed photographs. For the relatively slower sheets of argon and neon, the blowing time is relatively short, or even zero for the slowest sheets. For helium and hydrogen, however, this time is a significant portion of the total pulse time. In these cases, the blowing impulse is a large percentage of the total measured impulse.

The measurement of the blowing component of the total impulse, reported in this section, is presented graphically in the next section together with the other components.

5.6   Comparison of Impulses

In section 5.2.1 we measured the total impulse derived from the accelerator. This impulse is composed of the sheet, wake, restrike and blowing impulses. Each of these impulse components has been calculated in the previous sections. The sheet and restrike impulses were calculated from multiplying the measured masses and velocities of the current sheet and the restrike sheet. The wake mass was inferred from the measurements of the current sheet and restrike sheet masses, and this was multiplied by the measured wake velocity to obtain the wake impulse. The blowing component of the impulse was estimated from integrating the waveform of the total current during the blowing phase of the discharge. We will compare these four impulse components added together, to the momentum plate measured impulse from section 5.2.1. The main purpose of this comparison is to check whether the wake masses that were inferred, but not measured directly, in section 5.4.2 are reasonable estimates.

Figures 5.25-5.28 show the impulse comparisons for argon, neon, helium and hydrogen. In these figures, the labelled areas represent the contributions from each component of the impulse, so that one can easily see the relative importance of each impulse. In this study we are interested in the division of impulse between the sheet and wake structures, which can be seen in these figures. In a real thruster there would likely be no restrike or blowing components of the impulse, thus we are only interested in these components for the additional information they can provide. For example, it is clear that the restrike impulse is unimportant in helium and hydrogen, indicating that very little neutral mass permeates through these sheets.

The percentage difference between the two measurements of total impulse (from the momentum plate and from adding measured components) is $3 - 17\%$ for argon, $15 - 26\%$ for neon, $16 - 21\%$ for helium, and $21 - 27\%$ for hydrogen. This is a reasonable
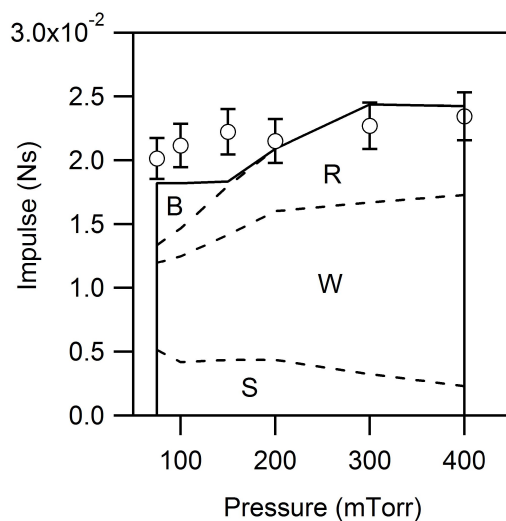
Figure 5.25: The added-up contributions of the calculated sheet, wake, restrike and blowing impulses are compared to the momentum plate measured total impulse for argon over the usual range of pressures. The impulse contributions are: sheet (S), wake (W), restrike (R), and blowing (B).
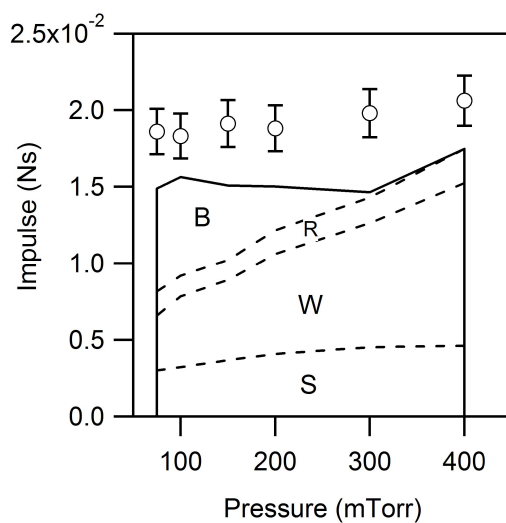

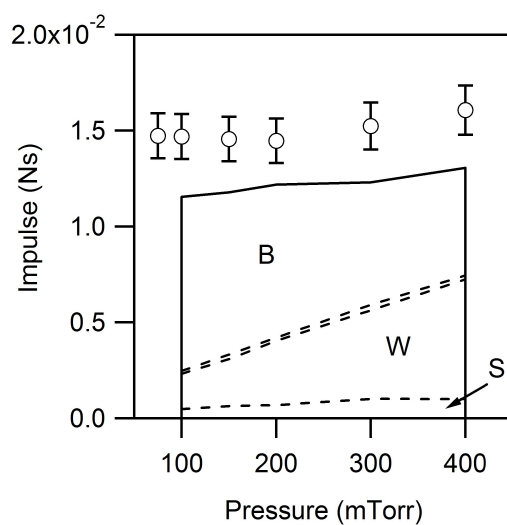Figure 5.26: The same as figure 5.25, but for neon.

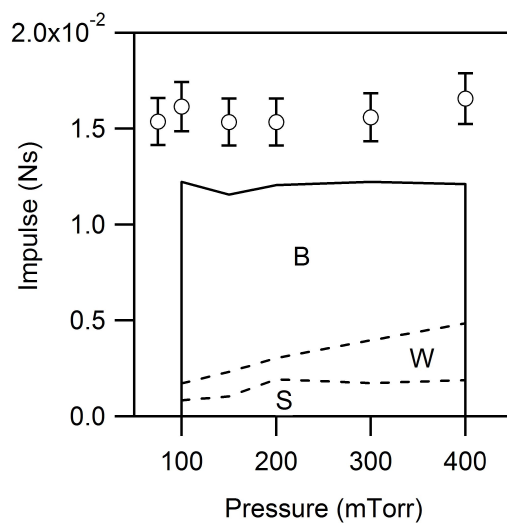Figure 5.27: The same as figure 5.25, but for helium.

Figure 5.28: The same as figure 5.25, but for hydrogen.

match, considering that the momentum plate measurements are relatively inaccurate. The comparison for the helium and hydrogen measurements is probably less accurate for two reasons. The first is that the blowing impulse, which is an estimate, makes up a large percent of the impulse for these sheets. The second reason is that momentum is reflected off of the plate for these discharges. We have accounted for this in section 5.2.1, but that also was an estimate. It is very possible that slightly more momentum was reflected which would bring the momentum plate measurements closer to the total added-up impulse measurement.

Because the two methods of measuring the total impulse, directly with a momentum plate and indirectly by adding up each component, give satisfactorily similar answers, we have added confidence that our measurements are correct. This is especially helpful with regard to the wake mass data, which was inferred from the sheet and restrike masses, but not measured directly. Essentially, measuring the total impulse directly with the momentum plate has confirmed that these inferred values are, at the least, good estimates.

5.7   Non-Dimensional Performance Parameters

Non-dimensionalizing the performance indicators of a pulsed plasma thruster allows for a more straightforward comparison of the performance of the accelerator across different operating conditions. In the introduction (section 1.3)we showed that the total impulse, specific impulse, and efficiency can be written non-dimensionally in terms of the non-dimensional mass and velocity of the current sheet and wake. Each of these quantities has been measured in this chapter for the four propellants, over the range of pressures. The sheet mass, and sheet and wake velocities were measured directly. The wake mass was inferred from other mass measurements, and confirmed by the total impulse measurements in the previous section. Each of these measurements can now be presented non-dimensionally.

5.7.1 Non-Dimensional Masses

The first parameter is the non-dimensional current sheet mass, or equivalently, the sweeping efficiency. We can obtain a measure of the sweeping efficiency from our sheet mass measurements, calculated in section 5.3.3, by dividing by the available propellant mass:

$$\Phi_{sh} = \frac{m_{sh}}{m_{av}}. \tag{5.5}$$

Figures 5.29 and 5.30 show the sweeping efficiency of discharges in various propellants vs. pressure. For the heavier propellants Φ_{sh} decreases with increasing propellant fill pressure. This is another way of expressing what is obvious from the argon and neon sheet mass measurements of section 5.3.3, namely that the sheet mass does not increase at a rate commensurate with the increase in propellant pressure. For helium, the sweeping efficiency stays constant with pressure, but it is quite low, around 20%. For hydrogen, Φ_{sh} also is constant with pressure at around 40%, with the exception of the 200 mTorr measurement. As was noted before, we believe that this single measurement is anomalously high. We do not believe that this single point is indicative of a trend.

Next we present the analogous parameter for the wake instead of the sheet. This is the percent of initially available mass that goes into the wake, $\Phi_w = m_w/m_{av}$ (figures 5.31 and 5.32). For hydrogen, with no restrike mass, and helium, with very small restrike mass, the non-dimensional wake mass is approximately given by $\Phi_w = 1 - \Phi_{sh}$. For argon and neon, $\Phi_{sh} + \Phi_w < 1$ because of the mass that is lost to both structures.

5.7.2 Non-Dimensional Velocities

The third and fourth parameters on which the performance of the device depends are the non-dimensional current sheet and wake velocities. In the introduction we defined these velocities by dividing them by the velocity that would be obtained if all of the input energy
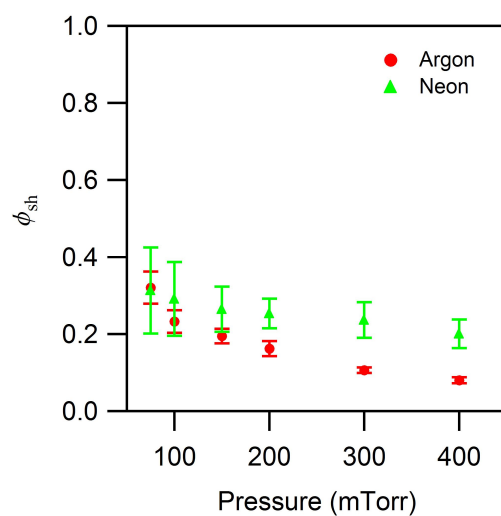
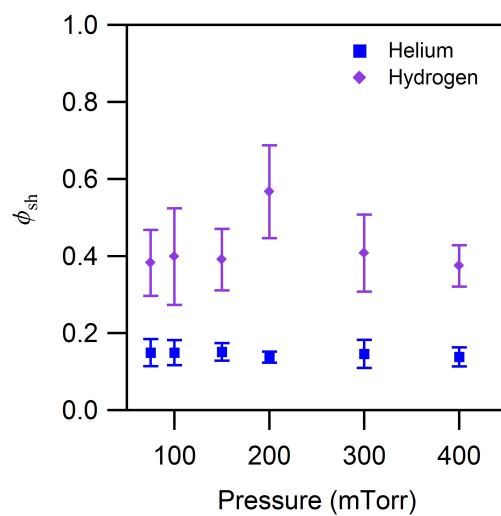Figure 5.29: Sweeping efficiency vs. pressure for argon and neon.

Figure 5.30: Sweeping efficiency vs. pressure for helium and hydrogen.
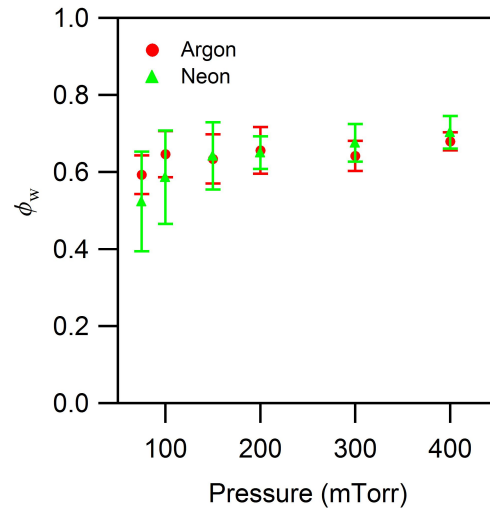
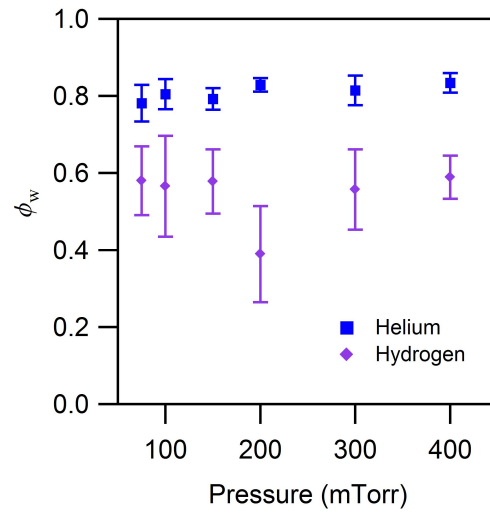Figure 5.31: Non-dimensional wake mass vs. pressure for argon and neon.

Figure 5.32: Non-dimensional wake mass vs. pressure for helium and hydrogen.

went into kinetic energy. Thus, the non-dimensional velocities are defined as,

$$\xi_{sh} = v_{sh}\sqrt{\frac{m_{av}}{2E_0}},\tag{5.6}$$

$$\xi_{w} = v_{w}\sqrt{\frac{m_{av}}{2E_0}}.\tag{5.7}$$

Using the input energy (which is 4050 J for all 9 kV discharges), the available propellant mass and the measured sheet and wake velocities, we can calculate these non-dimensional velocities. Figures 5.33 and 5.34 show ξ_{sh} vs. pressure, while figures 5.35 and 5.36 show ξ_w vs. pressure.

We can see from these figures that the non-dimensional sheet and wake velocity both are fairly constant with pressure for argon and neon, except for argon sheet velocity at the highest pressure, which begins to drop off. For helium and hydrogen, both non-dimensional velocities increase with pressure, the wake velocity at a slightly higher rate than the sheet velocity.

5.7.3 Non-Dimensional Impulse

In the introduction to this dissertation we identified three major performance indicators of pulsed plasma thrusters: total impulse, specific impulse and acceleration efficiency. We found that these three indicators depend upon the four non-dimensional parameters presented above: non-dimensional sheet mass, wake mass, sheet velocity and wake velocity. Specifically for the non-dimensional impulses,

$$\hat{I}_{total} = \hat{I}_{sp} = \Phi_{sh}\xi_{sh} + \Phi_{w}\xi_{w}.\tag{5.8}$$

Figures 5.37 and 5.38 show these measured non-dimensional impulses calculated from the four measured non-dimensional parameters. The non-dimensional impulse decreases
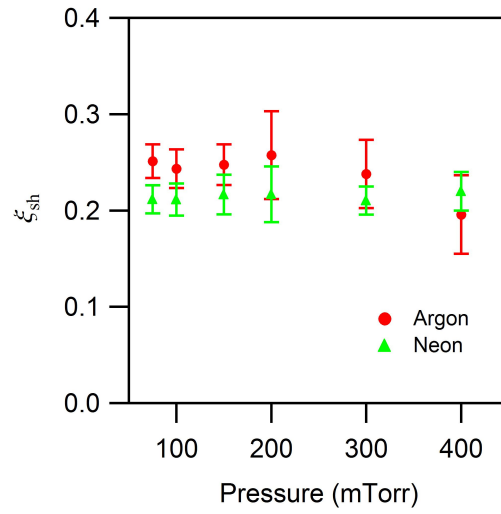
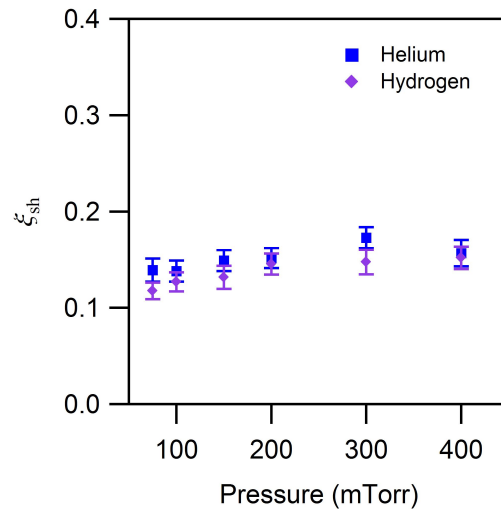Figure 5.33: Non-dimensional current sheet velocity vs. pressure for argon and neon.

Figure 5.34: Non-dimensional current sheet velocity vs. pressure for helium and hydrogen.
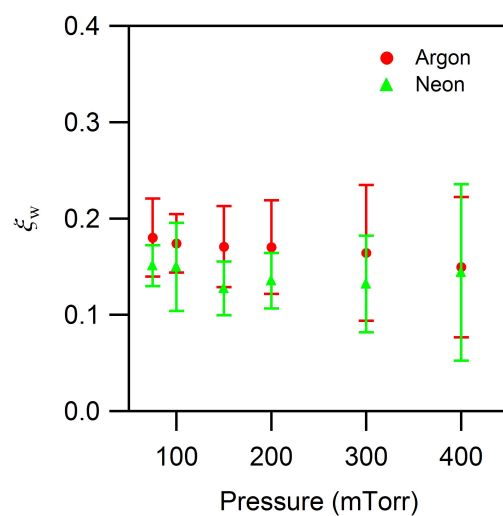
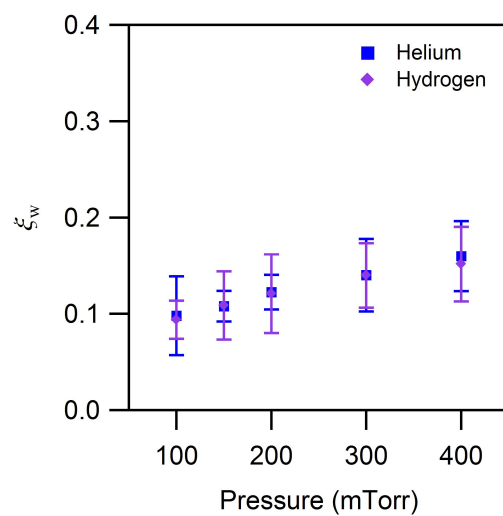Figure 5.35: Non-dimensional wake velocity vs. pressure for argon and neon.

Figure 5.36: Non-dimensional wake velocity vs. pressure for helium and hydrogen.

with increasing pressure for argon, stays constant for neon and increases for helium and hydrogen. Because we have written the non-dimensional impulse as a function of the four measured non-dimensional parameters, above, it is easy to see how the interplay of these parameters cause the trends in the performance seen here. The decreasing performance with increasing pressure for argon is clearly due to the fact that the non-dimensional sheet mass, Φ_{sh}, decreases with pressure at a rate higher than that of the increase in the non-dimensional wake mass, Φ_w. For neon, the two rates are nearly equal and opposite, ensuring that impulse lost from the sheet at higher operating pressures is made up for by increased wake impulse. Thus the non-dimensional impulse stays constant with pressure for neon. For helium and hydrogen the Φ's are both constant with pressure. The slight increase in performance with pressure, then, is due to the increase in the non-dimensional velocities. Another interesting trend is that the non-dimensional impulse is nearly equal for the helium and hydrogen current sheets. This is despite the fact that the division of mass between the sheet and wake differs for these propellants by about a factor of two (hydrogen sheets contained about 40% of the available mass compared to about 20% for helium). The reason for this is that the wake velocities are actually quite close to the sheet velocities for these propellants, so that there is not much loss of impulse by transferring mass from the sheet to the wake.

5.7.4   Efficiency

Another measure of the performance of the device is acceleration efficiency, which is the kinetic energy of the sheet and wake exhaust divided by the input energy. The efficiency is written,

$$\eta = \Phi_{sh}\xi_{sh}^2 + \Phi_w\xi_w^2. \tag{5.9}$$

Figures 5.39 and 5.40 show the efficiency versus pressure for each propellant. The trends
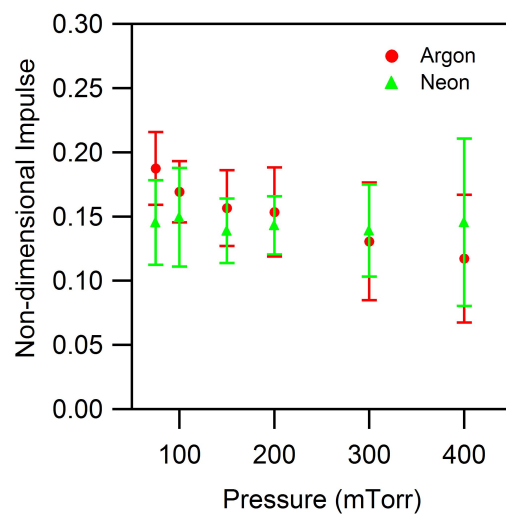
113

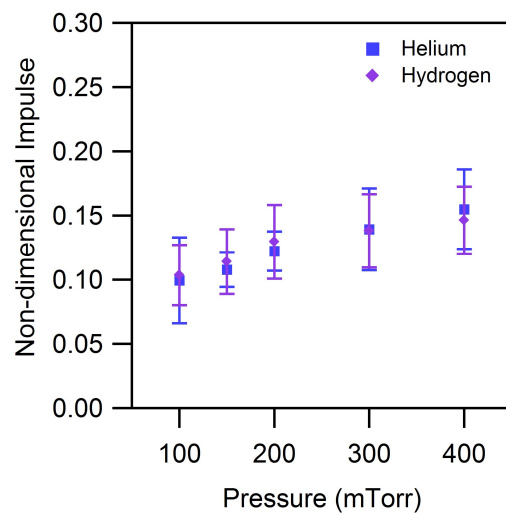Figure 5.37: Non-dimensional impulse versus pressure for argon and neon.

Figure 5.38: Non-dimensional impulse versus pressure for helium and hydrogen.

that are evident here are the same as those from the non-dimensional impulse plots above. The performance decreases with pressure for argon, is approximately constant with pressure for neon and increases for helium and hydrogen. In this case, the trends are even further exaggerated, especially for helium and hydrogen, due to the extra velocity terms in equation 5.9.

The magnitudes of the efficiencies measured here are quite low, ranging from about 1% to 4%. This is mostly a consequence of the fact that this experimental apparatus has not been optimized as a thruster. Most notably, the uniform gas fill technique should reduce the efficiency considerably versus a pulsed gas-feed system. A gas-fed PPT that has been optimized for efficient performance can achieve up to 50% efficiency [7, 63].

5.8   Summary

In this chapter we have presented measurements of the sheet and wake mass and velocity, that lead to calculations of the performance parameters non-dimensional impulse and efficiency. First the sheet velocity was measured by photography and magnetic field probing. These measurements were used, along with time-resolved electron number density measurements, to calculate the mass of the current sheet. Wake velocities were also measured photographically. Wake mass measurements could not be performed in the same manner as the current sheet mass measurements due to the complications of an undefined volume of the wake, and an unknown profile of density and ionization fraction. Instead, the wake mass was inferred from the sheet mass measurements and measurements of the restrike current sheet mass, which was assumed to contain all of the mass left behind by the two structures. The inferred wake mass measurements were validated, at least to first order, by momentum plate measurements of the total impulse which agreed reasonably with the added-up impulse of all the measured components. Each of the four parameters of sheet and wake mass
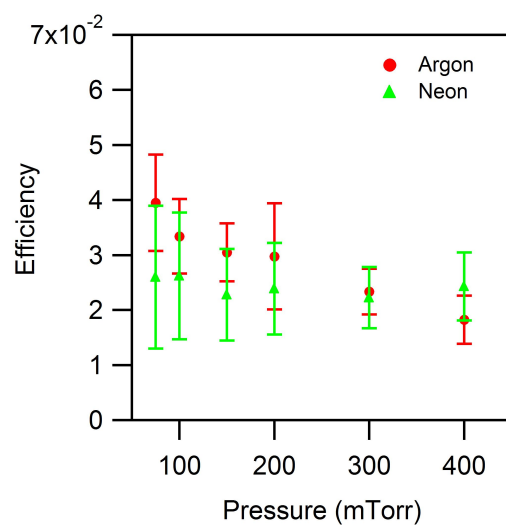
Figure 5.39: Efficiency versus pressure for argon and neon.
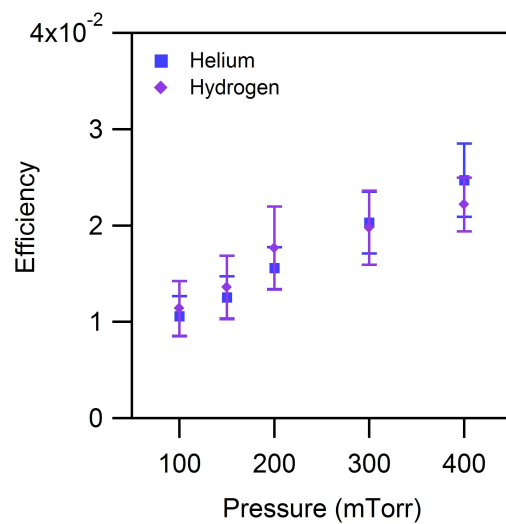

Figure 5.40: Efficiency versus pressure for helium and hydrogen.

and velocity were non-dimensionalized for easy comparison between propellants.

Two key performance parameters were calculated from the measured quantities above. These were the non-dimensional impulse and the efficiency. Through these calculations, major performance trends have been identified: thrusters operating with argon propellant have decreasing performance $(\hat{I}, \eta)$ with increasing propellant pressure, while with neon, performance is constant and with helium and hydrogen, performance increases. Because of the simple relationship of the performance parameters on the four measured non-dimensional quantities, it is straightforward to identify what causes these different trends.

- For argon, performance decreases with pressure. This is because Φ_{sh} decreases with pressure and Φ_w does not increase sufficiently to make up for the loss. In other words at high pressures there is a greater loss of mass from both structures.

- For neon, performance is constant with pressure. In this case the loss of mass from the sheet is made up for by an increase in the wake mass.

- For helium and hydrogen, the performance increases with pressure. Since both Φ_{sh} and Φ_w are constant with pressure, the performance increase comes from the increase in ξ_{sh} and especially ξ_w.

These measurements tell us what causes the performance of the device to follow the observed trends, but we want to know *why* the accelerator performs differently under different conditions. For this we will turn to a model of the current sheet in the next chapter. The goal of this model is to explain the observed behavior uncovered by the performance measurements of this chapter. Since the stated goal of this dissertation is to explain the effect of current sheet mass leakage on thruster performance, we will concentrate on explaining the leakage phenomenon and how it relates to the observations above. Specifically,

117

the major observation that is explained is why the sweeping efficiency, Φ_{sh}, stays constant

with pressure for helium and hydrogen, but decreases with pressure for argon and neon.

Chapter 6

Model of the Current Sheet

In the previous chapter we have shown that the performance of our device as a plasma accelerator varies with propellant species and pressure. It is the goal of this dissertation to determine the effect that current sheet mass leakage (the loss of mass from the sheet to the wake) has on the thruster performance. As such, we will now present a model of the current sheet that aims to explain the leakage process and, in particular, how this causes the trends observed in the sweeping efficiency, Φ_{sh}, of the sheets [64].

We have chosen to avoid the use of computer simulations in favor of an analytical approach which has the promise of giving more accessible, albeit less detailed, insight. First, we will divide the development of the sheet into two processes: canting, and propagation. The goal of modelling the canting process is to understand the way that the sheet establishes itself into a canted structure. This problem has already been treated [10, 55]. In this model, the sheet establishes itself into a fully canted structure and then maintains the same canting angle during the propagation phase. This behavior, which we have observed and described in detail in chapter 4, sets the conditions for the steady-state propagation phase.

The model presented here will deal entirely with the propagation phase of the current sheet development. We will use a force balance and a flux balance to predict the experimen-
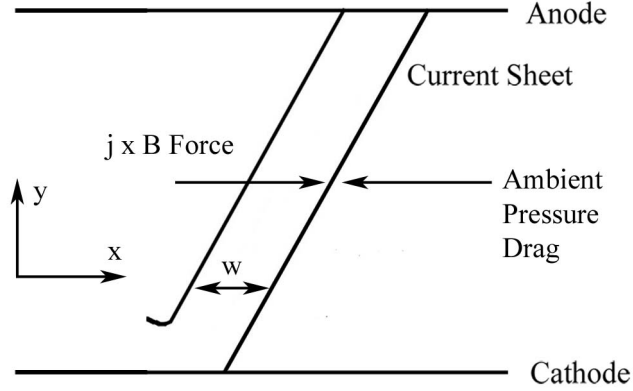
Figure 6.1: Diagram of the force balances performed to find the sheet velocity.

tally measured steady-state velocity and mass of the sheet. As a consequence, we will be able to gain insight about which processes are important in establishing the sheet mass and velocity, and identify the differences in the leakage behavior that cause the performance trends seen in the previous chapter.

6.1 Model of the Current Sheet Velocity

In the steady-state propagation phase, the current sheet velocity is determined by a balance of forces on the sheet. The equation of motion of the current sheet can be described as [1]:

$$m\frac{d^2x}{dt^2} + \frac{dm}{dt}\frac{dx}{dt} = F_x - D_x,$$ (6.1)

where $m(t)$ is the mass in the sheet and $x(t)$ is the position of the sheet, and F_x and D_x are the x components of the force and drag. Since there is no acceleration and assuming the sheet does not gain mass (see section 4.8.3), the balance is between the $\mathbf{j} \times \mathbf{B}$ force that pushes the sheet and the opposing dynamic pressure drag of the ambient neutrals (see

figure 6.1). The force can be determined by integrating $\mathbf{j} \times \mathbf{B}$ across the width of the sheet and multiplying by the projected surface area [1]:

$$F_x = hd \int_0^w jB dx = hd \frac{1}{2} \mu_0 \left(\frac{J}{dw}\right)^2 w^2 = \frac{1}{2} L' J^2.$$

(6.2)

Here we have made use of the definition of the inductance per unit length of the device, $L' = \mu_0 h/d$. Also, J is the total current, h is the inter-electrode distance, d is the width of the electrodes, w is the width of the sheet, and θ is the canting angle.

The dynamic pressure drag due to the neutrals is given by $\rho_a v^2$ times the projected surface area of the sheet. Here v is perpendicular to the sheet, so that the x component is $v_x = v \cos \theta$. The force balance is now given by,

$$\frac{1}{2} L' J^2 = \rho_a v_x^2 \frac{hd}{\cos^2 \theta}.$$

(6.3)

Solving for the snowplow velocity in the x direction, we find,

$$v_x = \sqrt{\frac{\frac{1}{2} L' J^2 \cos^2 \theta}{\rho_a hd}}.$$

(6.4)

So far this analysis has considered the sheet to be like a solid flat plate. If, however, some permeability exists such that in the frame of reference of the sheet some percentage of neutrals passes straight through, we must account for this while solving for the velocity. Any permeability will serve to reduce the drag, allowing the sheet to move at a faster velocity. If we make the simplifying approximation that a certain percentage of neutrals, X, is accelerated to the sheet velocity while the rest, $1 - X$, is not accelerated at all, then the drag becomes,

$$D_x = X \rho_a v_x^2 \frac{hd}{\cos^2 \theta},$$

(6.5)

and the velocity of the sheet in the x direction is,

121

$$v_x = \sqrt{\frac{\frac{1}{2}L'J^2\cos^2\theta}{X\rho_a h d}}. \tag{6.6}$$

The inductance per unit length of our device is based on the geometry, and thus is constant at a value of 3.845×10^{-7} H/m [54]. Likewise, the height and depth, h and d of the device were constant at 5.08 cm, and 10.16 cm, respectively. Since all of the data reported here were taken with the same applied voltage, the total current J was very similar, though not exactly the same, in all cases (typically ~ 60 kA). The current was measured with a current transformer and the flat-top value of the current, as reported in section 5.1, was used in equation 6.6. The initial gas fill density is straight-forwardly calculated from the initial propellant pressure, measured with a Baratron gauge.

The values of θ used in the calculations were obtained from the work of Markusic *et al* [10, 28] and from the present research. Measurements of θ from various methods have an error of approximately $\pm 10°$ and have shown that θ increases with increasing atomic mass of the propellant. The specific values used for θ for this and subsequent calculations are: argon: $60°$, neon: $60°$, helium: $50°$, and hydrogen: $16°$.

The force balance performed here makes the approximation that the sheet acts as a solid body and transfers momentum perfectly to a certain fraction, X, of the stationary neutral atoms. This is the only term in equation 6.6 that is unknown. By measuring the current sheet velocity and comparing to the expected velocity from equation 6.6, however, we can determine the effective amount of "permeability" of the sheet $(1 - X)$ that can explain the measurements. Since the parameter X has been inferred from measurements it does not represent a free parameter to the final model.

Hydrogen is a special case, however, because the protons comprising the sheet have half the mass of the diatomic molecules they collide with. In this case, conservation of momentum and energy of the colliding particles show that for an elastic collision the final
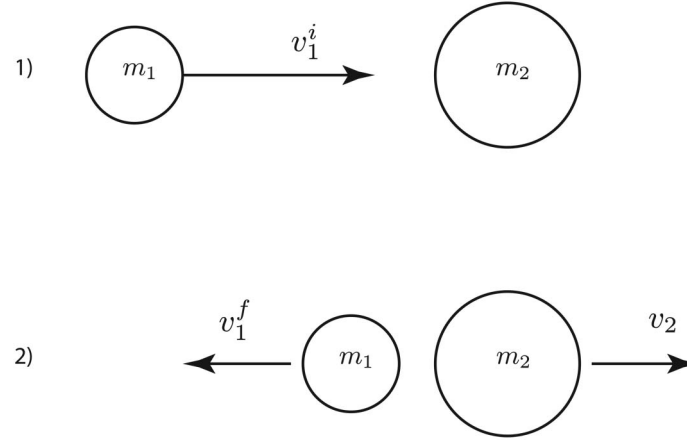
Figure 6.2: Diagram of the momentum balance of head-on collisions of sheet ions with ambient neutrals. In the case of hydrogen, $m_2 = 2m_1$ and $v_2 = \frac{1}{2}(v_1^i + v_1^f) = \frac{2}{3}v_1^i$.

velocity of the diatomic molecule is two-thirds the incident velocity of the ion and the ion will recoil at one-third of its original velocity. Therefore, while protons in the sheet can be locally accelerated to the snowplow velocity, the velocity of the sheet is equal to the mean velocity of the ions and thus should be limited to two-thirds the snowplow velocity (see figure 6.2). We find that this is the case for hydrogen. In section 6.3, the theoretical velocity for hydrogen that is used in calculations is,

$$v_H = \frac{2}{3}\sqrt{\frac{\frac{1}{2}L'J^2\cos^2\theta}{X\rho_a hd}}. \tag{6.7}$$

We have also performed a limited amount of velocity measurements of current sheets in deuterium, and they have shown the same two-thirds limitation (see appendix C).

In section 6.3 the results of the model of the current sheet velocity (equations 6.6 and 6.7) are compared to the measurements from the previous chapter.
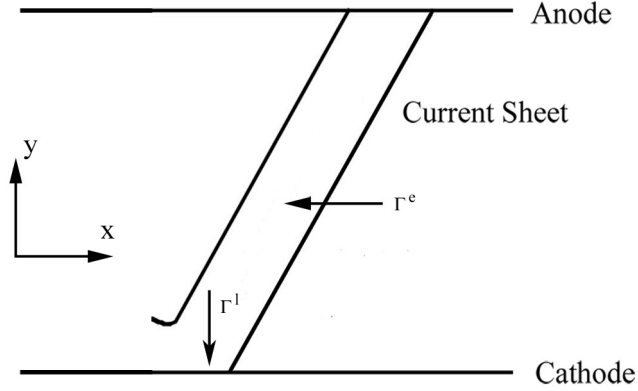
Figure 6.3: Diagram of the mass balance performed to find the theoretically expected current sheet mass.

6.2 Model of the Current Sheet Mass

We wish to explain and predict the experimentally determined sweeping efficiency trends both qualitatively and quantitatively. In order to do this, we must construct a model of the mass sweeping process. The main goal of the model is to gain insight into the important processes that cause the trends of the data that we observed.

In order to simplify the analysis, let us consider a current sheet with a single electron density and temperature everywhere across its width and height. In the steady-state phase that we observe, the sheet asymptotes to a constant velocity, canting angle and mass. In this case, the expected mass of the sheet can be determined by balancing the fluxes of mass into and out of the sheet. Figure 6.3 shows a schematic of these processes. A mass flux balance for the sheet is given by:

$$\frac{\partial m_{sh}}{\partial t} = 0 = \Gamma^e - \Gamma^l.$$ (6.8)

Here, Γ^e is the flux of mass entering the sheet, and Γ^l is the flux of mass leaking from the

sheet at the cathode and entering the wake.

Note that Γ^e is the rate of mass that is accumulated by the sheet and as such is equal to the rate of mass encountered by the sheet minus the rate of permeability of mass through the sheet. Thus this term can be expressed, using the previously defined term X, as,

$$\Gamma^e = X\rho_a v_x hd, \tag{6.9}$$

which is the percent of the neutrals that is swept up, X, times the density of the neutrals, times the sheet velocity, times the frontal area of the sheet.

If we define the velocity of plasma out of the sheet and into the wake at the cathode to be v_c, the sheet loses mass at a rate:

$$\Gamma^l = \rho_i v_c wd, \tag{6.10}$$

This means that, with $\Gamma^e = \Gamma^l$, we find:

$$\frac{\rho_i}{\rho_a} = X\frac{h}{w}\frac{v_x}{v_c}. \tag{6.11}$$

Also the sweeping efficiency can be written as,

$$\Phi_{sh} = \frac{\rho_i hdw}{\rho_a hdl}, \tag{6.12}$$

where l is the total length of the electrodes. Together with equation 6.11, this gives us:

$$\Phi_{sh} = X\frac{h}{l}\frac{v_x}{v_c}. \tag{6.13}$$

We see that the sweeping efficiency depends on the permeability of the sheet, the geometry of the device and the axial velocity of the sheet compared to the velocity of plasma leaking into the wake. The quantities h and l are known, and v_x and X are determined by the

current sheet velocity model in the previous section. In order to complete our model of the sweeping efficiency of the sheet, we must consider the flux of plasma from the sheet into the wake, specifically the velocity of ions towards the cathode, v_c.

6.2.1 The Motion of Ions in the Current Sheet

Let us consider an analysis in the frame of reference moving with the current sheet. A neutral particle moves with velocity v_x towards the sheet and at some point in the sheet it is ionized. The newly created electron will immediately begin drifting in the crossed electric and magnetic fields. Lovberg pointed out that if the newly created ion is free to gyrate it will also begin a drift motion and no polarization field between the two particles will arise [15]. However, if the ion's Hall parameter is low, it will initially remain stationary as the electron moves away, creating a polarization field. This will serve to decelerate the ion (in the sheet frame of reference) to zero velocity.

The former case (high ion Hall parameter) was observed by Lovberg in hydrogen current sheets, as evidenced by a lack of measured polarization field and an implied high level of ion current [15]. The low ion Hall parameter case was also observed by Lovberg in a heavier propellant, nitrogen, where a polarization field was measured and the ion current component was effectively zero [15]. This distinction in behavior is important for us to consider because the leakage of mass out of the sheet depends on the velocity of ions towards the cathode, or the ion current. In our experiments the ion Hall parameter is estimated to be on the order of 1 for helium and hydrogen, and less than 0.1 for argon and neon. The ion Hall parameter is calculated from the expression,

$$\Omega_i = \frac{eB}{m_i \nu_{ia}},\tag{6.14}$$

with the ion-ambient momentum transfer collision frequency, ν_{ia}, calculated from the ex-

pression,

$$\nu_{ia} = n_a v_{sh}(Q_{ia}^{es} + Q_{ia}^{cx}), \tag{6.15}$$

where Q_{ia}^{es} and Q_{ia}^{cx} are the elastic scattering and charge exchange collision cross sections, respectively.

A more transparent comparison, however, may be to consider the Larmor radius in comparison to the characteristic dimension of the sheet width. This is equivalent to the ion Hall parameter calculation if we instead estimate the ion-ambient collision frequency to be given by $\nu_{ia} \approx v_{sh}/w$. Here, w is the width of the sheet and we will consider it to be approximately 1 cm. In this case, if the Larmor radius, which is calculated from the expression,

$$r_L = \frac{m_i v_{sh}}{eB}, \tag{6.16}$$

is greater than or equal to 1 cm, the Hall parameter is in the "low" limit ($\Omega_i < 1$), and if $r_L < 1$ cm, the Hall parameter is in the "high" limit ($\Omega_i \sim 1$). The calculations of Larmor radius, according to equation 6.16 and shown in figure 6.4, put argon and neon in the first category and helium and hydrogen in the second.

In the case where $\Omega_i \approx \mathcal{O}(1)$, an ion's motion is determined by its drift velocity. From the steady-state ion and electron momentum equations we can solve for the velocity of the ions, $\mathbf{u}_i$, where $\mathbf{u}_i = \mathbf{U}_i + \mathbf{v}$, the sum of the ion drift and fluid velocities:

$$0 = en_i(\mathbf{E} + (\mathbf{v} + \mathbf{U}_i) \times \mathbf{B}) - \nabla \cdot \mathbf{p}_i - n_i m_i \left[\nu_{ie}(\mathbf{U}_i - \mathbf{U}_e) - \nu_{ia}(\mathbf{U}_i + \mathbf{v}) \right]. \tag{6.17}$$

$$0 = en_e(\mathbf{E} + (\mathbf{v} + \mathbf{U}_e) \times \mathbf{B}) + \nabla \cdot \mathbf{p}_e + n_e m_e \left[\nu_{ei}(\mathbf{U}_e - \mathbf{U}_i) + \nu_{ea}(\mathbf{U}_e + \mathbf{v}) \right]. \tag{6.18}$$
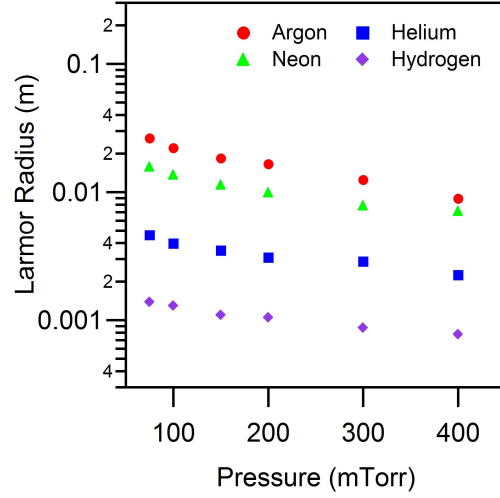
Figure 6.4: Calculated ion Larmor radius vs. pressure.

Here, $\mathbf{E}$ is the applied electric field, $\mathbf{v}$ is the fluid velocity of the sheet, $\mathbf{U}_i$ and $\mathbf{U}_e$ are the ion and electron drift velocities, and ν_{xy} is a momentum transfer collision frequency between particles x and y. If we assume that $n_e = n_i$, and using $\mathbf{U}_i + \mathbf{v} = \mathbf{u}_i$ and $\mathbf{U}_e + \mathbf{v} = \mathbf{u}_e$ (where $\mathbf{u}_i$ and $\mathbf{u}_e$ are the species velocities), the definition $\mathbf{j} = en_e(\mathbf{U}_i - \mathbf{U}_e)$ and $m_i n_i \nu_{ie} = m_e n_e \nu_{ei}$, these two equations simplify further to:

$$0 = \mathbf{E} + \mathbf{u}_i \times \mathbf{B} - \frac{\nabla \cdot \mathbf{p}_i}{en_e} - \frac{m_e \nu_{ei}}{n_e e^2}\mathbf{j} - \frac{m_i \nu_{ia}}{e}(\mathbf{u}_i). \tag{6.19}$$

$$0 = \mathbf{E} + \mathbf{u}_e \times \mathbf{B} + \frac{\nabla \cdot \mathbf{p}_e}{en_e} - \frac{m_e \nu_{ei}}{n_e e^2}\mathbf{j} + \frac{m_e \nu_{ea}}{e}(\mathbf{u}_e). \tag{6.20}$$

Subtracting equation 6.20 from equation 6.19, we find:

$$\frac{m_i \nu_{ia}}{e}\mathbf{u}_i = \mathbf{u}_i \times \mathbf{B} - \mathbf{u}_e \times \mathbf{B} - \frac{\nabla \cdot \mathbf{p}}{en_e} - \frac{m_e \nu_{ea}}{e}\mathbf{u}_e. \tag{6.21}$$

Solving for $\mathbf{u}_i$ and utilizing the definitions of $\mathbf{j}$ and Ω_i, we now have:

128

$$\mathbf{u}_i = \frac{\Omega_i}{en_e} \left[\frac{\mathbf{j} \times \mathbf{B}}{B} - \frac{\nabla \cdot \mathbf{p}}{B} \right] - \frac{m_e \nu_{ea}}{m_i \nu_{ia}} \mathbf{u}_e. \tag{6.22}$$

Because of the ratio of electron to ion mass, we can neglect the last term. We can also compare the order of magnitude of the pressure gradient term to the $\mathbf{j} \times \mathbf{B}$ term.

$$|jB| = \frac{|J||B|}{|w||d|} \sim \frac{\mathcal{O}(10^5)\mathcal{O}(10^{-1})}{\mathcal{O}(10^{-2})\mathcal{O}(10^{-1})} = \mathcal{O}(10^7) \, \mathrm{N/m^3}. \tag{6.23}$$

$$\left| \frac{\partial p}{\partial x} \right| = \frac{|n||kT_e|}{|w|} \sim \frac{\mathcal{O}(10^{22})\mathcal{O}(10^{-19})}{\mathcal{O}(10^{-2})} = \mathcal{O}(10^5) \, \mathrm{N/m^3}. \tag{6.24}$$

Therefore the pressure gradient that exists in the sheet contributes a negligible force. For the ion velocity, we have:

$$\mathbf{u}_i = \frac{\Omega_i}{en_e} \frac{\mathbf{j} \times \mathbf{B}}{B}. \tag{6.25}$$

Solving for $\mathbf{u}_e$ using, again, the definition of $\mathbf{j}$, we find:

$$\mathbf{u}_e = \frac{\Omega_i}{en_e} \frac{\mathbf{j} \times \mathbf{B}}{B} - \frac{1}{en_e} \mathbf{j}. \tag{6.26}$$

In this limit the ions move perpendicularly to the current, in the $\mathbf{j} \times \mathbf{B}$ direction. Thus the ion's cathode-directed velocity must be related to their velocity in the x direction (sheet velocity) by $v_c = v_x \tan \theta$ (see figure 6.5).

Alternatively, in the limit of $\Omega_i << 1$, the ions are not able to complete a gyration motion, so their motion is determined instead entirely by the polarization field that arises in the x direction. This field serves to slow ions to zero velocity in the sheet's frame of reference. In reality, it is likely that this process does *not* fully slow all of the ions, which could explain the observed permeability in these sheets (we will return to this discussion in section 6.4).
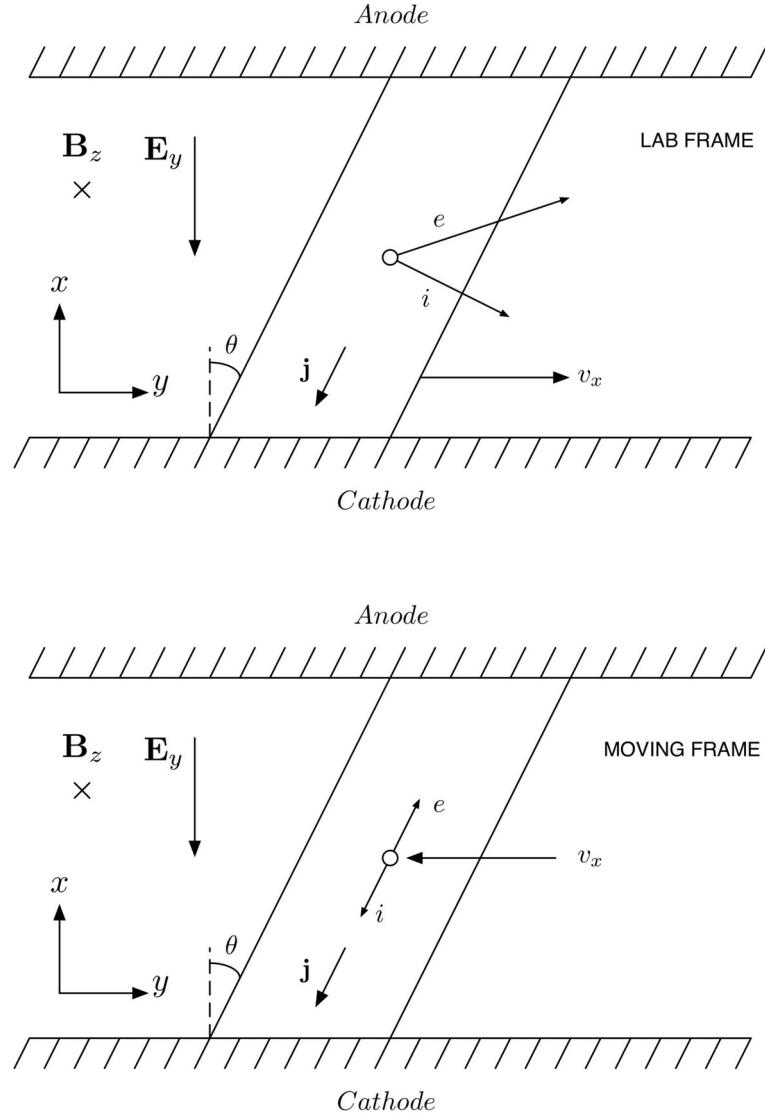
Figure 6.5: Diagram of the behavior of ions and electrons in the lab frame and moving frame when $\Omega_i \sim 1$. Both ions and electrons are free to follow drift motions, and no polarization field arises. The resulting ion current constitutes a *directed* leakage of plasma.
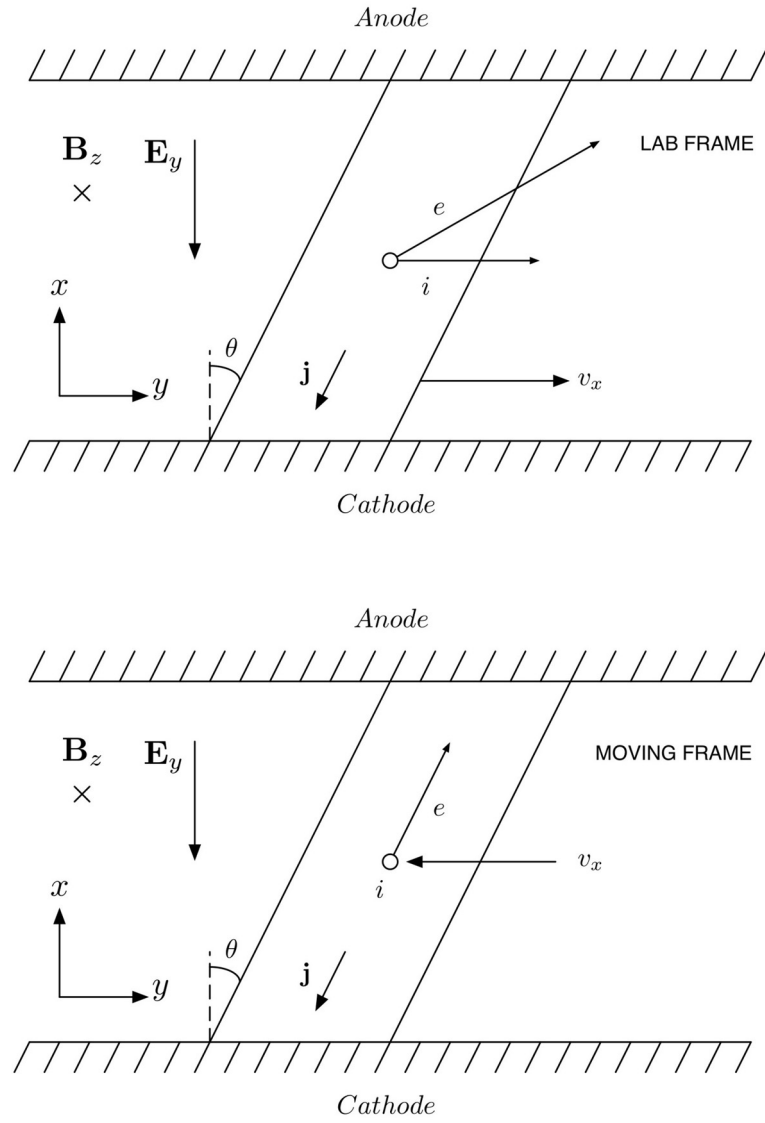
Figure 6.6: Diagram of the behavior of ions and electrons in the lab frame and moving frame when $\Omega_i << 1$. The motion of ions is entirely due to the polarization electric field that arises from a charge separation of ions and electrons. In the moving frame this field is just sufficient to decelerate the ions to zero velocity in the moving frame of reference of the sheet. With no ion current, the leakage of plasma at the cathode is *diffusive*.

131

Because the ions have no motion in the y direction in this limit, electrons carry all of the current, and there is no directed leakage of ions at the cathode (see figure 6.6). Since the directed leakage has been reduced to effectively zero in this case, the dominant leakage process to the cathode is instead diffusion. Therefore, for the flux of particles leaking out of the sheet we use,

$$\Gamma^l = \rho_c(\bar{c}/4)wd = \rho_c wd \frac{1}{4}\left(\frac{8kT_e}{\pi m_i}\right)^{\frac{1}{2}}. \tag{6.27}$$

Here we have deviated from our previous simplification of a single ion density in the entire sheet by defining instead a density at the cathode ρ_c. This is because we have found experimentally that the density in the sheet increases from anode to cathode, such that the average density relates roughly to the density near the cathode by $\rho_i \approx (2/3)\rho_c$ (see section 4.7).

We have identified two limits of the current sheet mass leakage behavior, the directed mass flux leakage, which dominates when the ion Hall parameter is on the order of 1, and diffusive mass flux leakage, which dominates when $\Omega_i << 1$. In the first case we see that with $v_c = v_x \tan\theta$ the expression for the sweeping efficiency (equation 6.13) reduces to,

$$\Phi_{sh} \approx X\frac{h}{l}\frac{1}{\tan\theta}. \tag{6.28}$$

When diffusion is the dominant mode of mass leakage at the cathode, Φ_{sh} is calculated from the expression,

$$\Phi_{sh} \approx X\frac{2}{3}\frac{h}{l}\frac{v_x}{(\bar{c}/4)}. \tag{6.29}$$

This equation was obtained by setting $\Gamma^e = \Gamma^l$ with Γ^e as previously defined, Γ^l as defined above (equation 6.27) and also using $\rho_i/\rho_c = 2/3$. Sheet velocity measurements give us the inputs X and v_x, but in this case the electron temperature must also be known to calculate

132

$\bar{c}/4$. In the next subsection we present the requisite T_e measurements and in section 6.3 we discuss the results of using equations 6.28 and 6.29 to model the sweeping efficiency of our current sheets.

6.2.2 Electron Temperature Measurements

It is necessary to measure the electron temperature in our argon and neon current sheets to use as inputs to the diffusive flux part of the model. Markusic measured the electron temperature in an argon discharge at 75 mTorr in this same device, finding that it was equal to $2.4 \pm .2$ eV [10].

We have measured the temperature in neon discharges over the range of pressure presented here, using line emission spectroscopy. The apparatus and technique for measuring the electron temperature this way was discussed in section 3.10. An example Boltzmann plot for neon at 300 mTorr is shown in figure 6.7. The temperature is determined from the slope of this plot, and we show the temperature measured this way over the range of pressures in figure 6.8.

For simplicity we will use the constant value of $kT_e = 2.6$ eV for all calculations in the model. The error associated with using this single value for all calculations should be very small.

At this point we can also address the assumptions, made earlier, that the plasmas in our current sheets are singly and fully ionized. These assumptions are justified, at least for the case of neon, by an equilibrium ionization calculation which shows that for neon at an electron temperature of 2.6 eV and a electron number density of 10^{22} m^{-3}, the effective ion charge is one [65].
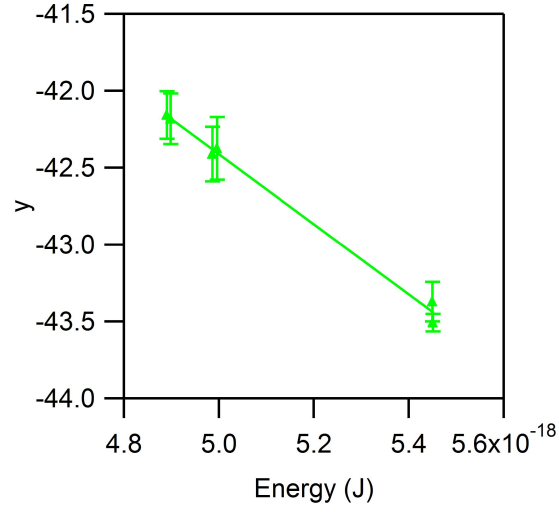
Figure 6.7: Boltzmann plot for a neon discharge at 300 mTorr pressure. The quantity y on the y axis is defined in equation 3.9. The slope of the line is equal to $-1/kT_e$, in this particular case $kT_e = 2.6 \pm .2$ eV.
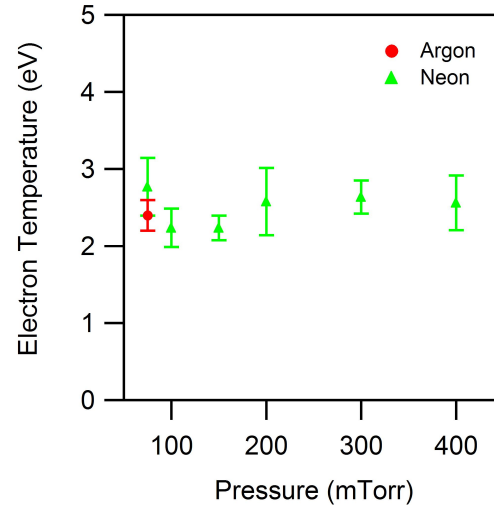

Figure 6.8: Electron temperature versus pressure for neon. The single argon data point is a measurement by Markusic in the same accelerator [10].

6.3 Results of the Model

The results of the current sheet velocity model of section 6.1 are shown in figures 6.9 and 6.10. In these figures we compare the velocities measured with photography (from section 5.3.1) to the predicted velocities. Both velocities have been non-dimensionalized, as discussed in section 5.7.2. For the expected velocity of hydrogen, equation 6.7 is used, because it is a diatomic molecule, whereas for the other propellants equation 6.6 is used. Because the degree of permeability of these current sheets is unknown, the parameter X in these equations is not independently known, but we will use the measured velocities to predict X. In figure 6.9 we have used $X = 0.2$ for argon and $X = 0.3$ for neon to match the modelled and measured velocities. For helium and hydrogen, $X = 1$ was used. The implications of this will be discussed in the next section.

The modelled non-dimensional velocity is not perfectly constant with pressure because the total current values used in equations 6.6 and 6.7 are the measured values from section 5.1, which vary slightly with pressure.

Figures 6.11 and 6.12 show the measured sweeping efficiencies in argon and neon, and helium and hydrogen respectively, with the modelled results included. We have found that the diffusive leakage model captures the trend of the sweeping efficiency of argon and neon current sheets well, while the directed leakage model describes helium and hydrogen current sheets due to the effect of the ion Hall parameter described in the previous section. Therefore, the modelled Φ_{sh} in figure 6.11 is the calculated value from equation 6.29, while the curves in figure 6.12 are calculated from equation 6.28.

For the most part, and considering the simplicity of the model, the model results match the experimental results well. Although the prediction from equation 6.28 is slightly low compared to the helium and hydrogen measurements, it captures the lack of dependency of the sweeping efficiency on pressure for these sheets. The argon and neon measurements,
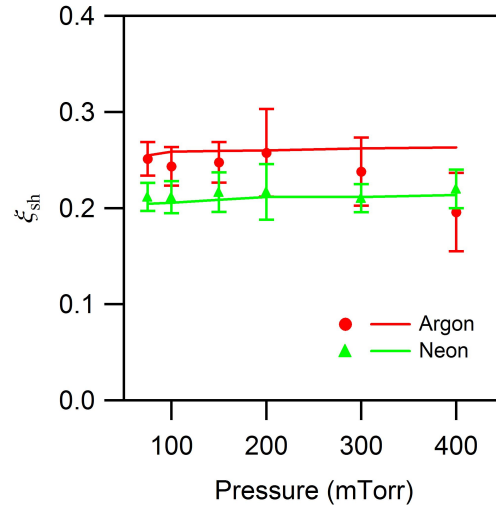
Figure 6.9: Non-dimensional current sheet velocity vs. pressure for argon and neon. The markers are measurements from the previous chapter, while the lines are the expected velocities from equation 6.6, with $X = 0.2$ for argon and $X = 0.3$ for neon.
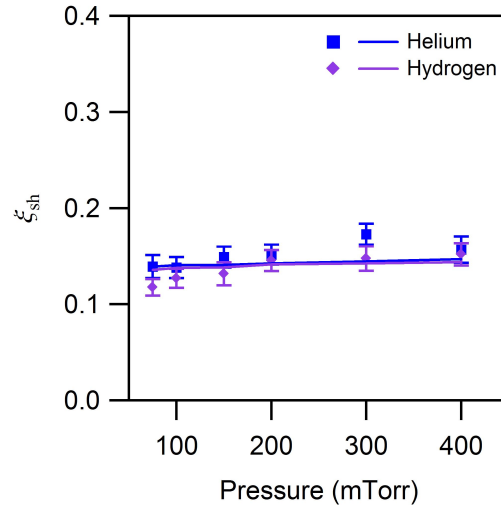

Figure 6.10: Non-dimensional current sheet velocity vs. pressure for helium and hydrogen. The markers are measurements from the previous chapter, while the lines are the expected velocities from equation 6.6 for helium and 6.7 for hydrogen. $X = 1$ is used for both propellants.
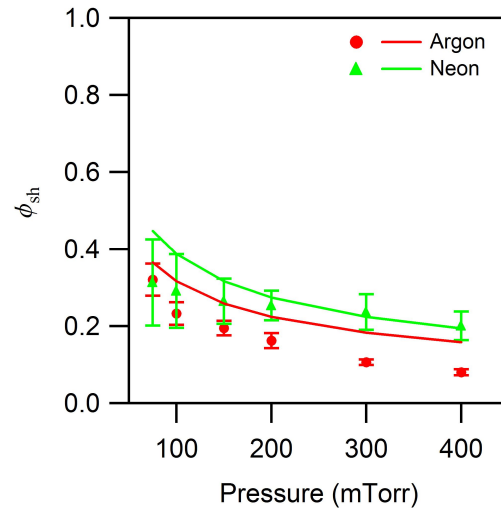
136

Figure 6.11: Non-dimensional current sheet mass vs. pressure for argon and neon.
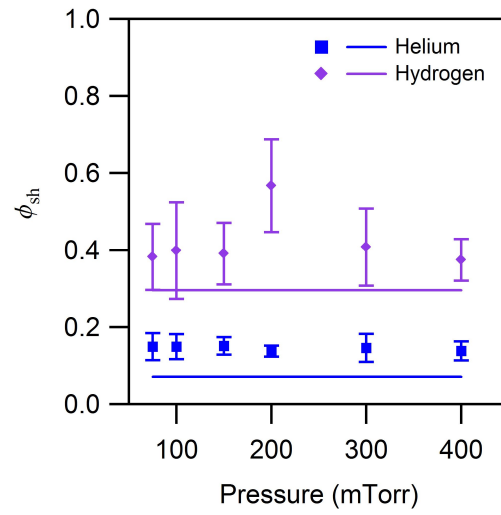

Figure 6.12: Non-dimensional current sheet mass vs. pressure for helium and hydrogen.

137

by contrast, show a dependency on propellant fill pressure, which is captured by the model through equation 6.29. Here the model's predictions are slightly high. Qualitatively this is to be expected because diffusive leakage is the minimum expected flux. Any small amount of directed leakage that exists in these sheets will tend to lower the predicted sweeping efficiency, bringing the model results closer to the measurements. Having verified the model as a good predictor of the observed behavior, we can now consider the insights that can be gained from it.

6.4   Insight Gained from the Model

The purpose of creating a simplified model of the current sheet is to gain insight about the various factors that influence the sweeping process. A computer model including all effects would perhaps give us a better prediction of measured quantities, but at the expense of complication that obscures insight. Our model tells us that the sweeping efficiency of a current sheet propagating into a ambient density of neutral gas is determined by the interplay of two processes: the flux of mass entering the sheet (the rate of mass encountered minus the rate of permeability) and the leakage of ions at the cathode into the wake.

Current sheets of the heavier propellants (argon and neon) are found to differ from the current sheets of the lighter propellants (helium and hydrogen) in behavior in both of these processes. Comparison of the measured current sheet velocities to the predicted values show that the heavier propellant current sheets are subject to permeability, while the lighter propellants are not. This is very much consistent with the findings of the restrike current sheet mass measurements in section 5.4.2. We found that the restrike current sheet, which sweeps up the neutrals that are left behind in the electrode gap due to permeability, was of significant mass for argon and neon and nearly zero mass for helium and hydrogen. The same conclusion is drawn from the velocity measurements presented here, that the

argon and neon sheets move too fast to possibly sweep up all the neutral gas; they must be permeable. The helium and hydrogen sheets, however, move at approximately the velocity that would be expected if they were impermeable.

Permeability reduces the flux of mass entering the sheet while increasing the sheet velocity. When considering the flux of mass leaving the sheet, a comparison of the measured sweeping efficiencies to the predicted sweeping efficiencies shows that the heavier propellant sheets are better described by a *diffusive* leakage model, while the lighter propellant sheets are well described by a *directed* leakage model. This means that while the lighter propellant's sheets are impermeable to the neutrals (they effectively sweep up propellant gas), they are prone to directed leakage of ions at the cathode. By contrast, argon and neon sheets are prone to permeability (perhaps due to an inefficiency of the polarization field at accelerating ions), but tend not to direct ions towards the cathode. Thus we have found that these heavier propellant sheets have higher permeability, but lower leakage.

We are now prepared to use the insight gained from this model to explain how current sheet mass leakage affects the trends in performance data observed in the last chapter. There we observed that the difference in the trend of the sweeping efficiency between the heavier and lighter propellant's current sheets strongly affects their performance trends. Specifically, the decreasing non-dimensional current sheet mass for argon and neon causes their performances to decrease or remain constant with pressure, respectively, while the constant non-dimensional current sheet mass for helium and hydrogen allows for an increase in the performance with pressure when operating with those propellants. We can explain the difference in the non-dimensional mass trends by a difference in the mechanism of mass leakage, with a diffusive leakage dominating for the heavier propellants and a directed leakage dominating for the lighter propellants.

The model presented here concentrated chiefly on the current sheet mass leakage pro-

139

cess and therefore does not explain all of the observed performance trends. Unanswered questions remain, and principal among them are the particulars of the permeability process which is seen to occur for argon and neon but not for helium and hydrogen. Here we have made a gross simplification that a percentage of the propellant permeates through the sheet without any acceleration. In reality there is probably a distribution of velocities of these neutrals and they also must interact in some way with the wake after permeating through the sheet. This also leads to the question of what causes the non-dimensional wake velocity to increase with pressure for helium and hydrogen (leading to a performance increase with pressure for those sheets).

Despite these shortcomings, this model of the current sheet adds to our understanding of the performance measurements of the previous chapter.

6.5   Summary

In this chapter we have developed a model of the propagation phase of the current sheet. The purpose of this model was to gain insight into the current sheet mass leakage process and how it effects the performance of the accelerator. A model of the current sheet velocity shows us that argon and neon propellant current sheets are prone to permeability whereas helium and hydrogen current sheets are not. From a model of the current sheet mass we have found that there is a dependence of the leakage process on the ion Hall parameter, with diffusive leakage dominating for the heavier propellants and directed leakage dominating for the lighter propellants. The effect of these leakage mechanisms on the performance of the device is to make the non-dimensional impulse and efficiency decrease or stay constant with pressure for argon and neon while increasing with pressure for helium and hydrogen.

Chapter 7

Conclusions

The research outlined in this dissertation has focused on the impact of current sheet mass leakage on the performance of a pulsed electromagnetic plasma accelerator. It was clear from previous research that gas-fed pulsed plasma thrusters were vulnerable to leakage of mass out of the current sheet into a wake at the cathode, and that this behavior could be detrimental to the performance of the device. We have endeavored to uncover the consequences of this behavior through experimental investigation of the mass and velocity of the sheet and wake structures as well as a model of the current sheet to explain the trends in performance. The major findings of this research are related in the next section and finally recommendations for future research are outlined.

7.1   Major Findings of this Work

This study has illuminated the problem of current sheet mass leakage in pulsed plasma accelerators, and the effect of leakage on the performance of the device. We find that current sheet mass leakage has a strong effect on the performance, one that is measurable,

can be explained by models and is dependent on the operating conditions of propellant species and pressure. Specifically, the major findings of this work are:

- Current sheet mass leakage is a ubiquitous phenomenon in our device, occurring in all operating conditions of different propellants and pressures.

- After an initial bifurcation phase, the current sheet in this device enters a steady-state phase of propagation during which the mass, velocity and canting angle are all approximately constant.

- The performance parameters non-dimensional impulse and efficiency decrease with increasing propellant pressure for discharges using argon propellant, because of lower sweeping efficiency at higher pressures.

- The performance of neon discharges stays constant with pressure because the loss of mass from the current sheet is made up for by a commensurate increase in wake mass.

- The performance of helium and hydrogen discharges increases with pressure, because the sweeping efficiency is constant with pressure and the wake velocity increases.

- The trends in the behavior of the sweeping efficiency, or non-dimensional current sheet mass, have been explored with an analytical model of the current sheet. The model allows us to suggest that:

  – For the lighter propellants, which have a higher ion Hall parameter, the ions in the sheet have a motion perpendicular to the canted current, and thus are subject to a directed motion towards the cathode, causing a high degree of leakage

142

of plasma into the wake. At the same time, these sheets show no signs of permeability.

- For the heavier propellants, with low ion Hall parameters, the ions cannot complete gyrations, therefore ions are not directed towards the cathode and these sheets are subject only to a diffusive leakage of plasma into the wake. However, these sheets are found to be highly permeable to the ambient propellant.

7.2 Future Research Recommendations

In this work we have shown experimentally that the performance of the accelerator is effected by current sheet mass leakage, and we have explained how this leakage manifests itself under different operation conditions. However, there remain a few unanswered questions.

Principle among these is the issue of current sheet permeability. We have demonstrated that for the heavier propellants permeability is at least as big an issue as leakage, possibly bigger. The exact mechanism of the permeability of gas through the current sheet is not known, but our experiments and model have hinted that this process is related to the ability of ions to "keep up" with the current sheet due to their low ion Hall parameters.

Related to the permeability issue is the issue of what happens behind the sheet. In this work we have not dealt with this region, but surely there must be an exchange of particles between neutrals that have permeated through the sheet and wake ions that may drift out of the wake. Examining these processes may help determine the mass and velocity of the wake more accurately, both of which directly impact the impulse of the accelerator. For example, in this study we have focused on the effect of mass leakage on the current sheet mass, but we have also noted that the differences in performance between the different propellants can be partially explained through differences in their wake masses (for argon

and neon) and in wake velocities (for helium and hydrogen).

Finally, a useful future experimental study in this device would be to examine in more detail evidence for the proposed diffusive vs. directed leakage theory. One experiment that could be implemented is a measurement in the sheet with an electric field probe, to check for the polarization field that should arise in the heavier propellant current sheets [15].

Appendix A

Example Grid Measurements

The following six graphs are examples of measured plasma parameters that were made in a grid of measurement points. All measurements were made under the conditions of the detailed study in chapter 4: argon propellant, 100 mTorr pressure, and 9 kV voltage.

In each figure we plot the measured B and j versus time, and in the cases where n_e was measured it is also included. B and n_e are plotted on the left axis while j is plotted on the right axis. Measurements are shown for only 14μs because this is the minimum time frame over which each of the measurements was made.

In each figure data is plotted for six different locations. These locations correspond to 6.03, 12.38, 18.73, 25.08, 31.43, and 37.78 cm from the breech (x direction) in the six frames from bottom to top, respectively. Figure A.2 data is from the first vertical row of data, 0.48 cm from the cathode. Figure A.3 data is 1.27 cm from the cathode. Figure A.4, 2.06 cm. Figure A.5, 3.02 cm. Figure A.6, 3.81 cm. Figure A.7, 4.60 cm. These locations are shown in figure A.1.
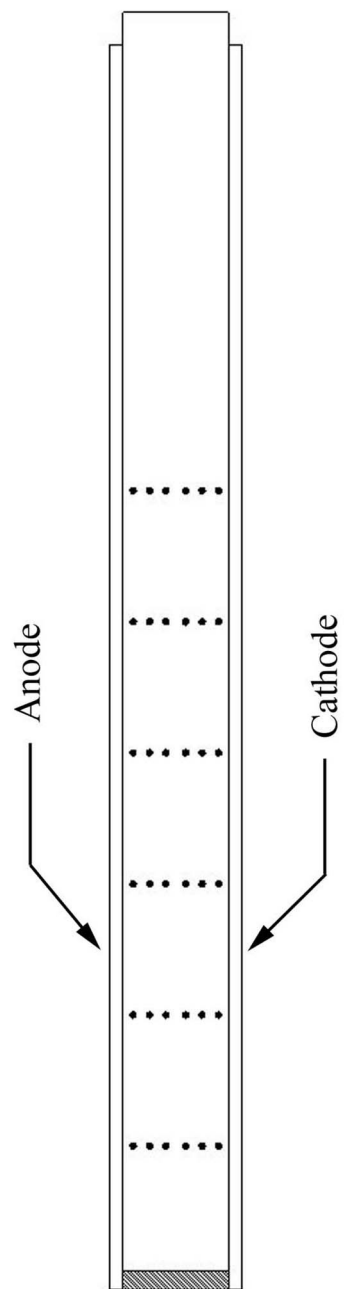
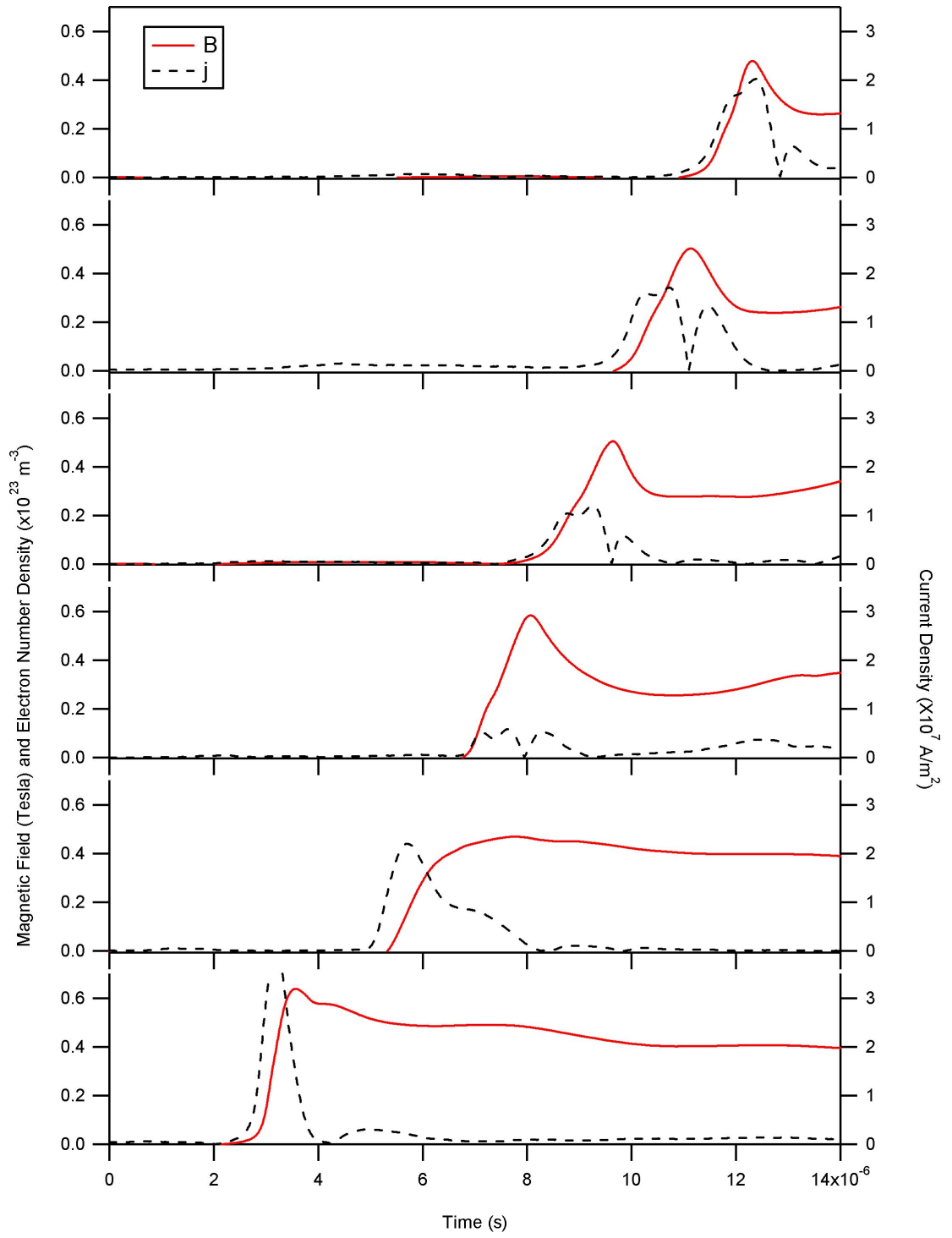Figure A.1: Columns of measurement points of the following six graphs.

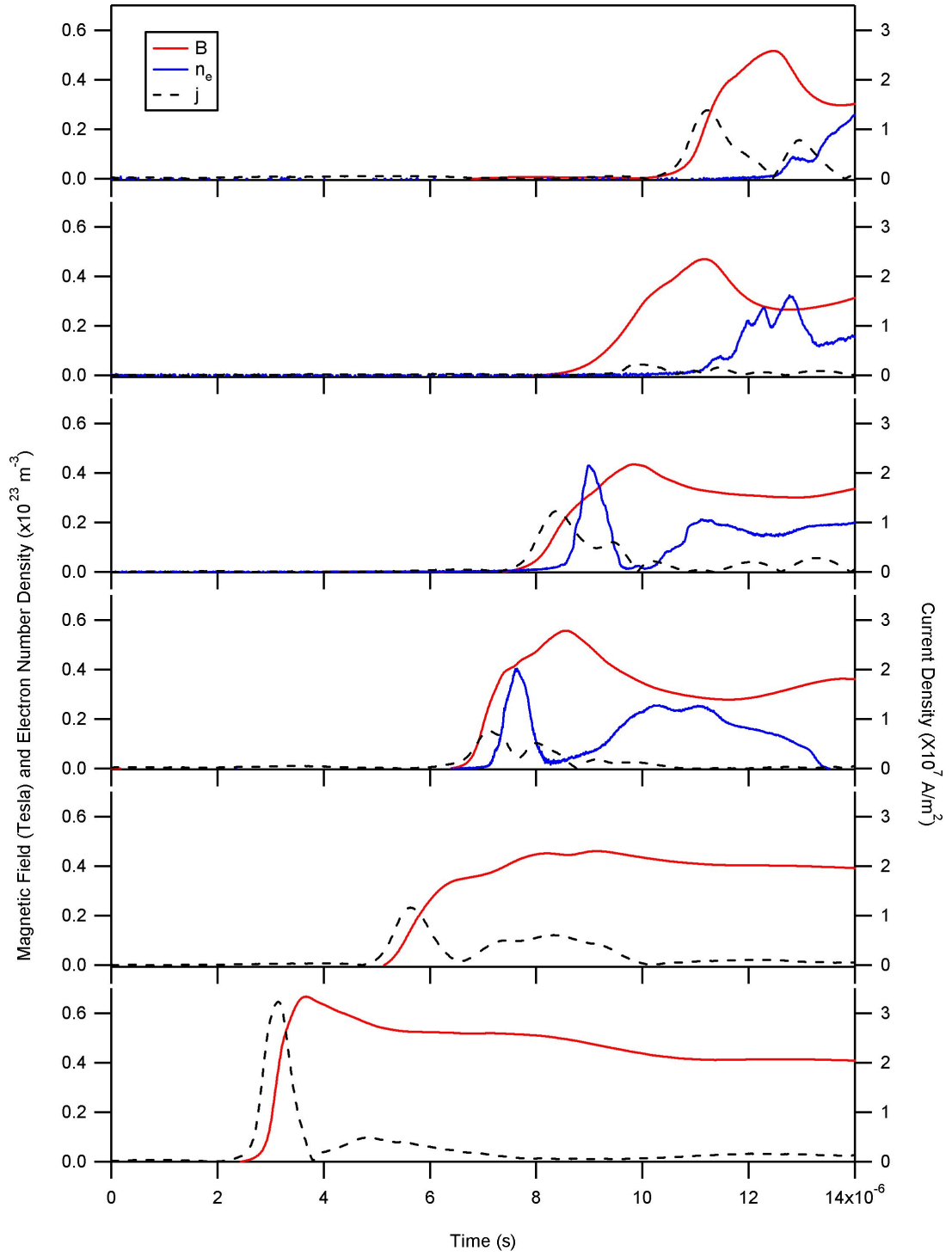Figure A.2: B and j vs. time at 6 horizontal positions in row 1.

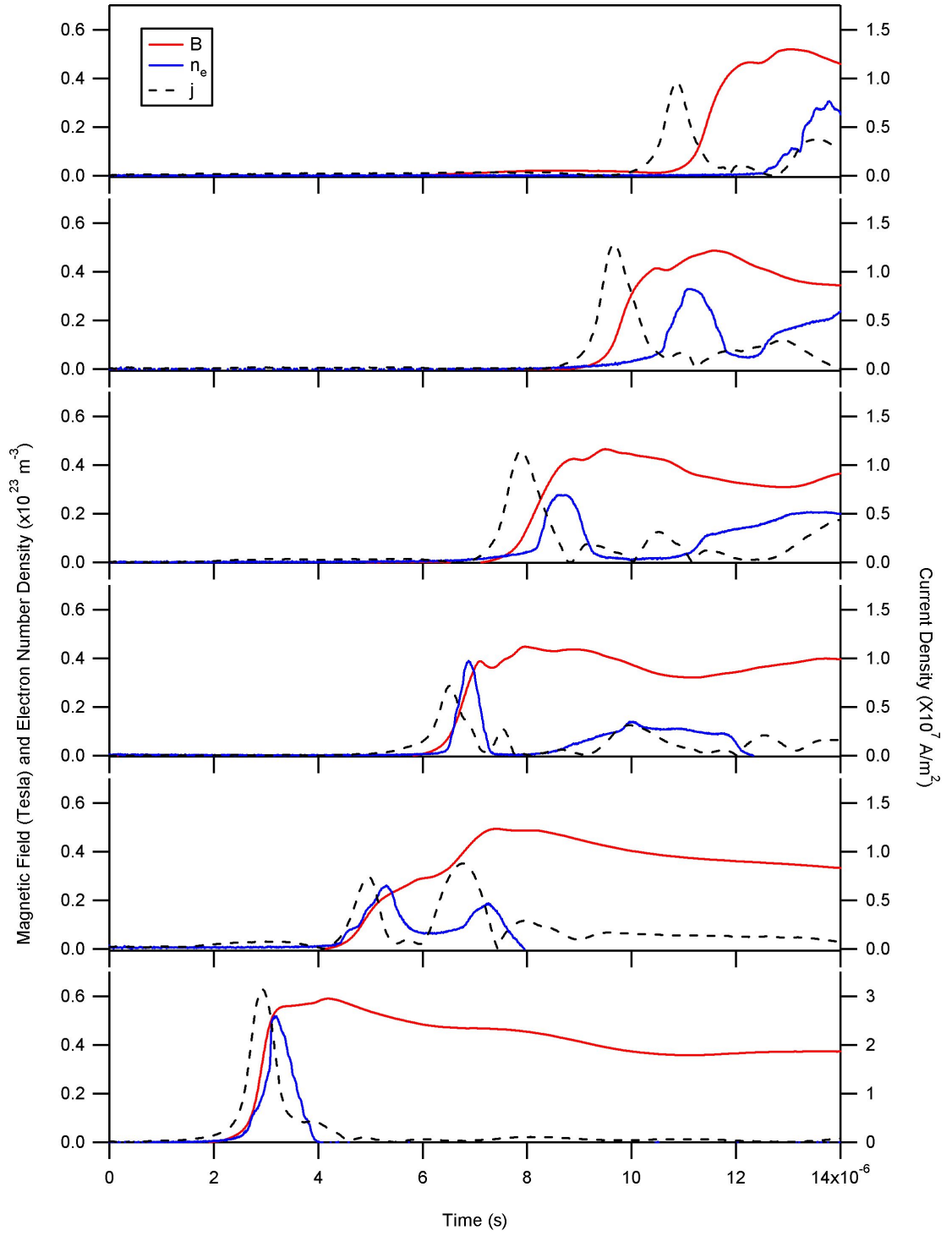Figure A.3: B, n_e, and j vs. time at 6 horizontal positions in row 2.

Figure A.4: B, n_e, and j vs. time at 6 horizontal positions in row 3.

Figure A.5: B, n_e, and j vs. time at 6 horizontal positions in row 4.
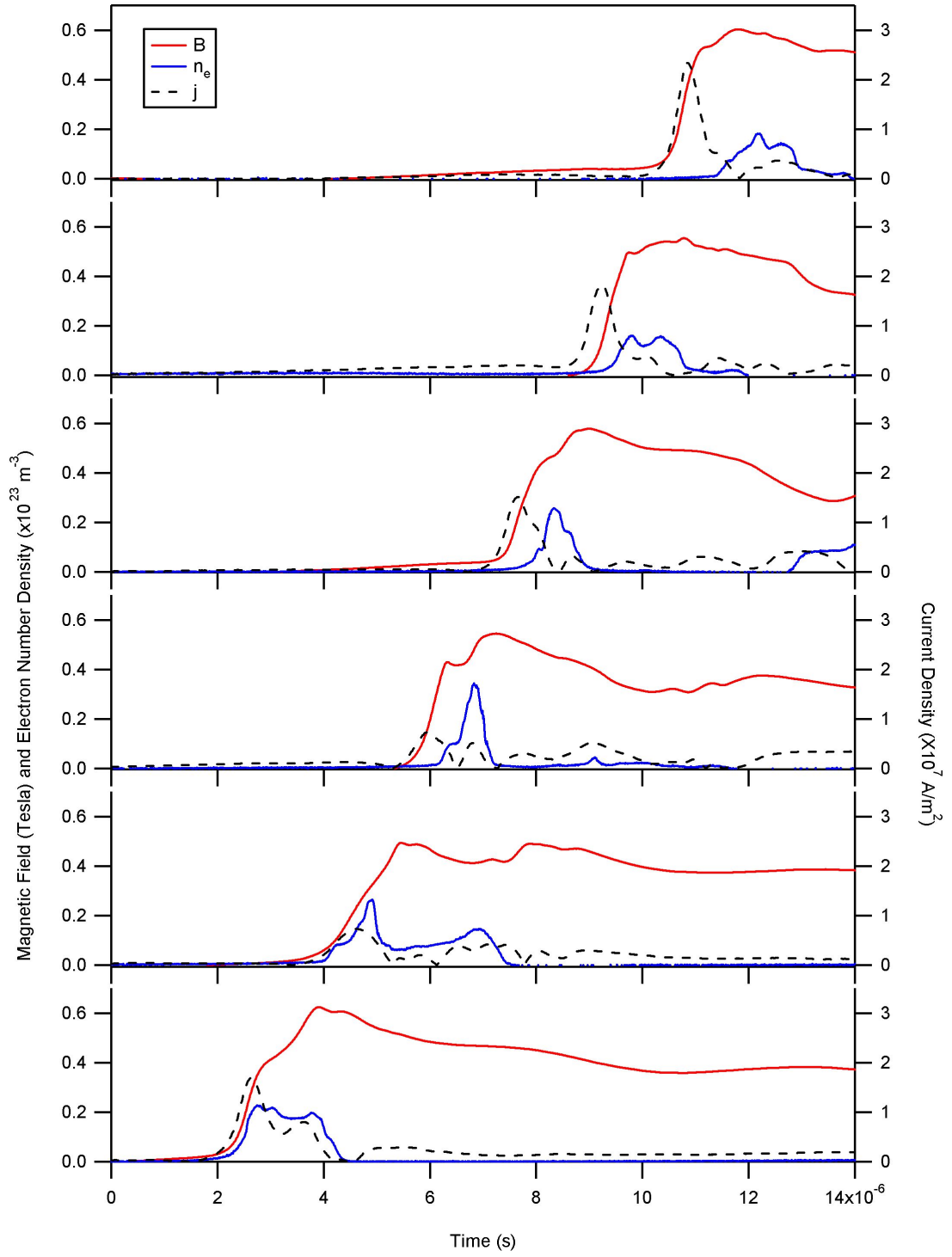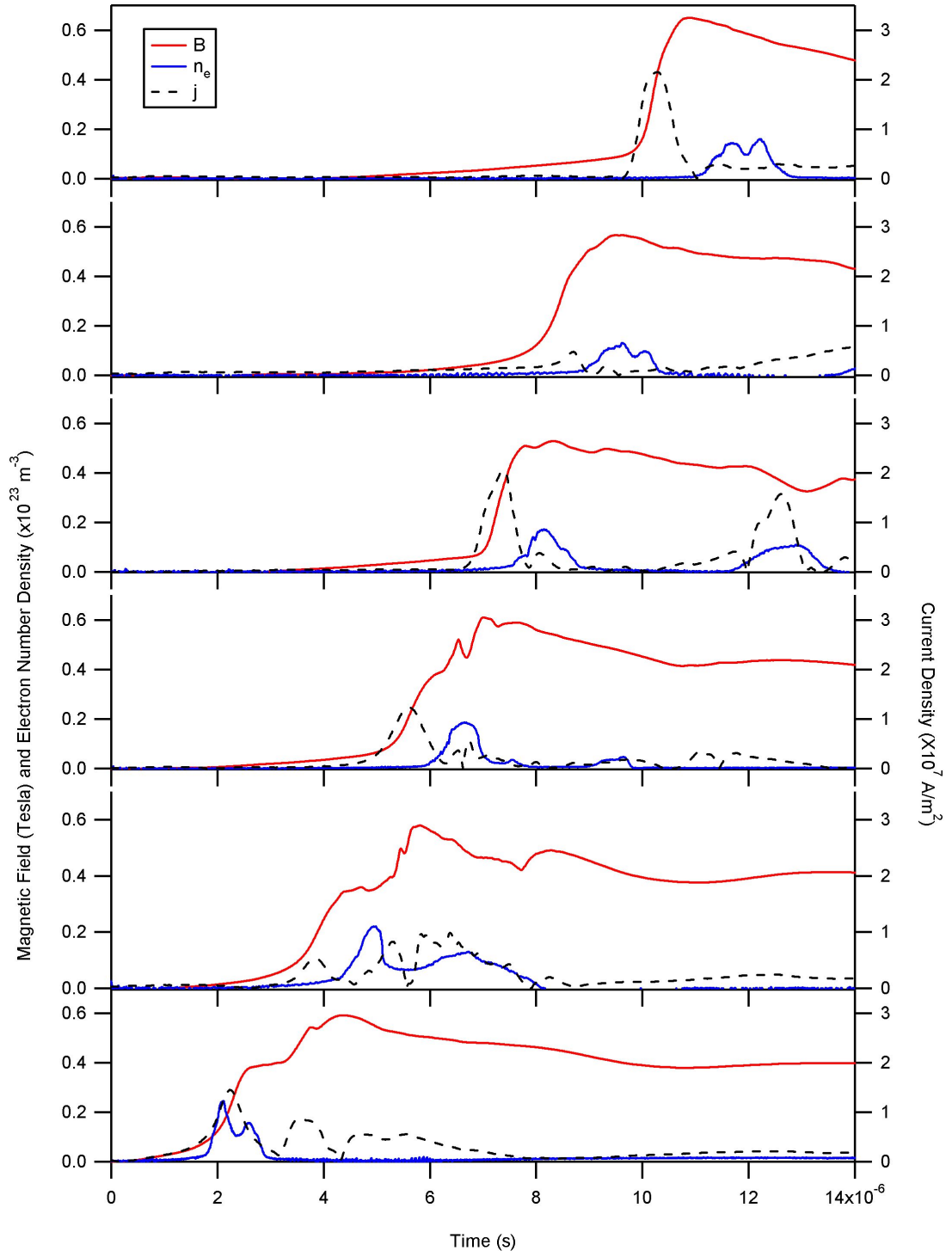
150

Figure A.6: B, n_e, and j vs. time at 6 horizontal positions in row 5.
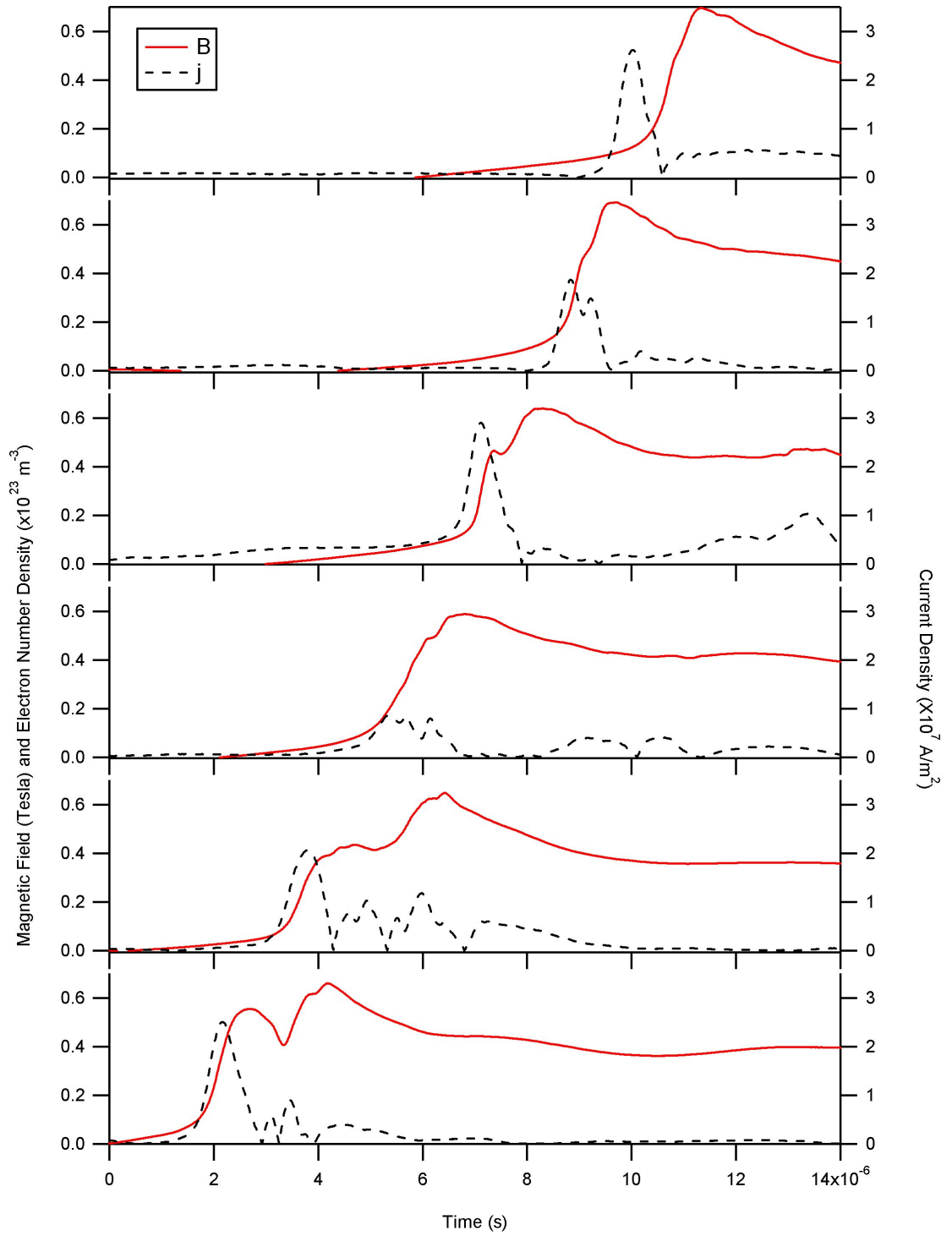
151

Figure A.7: B and j vs. time at 6 horizontal positions in row 6.

152

Appendix B

Neon Photography

Photographs were taken of a neon discharge at 100 mTorr pressure, with either a neon ion filter or a neon neutral filter placed over the camera lens. This allows a comparison of the luminosity from the ions and neutrals, to see if there is any spatial separation of ions and neutrals for example. Of course, this comparison does not tell us the relative proportions of ions and neutrals.

This test was done with neon propellant because neon ions and neutrals both have emission lines in the visible spectrum. The filter used for the neon ions was Hoya U-340. This filter allowed capture of 369.42 nm wavelength light from the $2p^43s$ - $2p^4(^3P)3p$ neon ion line [66]. The photographs from this test are shown in figure B.1. The photographs were made in the same manner as the argon photographs presented in section 4.1.

The neon neutral line $2p^53s$ - $2p^5(^2P^0_{1\frac{1}{2}})3p$ was captured at 633.44 nm wavelength with a Corion S10-630-R-H966 filter [66]. The photographs from this test are shown in figure B.2.

These photographs appear less bright compared to the argon photographs shown before, because the emission lines were relatively dimmer. The camera aperture had to be opened farther to capture the light adequately.

These photographs are of a 13.5 cm by 5.08 cm area of the accelerator, with the cathode on the top and the anode on the bottom. The left edge of each frame is 7 cm from the breech of the accelerator. The current sheet is moving from left to right.

The timing of the frames is from top to bottom. The first frame is at 2.5μs into the discharge, and each subsequent frame is 0.5μs later. The sequence was made with four separate firings. In each the camera was delayed 0.5μs from the previous firing.

Although these photographic series do not appear to be exactly the same, they are quite similar. There does not appear to be a discernable separation of ions and neutrals. This implies that the ions and neutrals are well coupled with momentum transfer collisions. The structures that appear are also the same. There appears to be both ion and neutral populations in the sheet and wake. The neutrals appear to be less dense in the sheet as compared to the wake, however. This is not unexpected, but strong conclusions cannot be drawn due to the qualitative nature of photography as a measurement.
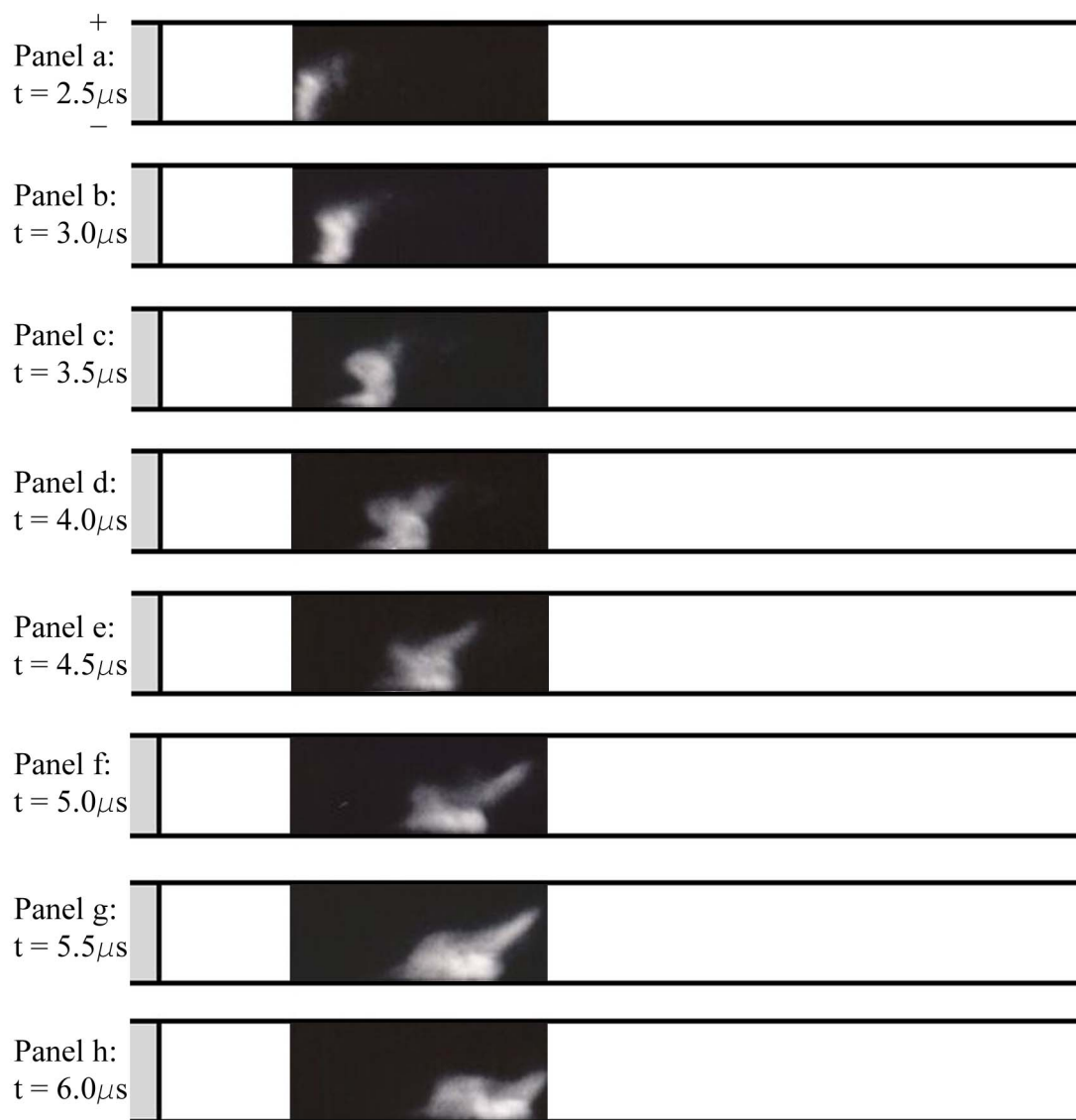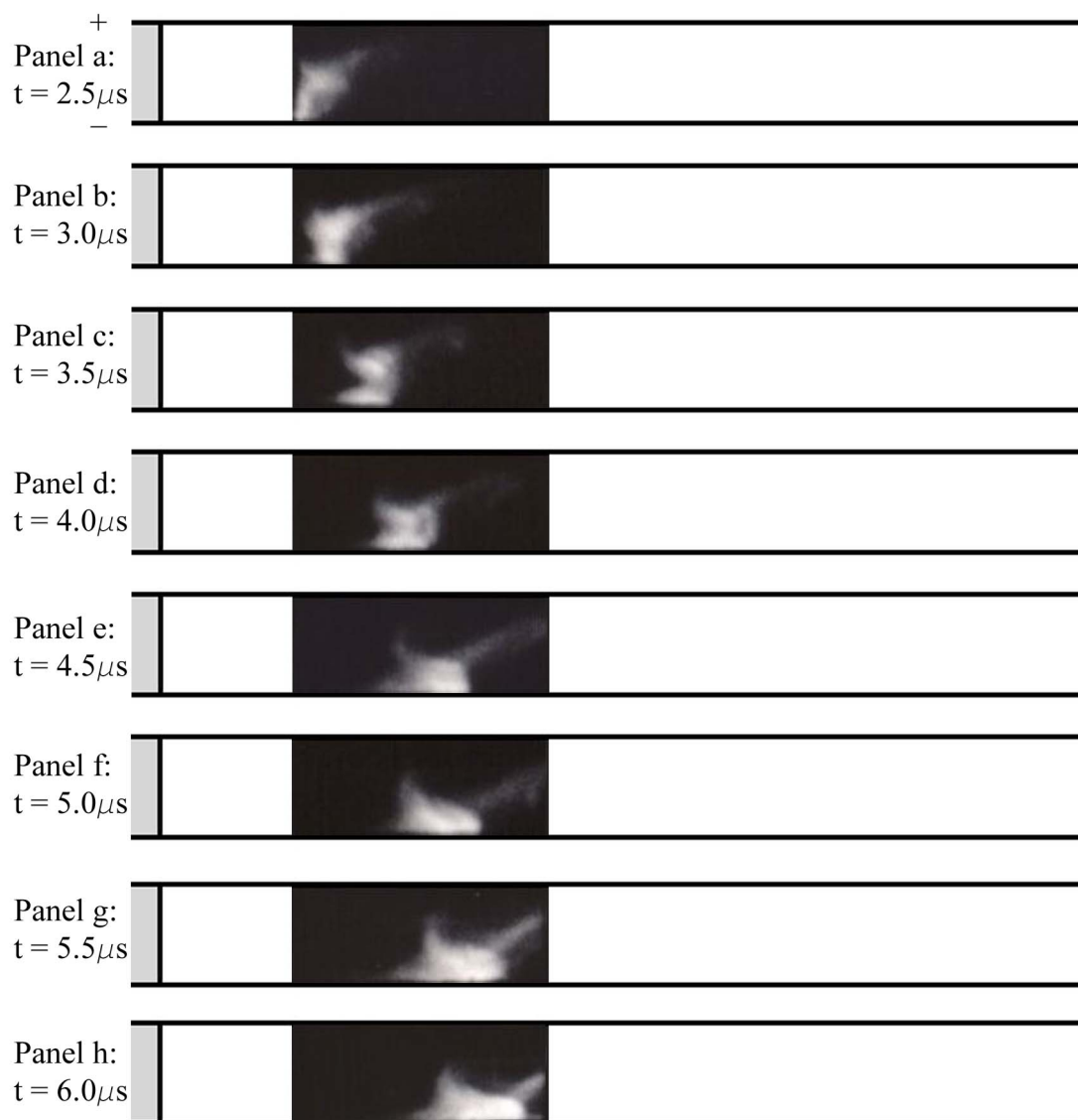
Figure B.1: Neon ion photographs.

Panel a:
t = 2.5μs

Panel b:
t = 3.0μs

Panel c:
t = 3.5μs

Panel d:
t = 4.0μs

Panel e:
t = 4.5μs

Panel f:
t = 5.0μs

Panel g:
t = 5.5μs

Panel h:
t = 6.0μs

Figure B.2: Neon neutral photographs.

156

Appendix C

Velocity Measurements with Deuterium Propellant

In section 6.1 we compared sheet velocity measurements to their expected values and found that for hydrogen, collisions between the sheet ions and the diatomic neutral molecules caused the velocity to be limited to two-thirds of the snowplow velocity. To test this hypothesis we made B-dot probe velocity measurements of current sheets in deuterium propellant. The results of these experiments are shown in figure C.1, and compared to the expected velocity from equation 6.7, using $\theta = 25°$ for deuterium (an estimate from the photographic measurements from reference [10]). There are no error bars included on the measurements because only two measurements were made at each condition. In general we can see from this comparison that the same result seen in hydrogen seems to be present in deuterium, validating the hypothesis that the velocity limitation is due to the propellant being diatomic.
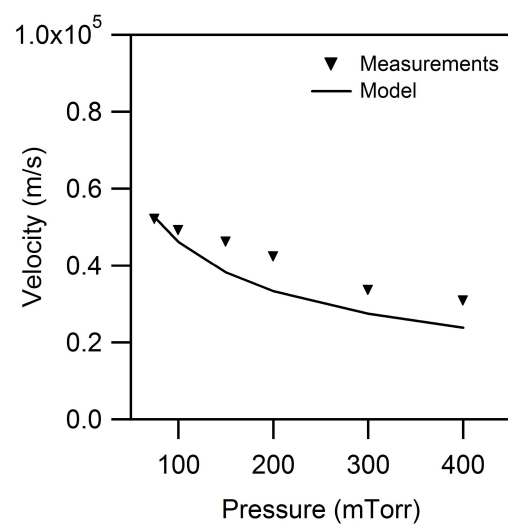
Figure C.1: Velocity versus pressure for deuterium, measured and modelled.

Appendix D

Experiments at Lower Energies

All of the experiments that have been reported in this dissertation were performed with a charging voltage of 9 kV, which gave a stored energy of 4050 J. We did perform some experiments at lower energies, however, and a sample of the results from those experiments is presented here. In general the expected results were found, that the current sheet densities and velocities were lower at lower energies.

D.1 Comparison of Argon 8 kV and 9 kV Measurements

In this section we compare measurements of peak electron number density made with argon propellant at 8 kV (3200 J) and over the usual range of propellant pressures to the previously reported argon 9 kV measurements (figure D.1). We can see that the peak density in the sheet is lower in the lower energy discharges.
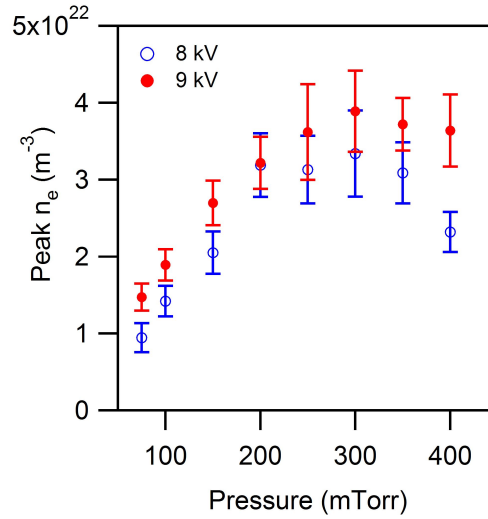
Figure D.1: Peak electron number density versus pressure for argon with 8 kV and 9 kV charging voltage.

D.2 Comparison of 6 - 9 kV Measurements in Various Propellants at 100 mTorr Pressure

In the bulk of this dissertation measurements were made with a constant charging voltage over a range of propellants and pressures. In this section we report some results of experiments performed while holding the *pressure* constant at 100 mTorr while varying the propellant species and *voltage*. Specifically, measurements of peak electron number density and velocity were made for argon, neon, helium and hydrogen at 100 mTorr and 6, 7, 8, and 9 kV (1800, 2450, 3200, and 4050 J). The peak density measurements are shown in figure D.2, and they display the expected behavior, higher density at higher energies. The B-dot probe measured current sheet velocities are displayed in figure D.3, and they show the same behavior, higher sheet velocities at higher energies. Neither of these plots have error bars on the measurements because there were only two measurements made at each condition.
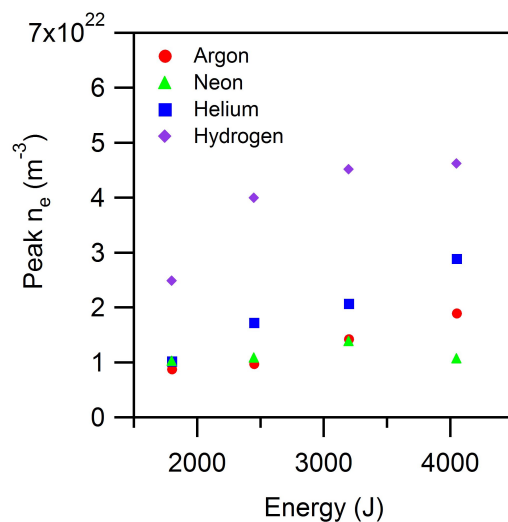
Figure D.2: Peak electron number density versus energy for all propellants at 100 mTorr pressure.
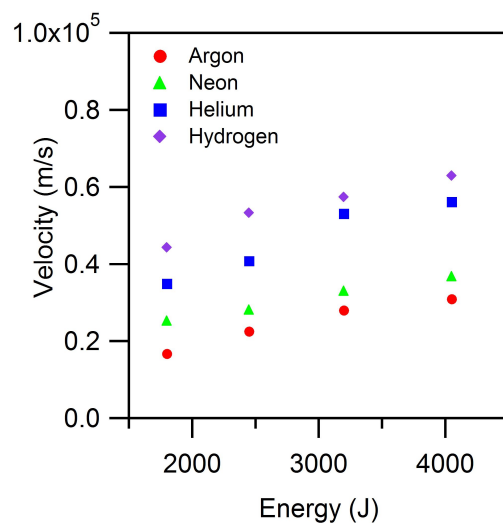

Figure D.3: Current sheet velocity versus energy for all propellants at 100 mTorr pressure.

Appendix E

Ionization in the Wake

Lovberg raised the question of why the wake remains ionized and does not quickly recombine into neutrals. He reached the conclusion that there must be current carried in the wake, parallel to the cathode [16]:

> It seems surprising that such an apparently dense plasma is able to maintain its ionization under these conditions... A likely explanation of what is observed here... is that the return current from the discharge is actually being carried along the cathode surface, in some fraction at least, by this boundary layer, and that this current, while not heating the plasma ions enough to cause rapid expansion of the gas away from the cathode, is able to maintain ionization at the level observed here.

It is clear from our photographs and electron number density measurements that the wake in our device has a high degree of ionization as well, although the ionization fraction is not known. It is instructive to consider an estimate of the recombination time scale in the plasma [52]. We can estimate the three-body recombination time scale as [67]:

$$\tau_{tbr} = \frac{1.14 \times 10^{38} * (T_i)^{4.5}}{(n_e)^2} \tag{E.1}$$

Here the ion temperature is in units of eV and electron density is in units of m^{-3}.

Using 10^{22} m^{-3} as the order of magnitude of the wake electron number density and 1 eV as the order of magnitude of the wake ion temperature, the three body recombination time scale is on the order of 1 μs. Since the wake persists as an ionized plasma for the duration of the pulse, which is about 25 μs, there must be some mechanism that keeps the wake ionized.

No current was observed in the wake from the magnetic field measurements of section 4.3, however the spatial resolution of the magnetic field mapping was limited, especially near the electrodes. It is possible that there is current in the wake that was undetected by our probing. An especially interesting side effect of current in the wake parallel to the cathode is that the $\mathbf{j} \times \mathbf{B}$ force density resulting from such a current would be directed towards the cathode. This current, then, could also serve as a mechanism for restricting the wake plasma to the cathode region, as is observed. The possibility of current in the wake remains unresolved, however.

Bibliography

[1] R.G. Jahn. *Physics of Electric Propulsion*. McGraw-Hill, 1969.

[2] R.G. Jahn and E.Y. Choueiri. Electric propulsion. In *Encyclopedia of Physical Science and Technology, 3rd Edition*, pages 125–141. Academic Press, 2002.

[3] E.Y. Choueiri. A critical history of electric propulsion: The first 50 years (1906-1956). *Journal of Propulsion and Power*, 20(2):193–203, 2004.

[4] R.H. Frisbee. Advanced space propulsion for the 21st century. *Journal of Propulsion and Power*, 19(6):1129–1154, November - December 2003.

[5] R.L. Burton and P.J. Turchi. Pulsed plasma thruster. *Journal of Propulsion and Power*, 14(5):716–735, 1998.

[6] D. Keefer and R. Rhodes. Electromagnetic acceleration in pulsed plasma thrusters. In 25th *International Electric Propulsion Conference*, Cleveland, Ohio, August 24-28 1997. IEPC 97-035.

[7] J.K. Ziemer. *Performance Scaling of Gas-Fed Pulsed Plasma Thrusters*. PhD thesis, Princeton University, 2001.

[8] J.K. Ziemer. A review of gas-fed pulsed plasma thruster research over the last half century. *Internal Report, Electric Propulsion and Plasma Dynamics Lab, Princeton University*.

[9] J.E. Cooley and E.Y. Choueiri. Fundamentals of PPT discharge initiation: Undervoltage breakdown through electron pulse injection. In 39rd *Joint Propulsion Conference*, Huntsville, Alabama, July 20-23 2003. AIAA 2003-5027.

[10] T.E. Markusic. *Current Sheet Canting in Pulsed Electromagnetic Accelerators*. PhD thesis, Princeton University, 2002.

[11] T.M. York and R.G. Jahn. Pressure distribution in the structure of a propagating current sheet. *Physics of Fluids*, 13(5):1303, 1970.

[12] L.C. Burkhardt and R.H. Lovberg. Current sheet in a coaxial plasma gun. *Physics of Fluids*, 5(3):341–347, March 1962.

[13] J.C. Keck. Current distribution in a magnetic annular shock tube. *Physics of Fluids*, 5(5):630–632, 1962.

[14] F.J. Fishman and H. Petschek. Flow model for large radius-ratio magnetic annular shock-tube operation. *Physics of Fluids*, 5(5):632–633, 1962.

[15] R.H. Lovberg. Acceleration of plasma by displacement currents resulting from ionization. *Proceedings of the Sixth International Conference on Ionization Phenomena in Gases*, 4:235–239, 1963.

[16] R.H. Lovberg. The measurement of plasma density in a rail accelerator by means of Schlieren photography. *IEEE Transactions on Nuclear Science*, 11(1):187–198, 1964.

[17] R.B. Johansson. Current sheet tilt in a radial magnetic shock tube. *Physics of Fluids*, 8(5):866–871, 1964.

[18] A.V. Larson, T.J. Gooding, B.R. Hayworth, and D.E.T.F Ashby. An energy inventory in a coaxial plasma accelerator driven by a pulse line energy source. *AIAA Journal*, 3(5):977–979, May 1965.

[19] T.J. Gooding, B.R. Hayworth, and R.H Lovberg. Instabilities in a coaxial plasma gun. *AIAA Journal*, 1(6):1289–1292, June 1963.

[20] J.R. MacLelland, A.S.V. MacKenzie, and J. Irving. Schlieren photography of rail-tube plasmas. *Physics of Fluids*, 9(8):1613–1615, 1966.

[21] R.L. Burton and R.G. Jahn. Acceleration of plasma by a propagating current sheet. *Physics of Fluids*, 11(6):1231–1237, 1968.

[22] W.R. Ellis and R.G. Jahn. Ion density and current distributions in a propogating current sheet, determined by microwave reflection technique. *Journal of Plasma Physics*, 3(2):189–213, 1969.

[23] W.R. Ellis. *An Investigation of Current Sheet Structure in a Cylindrical Z-Pinch*. PhD thesis, Princeton University, 1967.

[24] G.J. Pert. Current sheet structure in a parallel plate rail gun. *Physics of Fluids*, 13(8):2185–2192, 1970.

[25] T.M. York and E.K. Stover. Transient flow and heating in a pinched plasma column. *Physics of Fluids*, 17(1):127–130, 1974.

[26] K.F. McKenna and T.M. York. Transient flow and expansion of a pinch discharge in self-induced magnetic fields. *Plasma Physics*, 17:1–14, 1975.

[27] T.J. Gooding, A.V. Larson, B.R. Hayworth, and D.E.T.F. Ashby. Development of a coaxial plasma gun for space propulsion. Technical Report CR-54245, General Dynamics Space Science Laboratory, April 1965.

[28] T.E. Markusic, E.Y. Choueiri, and J.W. Berkery. Measurements of current sheet canting in a pulsed electromagnetic accelerator. *Physics of Plasmas*, 11(10):4847–4858, 2004.

[29] T.E. Markusic, J.W. Berkery, and E.Y. Choueiri. Visualization of current sheet evolution in a pulsed plasma accelerator. *IEEE Transactions on Plasma Science*, 33(2):528–529, April 2005.

[30] T.E. Markusic. Movie of a parallel-plate gas-fed pulsed plasma thruster discharge. http://www.princeton.edu/˜eppdyl/personnel/markusic.html.

[31] R.G. Jahn and K.E. Clark. A large dielectric vacuum facility. *AIAA Journal*, 4(6):1135, 1966.

[32] J. Maloch and J. Maftul. Use of internal probes for diagnostics of pulse plasma. *Czechoslovak Journal of Physics*, 26(3):269–281, 1976.

[33] G.G. Spanjers, E.J. Yadlowsky, R.C. Hazelton, and J.J. Moschella. Investigation of current channel migration in a conducting plasma between planar electrodes. *Journal of Applied Physics*, 79(5):2229–2236, 1996.

[34] F.C. Jahoda and G.A. Sawyer. Optical refractivity of plasmas. In R.H. Lovberg and H.R. Griem, editors,. *Methods of Experimental Physics, Volume 9 - Part B*, page 1, Academic Press, 1971.

[35] G.G Spanjers, K.A. McFall, F.S. Gulczinski, and R.A. Spores. Investigation of propellant inefficiencies in a pulsed plasma thruster. In 32rd *Joint Propulsion Conference*, Lake Buena Vista, Florida, July 1-3 1996. AIAA 1996-2723.

[36] W.L. Wiese. Spectroscopic diagnostics of low temperature plasmas: Techniques and required data. *Spectrochimica Acta Part B: Atomic Spectroscopy*, 46(6-7):831–841, 1991.

[37] H.R. Griem. *Plasma Spectroscopy*. McGraw-Hill, 1964.

[38] National Institute of Standards and Technology. NIST Atomic Spectra Database. http://physics.nist.gov/cgibin/AtData/main_asd.

[39] D.L. Clingman and T.L. Rosebrock. Comments on the validity of ballistic pendulum measurements with pulsed plasma accelerators. *AIAA Journal*, 1(5):1233–1234, May 1963.

166

[40] D.M. Wetstone. Coaxial plasmoid source of small aspect ratio. *Physics of Fluids*, 5(8):981–987, 1962.

[41] S.F. Goncharov, P.P. Pashinin, R.V. Serov, and V.P. Yanovsky. Hollow ballistic pendulum for plasma momentum measurements. *Review of Scientific Instruments*, 59(5):709–711, 1988.

[42] J. Marshall. Performance of a hydromagnetic plasma gun. *Physics of Fluids*, 3(1):134–136, 1960.

[43] A. Andrew and J.P. Fitzpatrick. Velocity and impulse of an accelerated plasma. *Physics of Fluids*, 4(1):160–161, 1961.

[44] J. Grun and B.H. Ripin. Ballistic pendula for measuring the momentum of a laser-produced plasma. *Review of Scientific Instruments*, 53(12):1878–1881, 1982.

[45] J. Marshall. Hydromagnetic plasma gun. In S.W. Kash, editor, *Plasma Acceleration*. Stanford University Press, 1960.

[46] W.L. Starr and J.T. Naff. Acceleration of metal-derived plasmas. In S.W. Kash, editor, *Plasma Acceleration*. Stanford University Press, 1960.

[47] D.G. Chavers and F.R. Chang-Diaz. Momentum flux measuring instrument for neutral and charged particle flows. *Review of Scientific Instruments*, 73(10):1–7, 2002.

[48] D.G. Chavers. Momentum flux measurements using an impact thrust stand. Presentation at the 46th APS-DPP Conference, Savannah, Georgia, November 15-19, 2004.

[49] D.G. Chavers. Personal Communication, November 2004.

[50] P.C. Stangeby. *The Plasma Boundary of Magnetic Fusion Devices*. Institute of Physics Publishing, 2000.

[51] W.L. Wiese, M.W. Smith, and B.M. Miles. *Atomic Transition Probabilities, Volume II*. National Bureau of Standards, 1969.

[52] J.W. Berkery and E.Y. Choueiri. Characterization of current sheet evolution in a pulsed electromagnetic accelerator. In 28th *International Electric Propulsion Conference*, Toulouse, France, March 17-24 2003. IEPC 2003-0307.

[53] J.W. Berkery. Movies of magnetic and interferometric experimental contours in a parallel-plate gas-fed pulsed plasma accelerator discharge. http://www.princeton.edu/~eppdyl/personnel/ berkery.html.

[54] I. Kohlberg and W.O. Coburn. A solution for three dimensional rail gun current distribution and electromagnetic fields of a rail launcher. *IEEE Transactions on Magnetics*, 31(1):628–633, 1995.

[55] T.E. Markusic and E.Y. Choueiri. Phenomenological model of current sheet canting in pulsed electromagnetic accelerators. In 28th *International Electric Propulsion Conference*, Toulouse, France, March 17-24 2003. IEPC 2003-0293.

[56] J.T. Cassibry, T.E. Markusic, and S.T. Wu. Effects of equation of state and transport on the modelling of pulsed plasma accelerators. In 35th *AIAA Plasmadynamics and Lasers Conference*, Portland, Oregon, June 28 - July 1 2004. AIAA-2004-2361.

[57] S. Ogi, M. Shiratani, M. Takamatsu, and Y. Watanabe. On shifting of plowed plasma to back of current sheath in implosion phase of theta pinch. *Japanese Journal of Applied Physics*, 26(8):1334–1341, 1987.

[58] M. Alidieres, R. Aymar, F. Koechlin, P. Jourdan, and A. Samain. Shock and current sheet structure in a theta-pinch configuration. *Physics of Fluids*, 13(6):1525–1532, 1970.

[59] W. Eckstein. Reflection. *Nuclear Fusion*, 1:17–30, 1991.

[60] R. Ito, T. Tabata, N. Itoh, K. Morita, T. Kato, and H. Tawara. Data on the backscattering coefficients of light ions from solids (a revision) IPPJ-AM-41. Technical report, Institute of Plasma Physics, Nagoya, Japan, 1985.

[61] A.C. Eckbreth, K.E. Clark, and R.G. Jahn. Current pattern stabilization in pulsed plasma accelerators. *AIAA Journal*, 6(11):2125–2132, 1968.

[62] A.C. Eckbreth and R.G. Jahn. Current pattern and gas flow stabilization in pulsed plasma accelerators. *AIAA Journal*, 8(1):138–143, 1970.

[63] J.K Ziemer, E.A. Cubbin, E.Y. Choueiri, and D. Birx. Performance characterization of a high efficiency gas-fed pulsed plasma thruster. In 33rd *Joint Propulsion Conference*, Seattle, Washington, July 6-9 1997. AIAA-97-2925.

[64] J.W. Berkery and E.Y. Choueiri. Basic mechanisms controlling the sweeping efficiency of propagating current sheets. *Submitted for publication to Plasma Sources Science and Technology*, 2005.

[65] International Atomic Energy Agency. Effective rate coefficient calculator. http://www-amdis.iaea.org/RATES/.

[66] W.L. Wiese, M.W. Smith, and B.M. Glennon. *Atomic Transition Probabilities, Volume I*. National Bureau of Standards, 1966.

[67] Y.P. Raizer. *Gas Discharge Physics*. Springer-Verlag, 1991.